# Study of Thin Liquid Film Drainage and Interaction Forces in Organic Solvent for Liquid/Solid and Liquid/Liquid Interactions Using Dynamic Force Apparatus (DFA)

by

Nina Olegovna Ivanova

A thesis submitted in partial fulfillment of the requirements for the degree of

Doctor of Philosophy

in

Chemical Engineering

Department of Chemical and Materials Engineering

University of Alberta

# Abstract

Properties of thin liquid films between two approaching droplets or between a droplet and a solid surface are critical for emulsion stability and for mineral flotation. If the thin liquid film is stable, no coalescence occurs, while an unstable film will lead to rupture and coalescence or the formation of a three-phase contact line. While many studies have been conducted on the drainage of thin liquid films in aqueous media using techniques such as the Surface Force Apparatus (SFA) or Atomic Force Microscopy (AFM), fewer have been undertaken in organic media. Hydrodynamic effects, while important in many practical applications, are neglected in most studies by limiting approach speeds to low Reynolds numbers. This thesis focuses on understanding thin film behaviour and surface forces involved in the interaction of water/water and water/solid in "clean" and "contaminated" organic systems.

A Dynamic Force Apparatus (DFA), which allows for simultaneous measurement of interfacial film thickness, drainage time and interaction forces at precisely controlled approach velocities, was used to study the interactions of a water drop with solid surfaces or between two water drops in organic liquids. For the "clean" system, two types of organic solvents were used: toluene and *n*-heptane (with and without water saturation). In the case of *n*-heptane, a very fast film rupture occurred for fully water-wettable hydrophilic silica and mica, with a very long-range attractive force observed (in the mm range), capable of deforming the interacting water droplet(s) prior to contact. It was shown that increasing substrate *n*-heptane immersion time, droplet salt concentration, approach velocity and pH decreased the observed long-range force and droplet elongation, with the opposite effect (increased attractive force, drop elongation) observed for water-saturated *n*-heptane; high pH was found to increase drop elongation for drop/drop

interactions. In the case of toluene, sapphire or all hydrophobized substrates, no elongation of droplet(s) or long-range force was observed.

For the "contaminated system", the fundamental behaviour of thin organic liquid films (containing the asphaltene model compound C5PeC11) between a droplet and solid surface was elucidated using a temperature-controlled DFA cell. A water droplet in 0.1 g/L C5PeC11-in-toluene solution was driven towards a silica surface of varying wettability (contact angles of 0° and 107°) at two different droplet approach velocities (0.1, 1 mm/s) and temperatures (22°C, 40°C). The observed spatiotemporal thin film drainage dynamics and interaction force agreed well with the prediction of the Stokes-Reynolds-Young-Laplace (SRYL) theoretical model. Rupture of thin liquid films between a water droplet and silica surfaces was observed, with moving three phase contact line and strong attachment for hydrophilic silica and minor, local attachment and an easily detachable water drop for hydrophobic silica. Increasing the approach velocity of water droplets towards solid surfaces resulted in a larger dimple and longer film lifetime. Interestingly, higher temperature led to a faster film rupture for hydrophilic silica, in line with industrially observed improvements in bitumen production for the removal of water-in-oil emulsions at higher temperatures during froth treatment.

The major contributions to science of this thesis are the detection of a novel, extra long-range attractive force in a "clean" *n*-heptane system observed between water/(silica or mica) and water/water that cannot be described by current DLVO theory. The DFA was used to quantify the effect of salt concentration, pH, approach velocity, solvent immersion time and solvent water saturation on the extra long-range attractive force in the "clean" *n*-heptane system. The interaction forces and thin film drainage were also explored for other "clean" systems where no

such long-range force was observed, namely hydrophobized surfaces and sapphire. Finally, in the “contaminated” system, the effect of velocity, wettability and temperature were elucidated for a water droplet driven toward a silica surface in a dilute C5PeC11/toluene solution, with the results in good agreement with the SRYL theoretical model.

# Preface

This thesis is composed of original work and three papers at different stages of preparation. The following is a statement of contributions made to the jointly authored papers contained in this thesis:

- Chapter 1 Introduction. Original work by Nina Ivanova.
- Chapter 2 Literature Review. Original work by Nina Ivanova, with part of this chapter published as: Ivanova, N.O.; Xu, Z.; Liu, Q..; Masliyah, J.H. "Surface Forces in Unconventional Oil Processing", *Curr. Opin. Colloid Interface Sci.* **2017**, *27*, 63-73. Ivanova was responsible for concept development and manuscript preparation. Xu, Liu and Masliyah were involved in manuscript corrections and proofreading.
- Chapter 3 Materials and Methods. Original work by Nina Ivanova.
- Chapter 4 Organic Systems – Liquid/Solid Interactions & Chapter 5 Organic Systems – Liquid/Liquid Interactions. Original work by Nina Ivanova, manuscript in preparation. Ivanova was responsible for experimental work, data analysis and manuscript preparation. Manica, Liu and Xu are involved in manuscript corrections and proofreading.
- Chapter 6 Contaminated Organic Systems: Drainage Dynamics of Thin Liquid Films between Water and Silica. A version of this chapter has been published: Ivanova, N.O.; Manica, R.; Liu, Q.; Xu, Z. "Effect of Velocity, Solid Wettability, and Temperature on Drainage Dynamics of C5PeC11-in-Toluene Films between Silica and Water Droplet", *Energy & Fuels* **2020**, *34* (6), 6834-6843. Ivanova was responsible for experimental work, data analysis and manuscript preparation. Manica performed data modeling and contributed manuscript corrections. Liu and Xu proofread manuscript prior to submission.
- Chapter 7 Conclusions and Future Perspectives. Original work by Nina Ivanova.

# Acknowledgements

I would like to thank my supervisors, Dr. Zhenghe Xu and Dr. Qingxia Liu, for their continued guidance, support and encouragement throughout my graduate studies.

I would also like to thank all members in the Oil Sands Research Group, especially Dr. Rogerio Manica, Dr. Bo Liu and Dr. Zuoli Li, for their help and insightful suggestions during the course of this work. I would like to extend my gratitude to Mr. James Skwarok, Ms. Jie Ru and Ms. Lisa Carreiro for their assistance with administrative matters and general lab support. The help of the machine shop, especially Bob Smith and Les Dean, is also greatly appreciated.

I am grateful for the financial support from NSERC−Industrial Research Chair Program in Oil Sands that has made this research possible.

Finally, my deepest gratitude goes to my family, especially my son, fiancé, mother and father, for their incredible patience and their steadfast belief that I could accomplish anything I set my mind on. It is to you that I dedicate this work.

# Table of Contents

# List of Tables

# List of Figures

# Nomenclature

## Symbols

| | |
|---|---|
| $A$ | Hamaker constant, J |
| $D$ | Distance, μm |
| $d_{31}$ | Piezo material charge constant |
| $E$ | Young's modulus, N/m$^2$ |
| $F$ | Force, N |
| $F_{adh}$ | Force of adhesion, N |
| $G$ | Gibb's modulus, N/m$^2$ |
| $h(r,t)$ | Film thickness, m |
| $h_c$ | Film thickness at the center of film, m |
| $h_{rim}$ | Film thickness at the rim of film, m |
| $I$ | Moment of inertia, kg·m$^2$ |
| $I(r,t)$ | Instantaneous light intensity |
| $I_{max}$ | Maximum light intensity |
| $I_{min}$ | Minimum light intensity |
| $j$ | Bimorph thickness, m |
| $K$ | Spring constant, N/m |
| $k_B$ | Boltzmann constant, J/K |
| $L$ | Length, m |
| $m$ | Order of interference |
| $n_1\ n_2\ n_3$ | Refractive index of droplet, continuous phase and solid |
| $p(r,t)$ | Hydrodynamic pressure in the film, N/m$^2$ |
| $Q$ | Accumulated charge, C |
| $R$ | Radius of water drop, m |
| $r$ | Radial direction, m |
| $r_c$ | Inner radius of capillary, m |

| | |
|---|---|
| $Re$ | Reynolds number |
| $S(t)$ | Distance between initial (undeflected) and deflected bimorph, m |
| $T$ | Temperature, K |
| $t$ | Time, s |
| $V$ | Velocity, m/s |
| $X(t)$ | Distance between end of capillary and un-deflected bimorph, m |
| $z$ | Vertical direction, m |

## Greek Symbols

| | |
|---|---|
| $\gamma$ | Interfacial tension, N/m |
| $\delta$ | Phase lag between incident and reflected rays |
| $\varepsilon$ | Dielectric constant |
| $\theta$ | Contact angle, ° |
| $\lambda$ | Wavelength of light, m |
| $\mu$ | Viscosity, Pa·s |
| $v_e$ | Absorption frequency, $s^{-1}$ |
| $\Pi(h)$ | Disjoining pressure, $N/m^2$ |
| $\Pi_h$ | Hydrophobic interaction energy, $J/m^3$ |
| $\Pi_s$ | Steric interaction energy, $J/m^3$ |
| $\Pi_{VdW}$ | Van der Waals interaction energy, $J/m^3$ |
| $\rho$ | Density, $kg/m^3$ |
| $\sigma$ | Surface tension, N/m |

## Abbreviations

| | |
|---|---|
| AFM | Atomic force microscope |
| CCD | Charge-coupled device |
| C5PeC11 | N-(1-undecyldodecyl)-N′-(5-carboxypentyl)-perylene-3,4,9,10-tetracarboxylic bisimide |
| DFA | Dynamic force apparatus |
| DLVO | Derjaguin-Landau-Verwey-Overbeek |
| ITFDA | Integrated thin film drainage apparatus |
| OTS | *n*-octadecyltrichlorosilane |
| PTFE | Polytetrafluoroethylene |
| RMS | Root mean square |
| sat. | Solvent (toluene or *n*-heptane) saturated with water |
| SFA | Surface force apparatus |
| SRYL | Stokes-Reynolds-Young-Laplace |
| TLF | Thin liquid film |
| VdW | Van der Waals |

# Chapter 1: Introduction

## 1.1 Background and Motivations

Emulsions are of practical importance to many industrial processes, including petroleum production[1–6], pharmaceuticals[7,8], foods[9,10] and agrochemicals[11]. An emulsion is a fine dispersion of one liquid in another, where the liquids are immiscible. Whether the goal is to create a stable emulsion (e.g., mayonnaise with a long shelf life) or to break up an undesired emulsion (e.g. water-in-oil (W/O) petroleum emulsions), the intervening thin liquid film formed between approaching emulsified droplets determines emulsion stability and behaviour. The properties of this thin liquid film are impacted by factors inherent to a given emulsified system (such as interfacial tension, surface forces), but also by outside variables such as the hydrodynamics[12] and temperature (a controllable variable in many industrial processes including petroleum production) of the system.

At 3.2 trillion barrels of currently recoverable unconventional oil, and with in-place reserves putting Canadian oil sands alone at 1.7 trillion barrels, it is increasingly important to find both economical and environmentally-friendly technologies to extract this natural resource and bring it to market.[13] During the production of bitumen from oil sands, the formation of highly stable W/O emulsions are a major challenge for the petroleum industry in general, and oil sands deposits in Alberta in particular. Emulsified water in W/O emulsions is notorious for carrying chlorides and solids to downstream upgraders, which results in wear, corrosion and fouling problems.[14] Surface active materials, including asphaltenes, natural surfactants (e.g. naphthenic acids) and fine solids, form a protective film at the W/O interface that prevents coalescence of water droplets, leading to stable W/O emulsions.[15] Considering that asphaltenes are a solubility class (soluble in toluene and insoluble in *n*-alkanes), the heterogeneity of asphaltene chemical structures leads to difficulties in studying their fundamental behaviour. For this reason, the use of model asphaltene compounds (can mimic asphaltene properties with a well-defined molecular structure) such as C5PeC11is beneficial.

In order to improve the demulsification of W/O emulsions observed in froth treatment during bitumen processing, a more thorough fundamental understanding of the surface forces and interfacial thin film drainage dynamics in both "clean" systems (pure solvents and clean substrates) and "contaminated" systems (with C5PeC11 asphaltene model compound) for non-polar continuous media (toluene or *n*-heptane) is needed.

## 1.2 Objectives and Thesis Scope

The major objective of this work is to gain an improved understanding of interaction forces and thin film drainage dynamics for water/solid and water/water interactions in "clean" and "contaminated" organic systems. Through the use of the Dynamic Force Apparatus (DFA), the interaction forces and spatiotemporal thin film drainage were measured, and resulting film profiles were fit using the Stokes-Reynolds-Young-Laplace (SRYL) theoretical model. The DFA allows for simultaneous measurement of interaction force, spatiotemporal film drainage and droplet side profile in a variety of hydrodynamic conditions (approach velocity in mm/s), as well as a specialized cell that allows for experiments at elevated temperatures.

In the first part of this thesis, interaction force and spatiotemporal film drainage between a water drop and solid surfaces (silica, sapphire, mica) in organic media (toluene, *n*-heptane) were investigated using the DFA. A long-range attractive force was observed between water and hydrophilic substrates (mica, silica) in *n*-heptane, with no long-range attraction in toluene. The magnitude of long-range attractive force and water drop elongation at drop/surface contact were explored as a function of solvent exposure time (water drop, substrate), solvent type (pure or water-saturated), drop salinity and pH, substrate wettability, substrate surface roughness and drop approach velocity.

In the second part of this thesis, the interaction force between two water drops in *n*-heptane was measured using the DFA. A long-range attractive force was detected, with drop elongation observed at drop/drop contact. The effect of silica solvent exposure time, bottom water drop solvent exposure time and the drop pH on the magnitude of the attractive force and drop elongation at drop/drop contact were explored.

In the third part of this thesis, the fundamental behaviour of thin organic liquid films containing model asphaltene compound C5PeC11 between a silica substrate and water drop was elucidated by using a temperature-controlled DFA cell. The effect of water drop approach velocity, substrate wettability and temperature were analyzed, with the SRYL theory used successfully to model the observed thin film drainage dynamics. Higher temperature led to faster film rupture for hydrophilic silica, which agreed with observations of more rapid oil/water phase separation at higher temperatures in petroleum emulsion systems.

## 1.3 Organization of the Dissertation

This thesis consists of seven chapters.

Chapter 1 provides a short introduction to the background and main objectives of this research.

Chapter 2 provides a literature review of emulsions and interfacial thin film drainage, and how this applies to understanding "clean" organic systems, as well as "dirty" organic systems such as water-in-oil emulsions stabilized by asphaltenes encountered in froth treatment in the oil sands.

Chapter 3 details the experimental methodology, Dynamic Force Apparatus setup and operation, force and displacement measurement, and conversion of Newton fringes into spatiotemporal film profiles.

Chapter 4 investigates liquid/solid interactions in "clean" organic systems, namely interactions between water drop and solid (silica, sapphire or mica) in toluene or *n*-heptane.

Chapter 5 shows liquid/liquid interactions in "clean" organic systems, namely interactions between a water drop driven towards a water drop deposited on a silica surface, in *n*-heptane.

Chapter 6 presents liquid/solid interactions in a "contaminated" organic system, specifically the drainage of C5PeC11-in-toluene thin films between a water drop and silica as a function of temperature, wettability and approach velocity.

Chapter 7 summarizes the work presented in this dissertation and provides suggestions on future work in this research field.

# Chapter 2: Literature Review

## 2.1 Emulsions

### *2.1.1 Types of emulsions*

An emulsion is the dispersion of a liquid in another immiscible liquid; typically, they are water and oil. Both surfactants and solids can stabilize emulsions, with the latter known as a Pickering emulsion.[16] Whether addition of a surfactant results in O/W or W/O emulsion is a function of its HLB (hydrophilic-lyophilic balance), with HLB of 3-6 and 8-18 resulting in W/O and O/W emulsions, respectively. For solid particles, contact angle $\theta$ is typically measured through the aqueous phase, where $\theta > 90°$ represents hydrophobic particles that form W/O emulsions. Most emulsions (except microemulsion) are metastable, that is, thermodynamically unstable but kinetically stable.[1] While both particles and surfactants can form stable emulsions, there are some key differences in their stabilization mechanisms.[17] Surfactants stabilize emulsions by lowering the interfacial tension, as described by Gibb's law, with energy on the order of several $kT$'s per surfactant molecule. Conversely, solid particle attachment at the interface has no effect on interfacial tension – the driving force is the reduction in the system's internal energy (Gibb's free energy $\Delta G$). For very small particles (1 nm or less), the particle attachment energy is similar to adsorption energy of a typical surfactant, due to their similar size. Such particles are not effective emulsion stabilizers, whereas larger particles (but on colloidal length scale) can be effectively considered permanently attached to the interface due to the high energetic benefit provided to the system.

### *2.1.2 Organic systems with liquid/solid interactions*

The interaction forces between oil droplet and solid in aqueous media has been studied extensively,[12,18,19] while water droplet and solid interactions in non-polar, organic media have not garnered attention until relatively recently, despite their importance in industrial applications such as fouling issues in petroleum processing[20] and water desalination[21]. After pioneering studies where Atomic Force Microscopy (AFM) had been used to study interactions between a spherical colloidal particle attached to the AFM force-sensing cantilever and a bubble,[22,23] the

AFM technique was extended to study interaction forces in other systems such as liquid and solid interactions in organic media, described in detail below.

Kuznicki *et al.*[24] used an AFM silica colloid probe (8 μm colloidal particle attached to a cantilever) to study interactions with a water drop (~80 μm) anchored on hydrophobized silicon wafer in 0.05-0.2 g/L asphaltenes-in-toluene solution. The water interface was aged in the asphaltenes solution for 15 minutes prior to experiment, with 1 μm/s probe approach velocity used. Asphaltenes adsorbed on the water interface created a protective steric layer, leading to a repulsive interaction between silica probe and water droplet, as well as an adhesive force on probe withdrawal (~3-4 nN) related to interpenetration of adsorbed asphaltene layers.[24] The same authors also looked at the effect of solvent type (toluene or 1:1 toluene/*n*-heptane mix), water drop ageing time and drop/silica contact time on interactions between silica colloidal probe and water droplet in 0.1 g/L asphaltene-in-solvent solutions.[25] They observed repulsion in all cases, with increased force of adhesion with increasing drop ageing and silica/water drop contact time, during the withdrawal of silica probe from water drop. In the case of 1:1 solvent mix, no significant change in adhesion was observed over time after ~10 minutes due to fast initial "interfacial stiffening" (high dilatation elasticity and crumpling ratio).[25]

Liu *et al.*[26] studied the impact of modifying the wettability of a bitumen-coated silica surface with amphiphilic poly(ethylene glycol)-block-poly(propylene glycol)-block-poly(ethylene glycol) (PEG-PPG-PEG) on the interaction force between such a surface and a water drop in cyclohexane. They used the AFM drop probe technique, where a 35 μm water drop was attached to a cantilever and approached the silica surface at 1 μm/s. The interaction between water drop and bitumen-coated silica surface showed initial weak hydrodynamic repulsion, with ~0.3 nN jump-in on contact, but growing repulsion at maximum load force, followed by drop detachment from bitumen-coated surface on retraction.[26] The adsorption of PEG-PPG-PEG on bitumen-coated silica rendered the surface relatively hydrophilic: the water droplet readily detached from the AFM cantilever and coalesced with PEG-PPG-PEG surface, explaining aggregation of water drops and bitumen-covered silica particles coated with PEG-PPG-PEG.[26]

Gong *et al.*[20] looked at the interaction of a water drop with Fe substrates (with and without an electroless nickel-phosphorous (EN) coating) in toluene/heptol (mixture of toluene and *n*-heptane) solvent in the presence of asphaltenes. They used the AFM drop probe technique, with ~70 μm water drop attached to the cantilever and approached the substrate at 1 μm/s. The water drop was aged in asphaltenes for 5 minutes, after which unadsorbed asphaltenes were washed away from the cell and replaced with pure solvent. Specifically, the effect of solvent type (toluene with varying levels of *n*-heptane), asphaltene concentration, ageing time, contact time and loading force on drop/substrate interaction were elucidated. For pure water drop interactions in toluene, the water drop jumped-in (detached from cantilever) on surface contact, with an attractive Van der Waals (VdW) force observed for Fe, and no noticeable VdW for EN, prior to jump-in.[20] With higher toluene content in solvent (improved asphaltene solvent), increasing asphaltene concentration, contact time, loading force and ageing time, the adhesion force on retraction between water drop and Fe/EN surface became stronger due to the increasing amount and conformational change of adsorbed asphaltenes at the water/oil interface.[20] In all cases, the adhesion force between water and EN was noticeably weaker than for water and Fe, confirming the observed anti-fouling properties of EN that reduce asphaltene adsorption.[20]

Hu *et al.*[21] examined the effect of tannic acid on $MoS_2$ nanosheet membrane capacity to increase membrane water flux while maintaining high cation rejection rates. Using AFM probe technique, a water droplet (70-90 μm) was driven toward $MoS_2$ nanosheet or tannic acid-modified $MoS_2$ nanosheet ($TAMoS_2$) in toluene at 1 μm/s. Interaction with regular $MoS_2$ nanosheet showed no long-range attraction with attachment of the water drop to $MoS_2$ nanosheet on contact, while interaction of the water drop with $TAMoS_2$ showed long-range (~200 nm) attraction prior to drop attachment to surface on contact.[21] The authors attributed the long-range attraction to stronger dipole-dipole interaction between polyphenol groups of the tannic acid and water, with AFM measurements confirming observed superior performance of $TAMoS_2$ membranes in water purification.[21]

### *2.1.3 Organic systems with liquid/liquid interactions*

While much work on surface forces has been carried out for liquid/liquid interactions in aqueous systems,[27,28] studies in organic systems have been less abundant. Shi *et al.*[29] looked at interaction

forces between two water droplets in toluene using AFM, with (up to 0.5 g/L) and without asphaltenes. One water droplet was anchored to the bottom of the hydrophobized (~90°) glass fluid cell, and the second was anchored to an AFM tip. Both water droplets were ~100-200 μm and the top water droplet was moved downwards at 1 μm/s during approach to exclude hydrodynamic effects. Pure water droplets in toluene readily coalesced, while asphaltenes interfacially adsorbed on water drops could sterically inhibit drop coalescence and induce interfacial adhesion upon top water droplet retraction.[29] Specifically, the authors found increased adhesion with increasing: asphaltene concentration (up to 0.1 g/L), drop/drop force on contact and contact time. With the addition of *n*-heptane (a poor solvent for asphaltenes) to toluene, interfacial adhesion between water droplets was enhanced at low asphaltene concentrations and reduced at high asphaltene concentrations.[29]

In another study, Xie *et al.*[30] examined the interaction between two water droplets (~100 μm diameter) in pentol (a 1:1 mix of pentane : toluene) using AFM probe technique (one water drop attached to cantilever), as a function of NaCl concentration and asphaltene concentration. Pure water droplets in pentol coalesced on contact, while droplets with adsorbed asphaltenes remained stable due to steric repulsion. They found reduced interfacial adhesion between water droplets with increasing concentration of NaCl and asphaltenes, with interfacial adhesion on drop separation attributed to the contact, interpenetration and local aggregation of asphaltene molecules.[30] With increasing accumulation of asphaltenes at the water/pentol interface, a stronger repulsion force between two water droplets led to the observed weakening of interfacial adhesion.[30]

Several of the relevant force curves discussed in the previous two paragraphs are shown in Figure 2.1, where drop/drop interaction curves in pentol and toluene are shown in red and blue, respectively. For both systems in Figure 2.1, the water droplets with asphaltenes were exposed to an asphaltene solution (in toluene or pentol) for 5 minutes, after which the AFM cell was purged of excess asphaltenes by washing with pure toluene or pentol. In addition, the piezo displacement in Figure 2.1 is the relative movement of the droplet-loaded cantilever (not true drop/drop separation), with zero point arbitrarily chosen (coalescence or largest measured repulsive force). Interactions between pure water drops (Figure 2.1A,C) led to coalescence (due

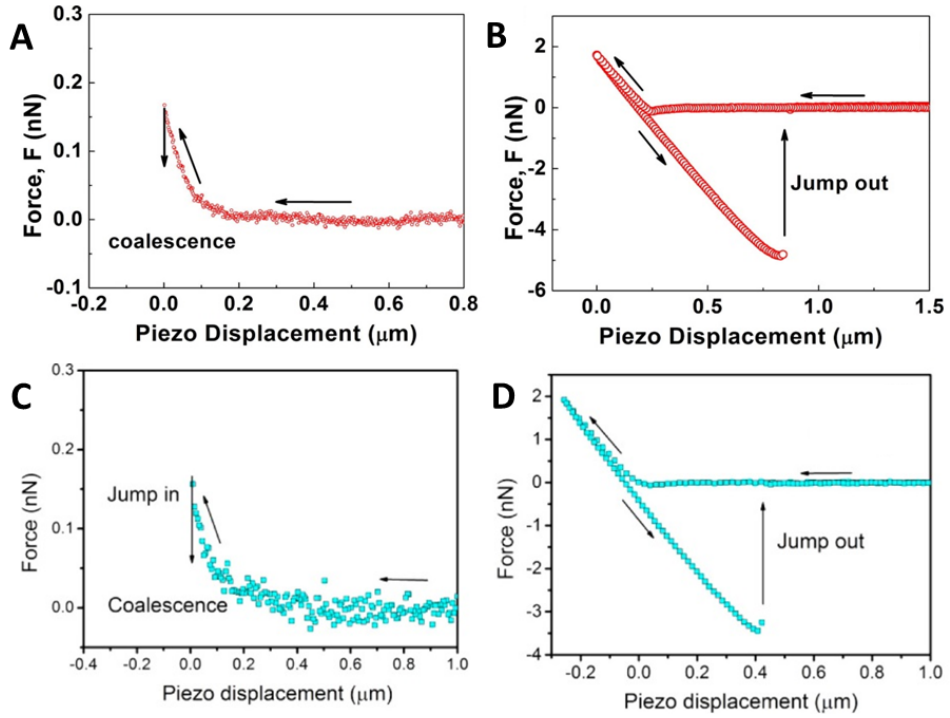


Figure 2.1 Interaction forces between two water droplets in pentol (A-B)[30] and toluene (C-D)[29], with coalescence observed for pure water/water interaction (A,C) and repulsion with drop/drop adhesion for 0.1 g/L asphaltenes (C,D). The arrows indicate movement of cantilever-anchored water droplet.

to an attractive VdW force), while water drops that have been aged in 0.1 g/L asphaltenes had repulsive interactions on contact, followed by asphaltene interpenetration that led to the observed adhesion force, with eventual jump-out during top drop withdrawal (Figure 2.1B,D). Similar results to those shown in Figure 2.1D were found by Kuznicki *et al.*[24] for water droplets interacting in 0.1 g/L asphaltenes-in-toluene solution. They also used the AFM water drop probe technique, with ~80 μm water drops, at an approach velocity of 1 μm/s. At a longer ageing time prior to experiment (15 minutes) and with free asphaltenes present in solution (in place of pure toluene), they observed a 5.4 nN adhesion force on drop separation.[24]

The AFM water probe technique was employed by two other research groups to study water drop interactions in non-polar media. Vakarelski *et al.*[31] looked at interactions between two water droplets (~70-80 μm; pure or stabilized with SPAN® 80 non-ionic surfactant) in tetradecane at a

cantilever approach velocity of 2-50 μm/s. Both the cantilever (top drop) and glass slide (bottom drop) were hydrophobized to facilitate experiment set-up and to maintain the spherical shape of the water drops. In pure tetradecane, water droplets coalesced at low approach velocity (under 30 μm/s), but remained stable at high approach velocity (50 μm/s); authors attributed this to trace contamination of tetradecane used ($\gamma$ = 42 mN/m versus $\gamma$ = 52 mN/m expected for tetradecane/ water interface).[31] Water drops with SPAN® 80 remained stable to coalescence (repulsive interaction) at all approach velocities.[31] Mettu *et al.*[32] looked at the interaction between two water droplets (60-150 μm) in canola oil at cantilever approach velocity of 0.2 μm/s. The water droplets were coated with poly-glycerol-poly-ricinoleate (PGPR) dissolved in canola oil (0-0.2 wt%), which is a fat-soluble, non-ionic surfactant used to stabilize water-in-oil food emulsions. The low approach velocity was chosen to help minimize approach/retract hysteresis of the force curves related to hydrodynamic drainage effects of the high-viscosity canola oil ($\mu$ = 70 cP).[32] In pure canola oil, water drops coalesced on contact with no repulsion, while PGPR adsorbed on the interface led to stable films due to steric repulsion and a short-range attraction on withdrawal at low concentrations attributed to PGPR bridging.[32]

## 2.2 Emulsions in Bitumen Production

### *2.2.1 Overview of bitumen extraction process*

Figure 2.2[13] shows the overall bitumen extraction process, where 1 barrel of bitumen routinely requires 1.8 tons of mined oil sands ore and generates 3.3 $m^3$ of tailings as a by-product of the process. Commercially produced bitumen from Athabasca oil sands typically uses the Clark hot water process,[33,34] which involves crushing of mined ores and mixing of the crushed ores with process aids (e.g. NaOH) and warm water to form a slurry that is transported via a hydrotransport slurry pipeline.[13] Under the favourable physicochemical condition, the turbulence in the pipeline causes heavy oil (bitumen) to detach from solid particles and become aerated with entrained air.[35] This slurry enters a gravity separation vessel (labelled PSV, or primary separation vessel, in Figure 2.2), where the aerated bitumen is collected as froth with an average composition of 60 wt% bitumen, 30 wt% water and 10 wt% solids.[36] Athabasca bitumen typically contains the following constituents: ~1-2 wt% naphthenic acids, ~18 wt% asphaltenes and ~40 wt% resins.[37]

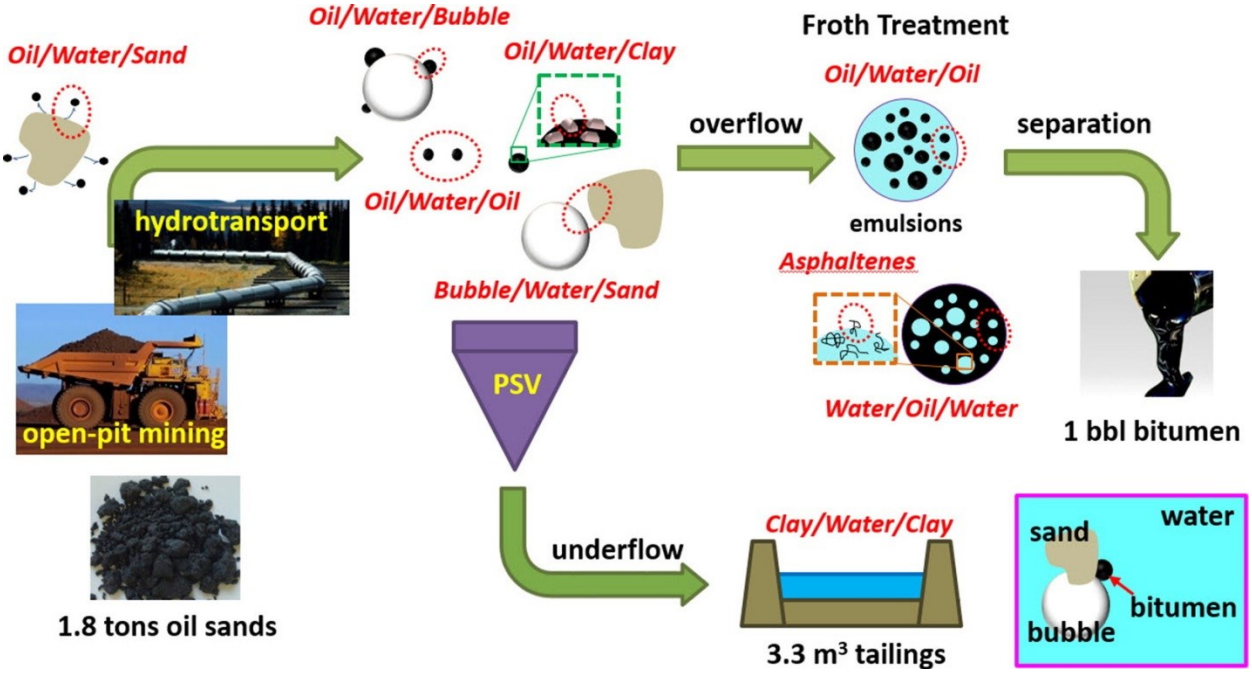


Figure 2.2 Schematic of bitumen extraction, showing overall process with relevant interaction types governed by surface forces.[13]

Gravity separation generates two streams: overflow and underflow. The froth is collected in the overflow and sent to froth treatment, where the majority of water and solids are removed using centrifugation at elevated temperatures (as high as 80°C), but up to 3 wt% of water in the froth is present in the form of kinetically stable W/O emulsions, and involve the addition of demulsifiers (commonly variants of EO-PO (ethylene oxide-polyethyle oxide) and EC (ethylcellulose) polymers)[3] to aid in water removal. While there could be innate emulsions present in any oil reservoir (connate water blocked off from oil migration into reservoir), most W/O emulsions are formed during turbulent transport (wellbore, centrifugal pump impellers, hydrotransport, etc.)[35] Once demulsified, bitumen is sent to upgrading where it is converted to synthetic crude oil (SCO). The underflow stream (predominantly water and solids) goes to the tailings pond for solid-liquid separation. While coarse solids (sand) settle relatively quickly to form beaches along the tailing ponds, the remaining fines (silts and clays) remain stable for decades composed of approximately 30 wt% fines and 70 wt% water, also known as fluid fine tailings (FFT).[38]

### *2.2.2 Water-in-oil emulsions*

#### *2.2.2.1 Role of fine solids*

W/O emulsions stabilized by fine solids are complex and influenced by many factors,[39] including particle size, density, shape, type of fine solid, relative concentration of different solid species, the presence and concentration of asphaltenes, surface coverage and others. The impact of wettability on drainage dynamics of emulsion thin liquid film has implications for demulsification using wettability-based membranes.[40,41] Some of the fine solids encountered in bitumen extraction are inorganic solids including clays (predominantly kaolinite and illite[17]), fine sands and heavy metal minerals (ex. pyrite). Thus, the role of fine solids in emulsion stability cannot be neglected. Asphaltenes have previously been shown to form aggregates and network structures[4] when in certain solvents after ageing. To provide a better control of formation of Pickering emulsions, rag layers and mature fine tailings in unconventional oil processing, much needs to be done to study anisotropic surface properties of clays and understand molecular interactions of various clay surfaces with natural components of heavy oil.

#### *2.2.2.2 Role of asphaltenes*

Asphaltenes are molecules classified by their solubility, with a wide distribution of chemical structures, functionality, polarity and molar mass.[1] Asphaltenes are amongst the most polar and surface active species found in crude oil, and as a solubility class, asphaltenes are soluble in aromatic solvents (e.g. toluene) but insoluble in *n*-alkanes (e.g. pentane). The most common way to obtain them is to use the so-called SARA (Saturates, Aromatics, Resins and Asphaltenes) analysis, with one of the standard protocols described in ASTM D6560-2012.12. Numerous structures have been proposed for asphaltenes (Figure 2.3), known in the scientific literature as archipelago,[42] island-like[43] and supramolecular[44] models. The archipelago model is based on GPC and vapour osmometry mass estimations of asphaltenes of 2000 Da or more.[42] Figure 2.3a shows several small aromatic ring systems that are connected by alkyl or sulfide bridges, with some coordinated porphyrin-like transition metal (ex. vanadium) complexes present. The island-like model (Figure 2.3b), also known as the Yen-Mullins model, indicates an asphaltene structure with a single polyaromatic core that has an average of seven condensed aromatic rings and several alkyl/naphthenic side chains. This model is consistent with asphaltene molecular weights

of 750 Da, with aggregation number less than 10 molecules and driven by π-π stacking.[43] Finally, the supramolecular is the latest model (Figure 2.3c), proposed by Gray *et al.*,[44] that expands asphaltene intermolecular interactions to include, in addition to π-π stacking, acid-base interactions, H-bonding, VdW forces (between alkyl, apolar and cycloalkyl groups) and metal coordination complexes. This allows for aggregates of highly variable size and shape, accounting for the high level of asphaltene weight polydispersity being observed.[45]

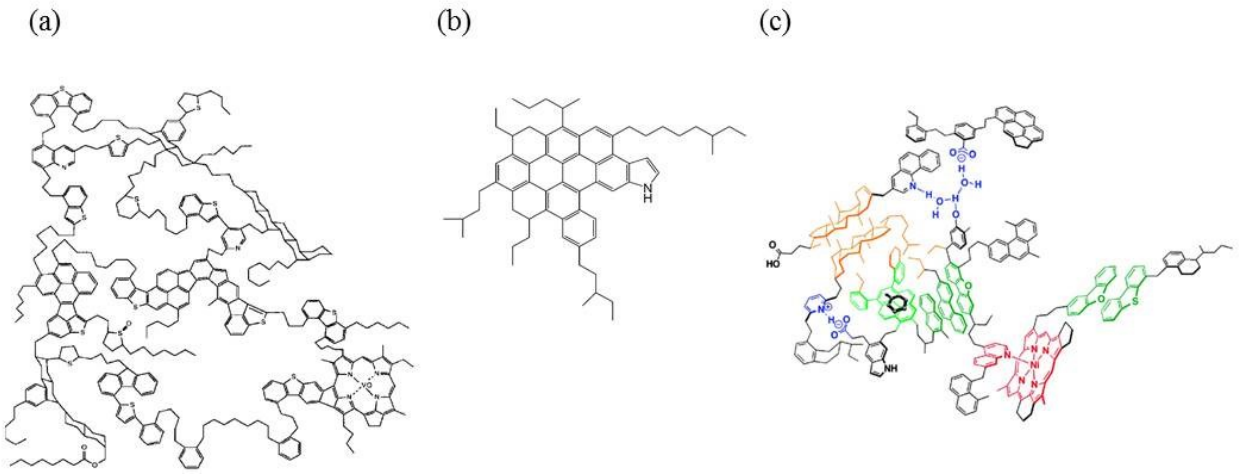


Figure 2.3 Asphaltene proposed molecular structures: (a) archipelago model[42] (b) island-like model[43] and (c) supramolecular model[44]

Kilpatrick[1] recently summarized four main interfacial properties of asphaltene films at the oil-water interface:

1) asphaltenes change their conformation over time (hours to days) on both the molecular and intermolecular levels;
2) interfacial rheology can be described as elastic once a sufficient number of asphaltenes are adsorbed;
3) dilatational elastic modulus correlates with emulsion stability; and
4) asphaltene emulsion films (8-20 nm thickness) are more dense than the corresponding nanoscale aggregates that make up the film.

*2.2.2.3 Model asphaltene compounds*

Despite many studies regarding the role of asphaltenes in stabilizing W/O emulsions, the fundamental mechanism behind their interfacial behaviour is still not well understood. This is especially the case for interfacial thin film drainage kinetics and asphaltene interfacial film interaction with substrates of various wettabilities and at elevated temperatures. Due to the complex nature of asphaltenes, it is difficult to understand their fundamental behaviour and the research community has turned to using model compounds. These model compounds can mimic asphaltene behaviour but their molecular structure and properties are well defined. Many such molecules have been proposed[46], and this work will focus on N-(1-undecyldodecyl)-N′-(5-carboxypentyl)-perylene-3,4,9,10-tetracarboxylic bisimide (C5PeC11). C5PeC11 consists of a polyaromatic (perylene) core, carboxylic acid headgroup and aliphatic side chains, as shown in Figure 2.4.

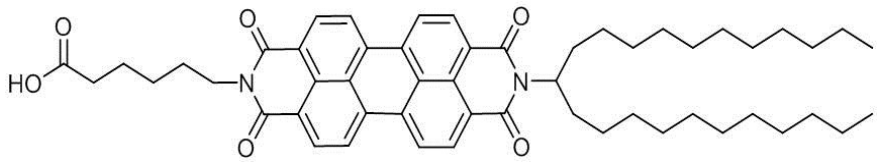


Figure 2.4 Molecular structure of C5PeC11.

The properties of C5PeC11 have been studied by electron spray ionization mass spectrometry (ESI-MS)[47], dynamic light scattering (DLS)[48], isothermal titration calorimetry (ITC)[49] and interfacial rheology[50]. Similar to indigenous asphaltenes, C5PeC11 shows pH-dependent change in interfacial tension and elastic modulus[50] as well as analogous flocculation kinetics to irreversibly-absorbed asphaltene fractions[48]. But unlike asphaltenes, C5PeC11 undergoes reversible oil/water adsorption,[50] with no inelastic steric "skin" formation as observed from the absence of crumpling[51] (no change in shape in response to volume reduction during interfacial tension measurements). In addition, it should be noted that unlike asphaltene polycyclic hydrocarbons (PAHs) that orient parallel to the interface, the oxygen functionality of compounds similar to C5PeC11 leads to a transverse orientation at the oil/water interface.[52] Overall, given a variety of studies that indicate only a fraction of asphaltenes are key players in emulsion

stabilization,[1,53–57] identifying and studying model structures for this fraction has important implications in understanding stabilization mechanisms for W/O petroleum emulsions.

*2.2.2.4 Water-in-oil emulsion studies*

Asphaltenes could be present at the interface, residing mainly in the organic phase. Destabilization of an emulsion involves droplet flocculation driven by attractive surface forces with high adhesion and coalescence, if interfacial films are unstable, resulting in phase separation. Wang *et al.*[58] were among the first to determine directly interaction forces between asphaltene surfaces in organic solvents, ranging from toluene (good asphaltene solvent) to *n*-haptane (poor asphaltene solvent) or in heptol (a *n*-heptane : toluene mixture) using AFM. Asphaltene interfacial films transferred from water-toluene interfaces onto both a silica colloidal probe and flat silica wafer using Langmuir-Blodgett method were used in this study. Figure 2.5A[58] shows the measured interaction forces ($F/R$) while the circular inset shows an average asphaltene structure as predicted by Yen-Mullins model.[59] The interaction forces are increasingly repulsive with increasing toluene content (red curve) due to steric non-DLVO forces resulting from the swelling of asphaltene layers in a good solvent such as toluene. For pure *n*-heptane (blue curve) and up to 0.2 toluene volume fraction, the steric repulsion is replaced by a weak VdW attractive force, believed to be responsible for asphaltene precipitation with π-π stacking.[3,58] Natarajan *et al.* observed similar findings from SFA measurements between asphaltenes deposited on mica: deposited asphaltene films were much more compressed in *n*-heptane than in toluene with a hard wall thickness of 20/2 and 40/2 nm, respectively.[60] These findings have practical implications in explaining, for example, the use of paraffinic solvent in precipitation of asphaltenes to enhance oil-water/solids separation in froth treatment of oil sands extraction.[36] SFA study also showed a strong time-dependent buildup of asphaltenes on mica surfaces from 1 wt% asphaltene-in-toluene solution, with the adsorbed layer thickness increasing from 30/2 nm at 5 min to 100/2 nm at 1.5 h and 300/2 nm after 4 h adsorption.[61]

To link the measured dynamics of asphaltene adsorption and interaction forces with emulsion stability and physicochemical properties of interfacial films, Harbottle *et al.* correlated in Figure 2.5(B-E) the water drop coalescence time measured using Integrated Thin Film Drainage Apparatus (ITFDA) with viscoelastic behaviour of asphaltene interfacial films formed under the

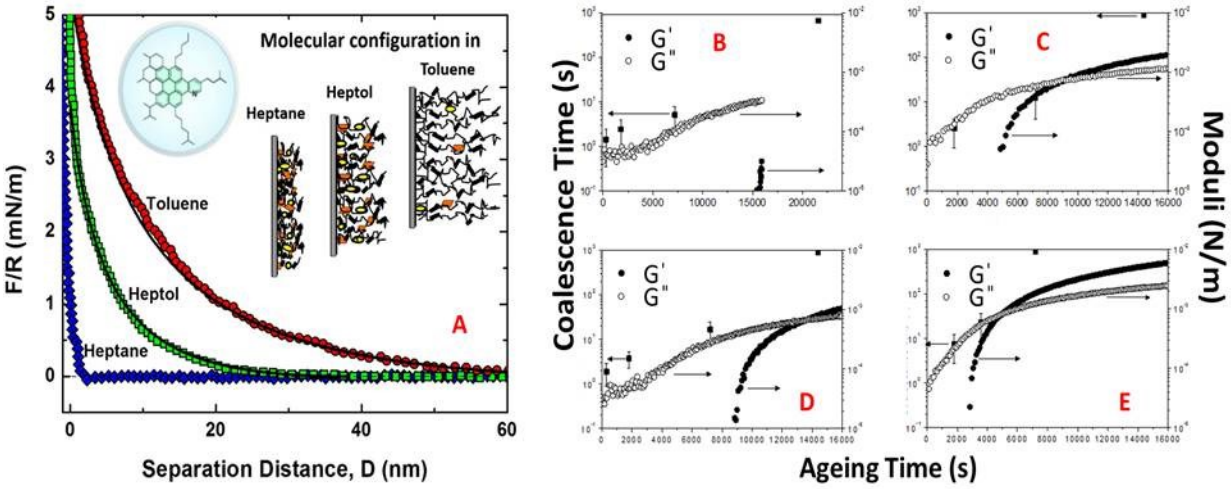


Figure 2.5[13] Asphaltene-asphaltene interaction: (A) Normalized interaction force ($F/R$) as a function of distance of asphaltene-covered colloidal probe and asphaltene deposited film in toluene (red), heptol (green) and *n*-heptane (blue)[58]; circular inset: sample asphaltene molecular structure.[59] {B – E} Comparison of water drop coalescence time and viscoelastic ($G'$ = storage modulus, $G''$ = loss modulus) properties of asphaltene interfacial films: (B) 0.1 g/L asphaltene in toluene, (C) 0.1 g/L asphaltene in heptol 1:1, (D) 0.4 g/L asphaltene in toluene, (E) 0.4 g/L asphaltene in heptol 1:1.[62]

identical conditions of asphaltene-in-toluene solution in contact with water.[62] At short ageing time all the films were viscous dominant ($G'' > G'$) with the corresponding droplets coalescing within the order of seconds. However, the films became increasingly elastic-dominant ($G' > G''$) at longer ageing time, leading to stable droplets without coalescence and hence stable W/O emulsions. Using Thin Liquid Film (TLF) balance technique, Tchoukov *et al.* observed similar effects of ageing that led to much thicker interfacial films accompanied by the formation of heterogeneous sub-micrometer aggregates.[4] From disjoining pressure isotherms of various model W/O emulsions, Taylor *et al.*[63] observed a high positive disjoining pressure Π and hence stable films for systems with high asphaltene concentrations. Although the simplified Stefan-Reynolds model (by assuming $\Pi = 0$) seemed to predict the measured film thicknesses reasonably well for the results from both groups,[4,63] applying Stokes-Reynolds-Young-Laplace model to further experimental data at lower asphaltene concentrations with and without maltenes would help in elucidating the nature of the disjoining pressure.

## 2.3 Interfacial Thin Film Drainage

### *2.3.1 Stefan-Reynolds model*

One of the first to study rate of film drainage, Reynolds[64] assumed the two surfaces were tangentially immobile, rigid and flat, and expressed film drainage rate as shown in Equation 2.1:

$$-\frac{dh}{dt} = \frac{2\pi F h^3}{3\mu A^2} \tag{2.1}$$

where $h$ is surface separation distance, $t$ is time, $\mu$ is viscosity of fluid between surfaces, $A$ is area of surfaces and $F$ is the applied force. If the Reynolds number is small and droplet radii are much larger than $h$, the lubrication approximation can be applied.[64] The equation was verified experimentally over a century later by Chan and Horn[65] using the Surface Force Apparatus (measuring rate of thinning of liquid film between solid plates). However, Equation 2.1 is applicable only for sufficiently thin and small films, with convexities and disturbance in flow appearing once the film diameter grows beyond a certain size.[66] An example is the "dimple", first proposed by Frankel *et al.,*[67] which results from a sufficient build-up of hydrodynamic pressure in the gap between approaching surfaces.

### *2.3.2 Stokes-Reynolds-Young-Laplace (SRYL) model*

Recently, a model[12] was proposed that could capture the underlying physics of thin film drainage dynamics: the Stokes-Reynolds-Young-Laplace (SRYL) model. This model has been successfully applied to simulate droplet or bubble and solid surface interactions from AFM[68], SFA[69] and DFA[48] experimental studies. The SRYL model is used to model experimental results in this work. It consists of the Stokes-Reynolds equation for tangentially immobile interfaces (Equation 2.2) and the linearized augmented Young-Laplace equation (shown here for droplet-flat solid system) (Equation 2.3). Using the lubrication approximation, the Stokes-Reynolds equation for our system is written as[70]:

$$\frac{\partial h}{\partial t} = \frac{1}{12\mu r}\frac{\partial}{\partial r}\left(rh^3\frac{\partial p}{\partial r}\right) \tag{2.2}$$

where $h(r,t)$ is the film thickness, $r$ is the radial coordinate, $t$ is time, $\mu$ is viscosity of the fluid between droplet and solid surfaces (assumed Newtonian) and $p(r,t)$ is the hydrodynamic pressure in the film (excess pressure in the film relative to bulk liquid). Equation 2.2 links the thinning rate of the film and the radial velocity due to a radial Poiseuille flow driven by a radial pressure gradient. For the C5PeC11/toluene system, the immobile boundary condition is reasonable given the presence of surface-active molecules at the water/toluene interface and also provided the best correlation between model and experimental results. Due to the large difference of scale for film thickness (nanometer) and droplet radius (millimeter), $\partial h/\partial r \ll 1$ holds for this system, resulting in the linearized version of the augmented Young-Laplace equation, which is given as:

$$\frac{\gamma}{r}\frac{\partial}{\partial r}\left(r\frac{\partial h}{\partial r}\right) = \frac{2\gamma}{R} - \Pi - p \tag{2.3}$$

where $\gamma$ is the interfacial tension, $R$ is the droplet radius and $\Pi$ is the disjoining pressure in the film. Equation 2.3 assumes that the water droplet can adjust instantaneously to accommodate changes in the hydrodynamic and disjoining pressures. This assumption is reasonable given the flexible water/organic continuous phase interface. The effect of gravity is negligible for this system due to the small density difference between water drop and continuous phase, with a Bond number well below 1. Constant droplet volume during experiment was maintained via a gastight syringe. The total interaction force $F(t)$ can be determined from Equation 2.4, based on the Derjaguin approximation:

$$F(t) = 2\pi\int_0^\infty [p(r,t) + \Pi(r,t)]rdr \tag{2.4}$$

From Equations 2.2, 2.3 and 2.4, in order to generate a theoretical model output for $p$ and $h$, the necessary input parameters are $\mu$, $\gamma$, $R$ and Π. The relevant experimental variables are illustrated in Figure 2.6.

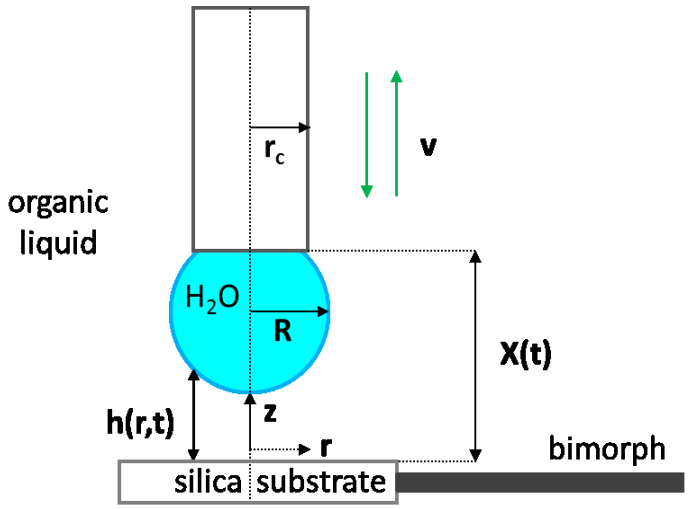


Figure 2.6 Schematic diagram of a water droplet approaching a flat solid substrate (e.g. silica) in organic liquid, where $r_c$ is the inner capillary radius, $R$ is the water droplet radius, $V$ is the droplet approach and retract velocity, $h(r,t)$ is the spatiotemporal film thickness, $X(t)$ is the distance between the end of the capillary and transparent silica substrate at the beginning of experiment (no bimorph deflection).

As a system of coupled non-linear partial differential equations, Equations 2.2 and 2.3 require one initial condition and four boundary conditions.[12,71] They can be solved numerically within the domain $0 < r < r_{max}$, where $r_{max}$ is some position outside the interaction zone (larger than the radius of the film rim) that is sufficiently large so as to generate numerical results that are independent of $r_{max}$. Briefly, the initial condition at $t = 0$, shown in Equation 2.5 below, assumes the droplet follows a parabolic profile as the droplet is far enough from the solid surface, resulting in zero film pressure (consistent with Equation 2.3):

$$h(r,0) = h_0 + \frac{r^2}{2R} \tag{2.5}$$

where $h_0$ is the initial separation between solid surface and water droplet. Next, two of the boundary conditions (Equation 2.6) are a result of the axisymmetric nature of the system interaction, that is, there is no change of pressure or film thickness at $r = 0$:

$$\frac{\partial h}{\partial r} = \frac{\partial p}{\partial r} = 0 \tag{2.6}$$

The final two boundary conditions (Equations 2.7, 2.8 and 2.9) involve defining $h$ and $p$ at $r = r_{max}$. Outside the interaction zone, $p$ decays as $r^{-4}$, thus at $r = r_{max}$, the pressure boundary condition can be implemented as follows[12]:

$$r\frac{\partial p}{\partial r} + 4p = 0 \tag{2.7}$$

The droplet is assumed pinned to the capillary tip and constant droplet volume is maintained during the experiment. Due to droplet deformation, as it starts interacting with the surface and changing shape due to the forces exerted on it, the surface of the droplet outside the interaction zone does not move at the same speed at the capillary tube. To account for this difference, change in film thickness at $r_{max}$ can be expressed as follows:

$$\frac{\partial h(r_{max}, t)}{\partial t} = \frac{dD(t)}{dt} - \frac{1}{2\pi\gamma}\frac{dF(t)}{dt}\left[\log\left(\frac{r_{max}}{2R}\right) + 1 + \frac{1}{2}\log\left(\frac{1+\cos\theta}{1-\cos\theta}\right)\right] \tag{2.8}$$

where $\theta$ is the angle the droplet makes with the capillary. The term $D(t)$ – vertical distance between the end of the capillary and a deformed bimorph – is defined in Equation 2.9 below, using geometric considerations from Figure 2.6:

$$D(t) = S(t) + X(t) = \frac{F(t)}{K} + X(t) \tag{2.9}$$

where $S(t)$ is the deflection of the bimorph from its neutral position due to droplet/solid interaction, $X(t)$ is the distance between the end of the capillary and the solid substrate at the

beginning of experiment (no bimorph deflection) and $K$ is the bimorph spring constant. $F(t)$ is calculated according to Equation 2.4 defined earlier. A standard numerical package (Matlab ode15s) was utilized to solve this system of equations by converting them to differential-algebraic equations of index 1, which was done by using Method of Lines with central differences for Equations 2.2 and 2.3, and Simpson's rule for Equation 2.4.[69,72]

### *2.3.3 Disjoining pressure*

When two droplets or a droplet and a surface approach each other, they begin to interact. These interactions can be divided into two categories, as discussed previously: thermodynamic and hydrodynamic. The former involves surface forces,[73] which can potentially include Derjaguin-Landau-Verwey-Overbeek[74,75] (Van der Waals, electrostatic) and non-DLVO (steric, polymer bridging, hydrophobic, etc.) forces. In the case of asphaltene-stabilized W/O petroleum emulsions, most likely stabilization mechanisms involve steric repulsion along with depletion and structural stabilization.[3] Surface forces are operative even if the droplets are at rest, and motion has little effect on them.[76] The thermodynamic interaction is very important in very thin films (<100 nm). A convenient way to measure it is by using the disjoining pressure Π. If $\Pi > 0$, it leads to film thickening, or the "disjoining" of the two surfaces, while $\Pi < 0$ leads to film thinning. For an organic thin film, the only DLVO force present is VdW and Π can be expressed as follows (in units of J/m$^3$):

$$\Pi = -\frac{A}{6\pi h^3} \tag{2.10}$$

where $A$ is the Hamaker constant and the separation distance is represented by film thickness $h$.

## 2.4 Unanswered Questions

Atomic force microscope (AFM) has been widely used for direct force measurement of interactions between droplet and solid surface[19,77], as well as in droplet/droplet systems[28,31,32,78–80] including water-in-oil emulsions stabilized with asphaltenes[24,29,81]. It is now also possible to simultaneously measure dynamic force and spatiotemporal film thickness of a droplet/solid interaction based on recent reports with bubble/solid system.[82] However, the inherent limitation

of AFM studies is the low range of available approach velocities (0.2-50 μm/s) and droplet sizes (typically under 100 μm), which limits the hydrodynamic condition to low Reynolds numbers ($Re = 2\rho RV/\mu < 0.02$, where $R$ is the drop radius, $V$ is the droplet approach velocity, $\rho$ and $\mu$ is the density and viscosity of the continuous phase – toluene or *n*-heptane). Many industrial processes have much higher emulsified drop velocities, whose hydrodynamic condition cannot be adequately captured with AFM studies. To overcome this limitation, it is advantageous to use the Dynamic Force Apparatus (DFA), a custom instrument that can simultaneously measure spatiotemporal thin film drainage, interaction force and drop profile over a large range of precisely controlled approach velocities (2 μm/s - 50 mm/s).

In the case of a "contaminated" system, specifically as it relates to W/O emulsions encountered in bitumen production, the effect of well-controlled approach velocity at higher Reynolds hydrodynamic condition ($Re > 0.02$) on interfacial thin film drainage and emulsion stability is an under-explored area. Asphaltenes are some of the most surface-active species in bitumen, and due to (i) their ill-defined molecular structure and (ii) only a fraction of asphaltenes play a key role in emulsion stabilization,[1,53–57] it is helpful to study an idealized "contaminated" system where an asphaltene model compound is used (C5PeC11; can mimic certain aspects of asphaltene behaviour[50]). Specifically, the effect of approach velocity, temperature and substrate wettability on thin film drainage between a water drop and silica substrate in C5PeC11-in-toluene solution will be described in detail.

For "pure" organic systems, where a water drop interacts with a clean solid surface or another water drop in an organic solvent (toluene or *n*-heptane), there had been limited work to measure surface forces conducted to date, with many unanswered questions remaining. For example, what is the potential effect of water drop pH, salt concentration, drop and solid ageing in solvent, drop approach velocity, water saturation levels of the solvent, solid wettability and solid surface roughness on interaction forces of pure water/solid and pure water/water in organic systems? Similarly to the "contaminated" system discussed above, obtaining interaction force and spatiotemporal thin film drainage measurements with DFA will provide the ability to explore water/solid and water/water interaction in these non-polar systems at higher Reynolds hydrodynamic condition than that accessible with AFM.

# Chapter 3: Materials and Methods

## 3.1 Materials

Milli-Q purified water with a resistivity of 18.2 MΩ·cm at 22°C was used in all experiments and sample preparations, referred to simply as water henceforth. C5PeC11 was provided by Ugelstad Laboratory at Norwegian University of Sciences and Technology (NTNU). Hydrogen peroxide aqueous solution (30% w/w, ACS reagent) was supplied by Ricca Chemical. Sulphuric acid (95-98%, ACS reagent, Sigma Aldrich), toluene (99.8%, optima, Fisher), *n*-heptane (99.5%, optima, Fisher), *n*-octadecyltrichlorosilane (OTS, 95%, Acros Organics) and sodium hydroxide solution (NaOH, 1 N Certified, Fisher) were purchased from Fisher Scientific. Potassium chloride (KCl) of 99.9% purity (Sigma-Aldrich) was calcined in an oven at 580°C for 8 h to remove any impurities. All chemicals (except KCl) were used as received without further purification.

All glass volumetric flask and stoppers used to prepare solutions (KCl, NaOH, etc.) were cleaned in a base bath (1:1 v/v M KOH : ethanol) overnight and rinsed thoroughly with water. The pH of prepared NaOH solutions was verified by immersing a pH probe into a sub-sample of the solution. Water-saturated *n*-heptane and toluene were prepared by adding ~40 mL water to ~60 mL organic solvent, shaking vigorously by hand for 1-2 minutes, and allowed 24 hours to fully phase separate. The DFA cell was cleaned between experiments with detergent cleaning solution, followed by thorough rinse with water, dried with $N_2$ flow.

Finally, the cell was rinsed with organic solvent that is the continuous phase in a given experiments, and dried with $N_2$ flow prior to filling the cell with solvent. Fused silica discs (10x1 $mm^2$, 1 wavelength) and sapphire ($\alpha$-$Al_2O_3$) discs (10x1 $mm^2$, 1/4 wavelength) were purchased from Edmund Optics. Muscovite mica discs (10x0.2 $mm^2$, grade V1) were purchased from Ted Pella. Roughened fused silica was prepared by grinding substrate with 2000 grit sand (pre-wetted with water) paper for 2 minutes. Unmodified substrates are quite smooth; a surface's roughness can be characterized by RMS, or root mean square, $\text{RMS} = \sqrt{\frac{1}{n}\sum_{i=1}^{n} y_i^2}$, where $n$ is number of points, $y_i$ is the vertical distance from the mean line of $i$th data point. AFM images of several substrates and their RMS values are shown in Figure 3.1 below:

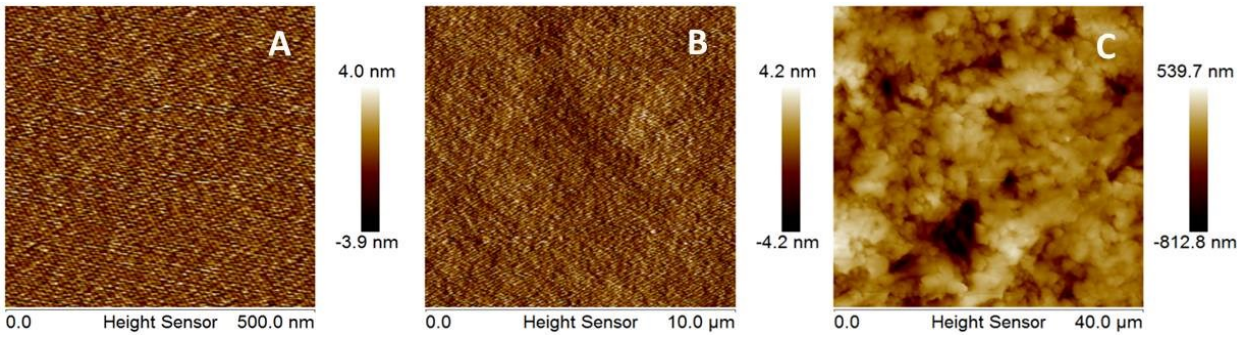


Figure 3.1 AFM images of (A) sapphire, (B) silica and (C) roughened silica, with RMS values of 1.15 nm, 1.21 nm and 166 nm, respectively.

Substrates used in this work include fused silica ($SiO_2$), sapphire ($\alpha$-$Al_2O_3$) and muscovite mica ($KAl_2(AlSi_3O_{10})(OH)_2$); the crystal structure for sapphire and mica are shown in Figure 3.2. Fused silica is a synthetic, non-crystalline (amorphous) form of silica that has superior UV transmission compared to crystalline quartz. Muscovite mica is composed of negatively charged aluminosilicate layers, with the negative charge, a result of the substitution of a quarter of the $Si^{4+}$ ions by $Al^{3+}$ ions. These aluminosilicate layers are kept together by electrostatically bound interlayer potassium cations, as shown in Figure 3.2(a).[83] Vectors a and b in Figure 3.2(a-b) define the {001} planes and vector c is the surface normal vector. The muscovite cell side-view (projection onto the a-axis) is shown in Figure 3.2(a), and the {001} surface top layer (projection onto the c-axis) is shown in Figure 3.2(b), indicating a hexagonal arrangement of Si (partly Al) and O atoms of a cleaved mica surface (residual $K^+$ ions not displayed).[83] Sapphire, or $\alpha$-$Al_2O_3$, is composed of oxygen layers in an ABAB stacking sequence, where Al atoms are bonded to six nearest-neighbour O atoms, with the O atoms bonded to four Al atoms in a distorted $sp^3$ arrangement.[84] The sapphire crystal structure, shown in Figure 3.2c, is a close-packed hexagonal array of O atoms, with Al atoms occupying two thirds of octahedral interstitial sites (one third remains empty as structural vacancies).[84]

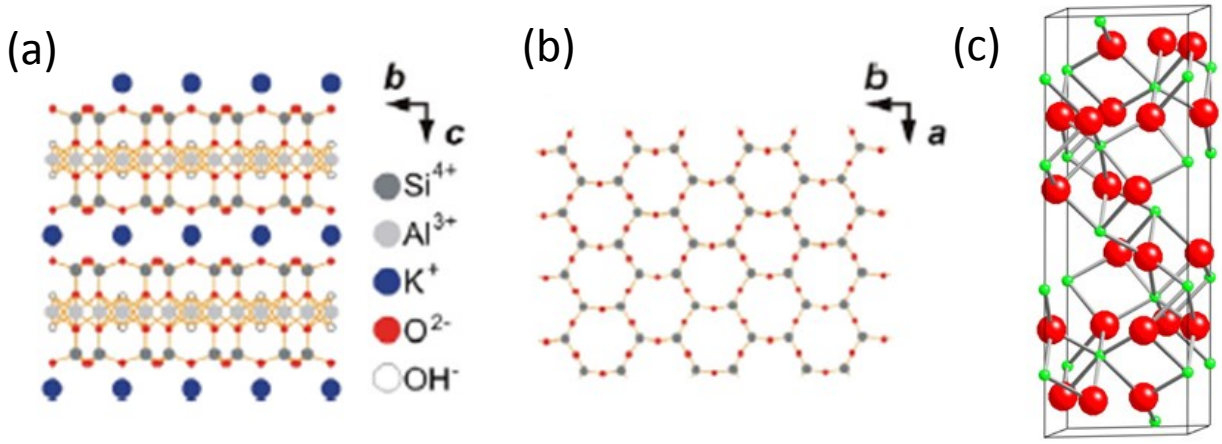


Figure 3.2 Crystal structure schematic for (a,b) muscovite mica[83] and (c) sapphire[85]. For sapphire, aluminum and oxygen atoms are shown in green and red, respectively.

### *3.1.1 Hydrophilic solid*

Silica substrates were cleaned in fresh piranha solution (3:1 v/v $H_2SO_4$ : 30% w/w $H_2O_2$) for 1-2 hours, followed by a rinse with water and several rounds of sonication in fresh water to remove any remaining traces of piranha solution. Such discs were completely water-wettable, with a contact angle of water in air of ~0°. These hydrophilic discs were kept submerged in water to maintain contact angle before running experiments. For pure system experiments (Chapter 4 and 5), the hydrophilic substrates were freshly cleaned on the day of experiments and used within hours to obtain reliable experimental results. For C5PeC11 experiments, the hydrophilic discs were used within hours to days of cleaning; this did not have any significant effect on experimental results. Roughened silica was cleaned with detergent and sonicated repeatedly in water before being cleaned in piranha solution for experiments.

Piranha cleaning did not work well for sapphire substrates (contact angle in air was ~20-25° and did not reach fully water-wettable state), and ~0° sapphire was instead prepared by: (1) cleaning with detergent, (2) air plasma (2 minutes/side at medium power, Harrick Plasma Cleaner) and (3) 30 minutes/side using UV/Ozone[86]. Freshly-cleaved hydrophilic mica was prepared by cleaning with plasma (2 minutes/side).

### *3.1.2 Hydrophobic solid*

Hydrophobic silica and sapphire discs were prepared by immersing the substrates in freshly prepared OTS/toluene solution: 2 minutes in 10% v/v for 107° (contact angle of water in air) and 1 minute in 0.1% v/v for 60° contact angle. The discs were then rinsed with copious amounts of toluene, acetone and water before being dried under nitrogen flow. Contact angle was verified for each substrate before use in experiments.

### *3.1.3 Contaminated system setup*

C5PeC11 was provided by Ugelstad Laboratory at Norwegian University of Sciences and Technology (NTNU) and was used as received.

## 3.2 System Characterization

### *3.2.1 Hamaker constant and disjoining pressure*

Based on Lifshitz theory,[87] the non-retarded Hamaker constant for two macroscopic phases 1 and 2 interacting across a medium 3 can be calculated according to Equation 3.1[88]:

$$A = \frac{3}{4}k_B T\left(\frac{\varepsilon_1-\varepsilon_3}{\varepsilon_1+\varepsilon_3}\right)\left(\frac{\varepsilon_2-\varepsilon_3}{\varepsilon_2+\varepsilon_3}\right) + \frac{3h\nu_e}{8\sqrt{2}}\frac{(n_1^2-n_3^2)(n_2^2-n_3^2)}{\sqrt{(n_1^2+n_3^2)}\cdot\sqrt{(n_2^2+n_3^2)}\cdot\left\{\sqrt{(n_1^2+n_3^2)}+\sqrt{(n_2^2+n_3^2)}\right\}} \quad (3.1)$$

where $\varepsilon_1$, $\varepsilon_2$ and $\varepsilon_3$ are the dielectric constants of the three media; $n_1$, $n_2$ and $n_3$ are the refractive indices for three media; $k_B$ is the Boltzmann constant, $1.38\times10^{-23}$ J/K; $T$ is the absolute temperature in Kelvin; $h$ is the Planck's constant, $6.626\times10^{-34}$ J·s; and $\nu_e$ is the main electronic absorption frequency in the UV region, in this work assumed to be the same for all materials ($3.0\times10^{15}$ $s^{-1}$). Calculated Hamaker constants relevant to the systems studied in this work are shown in Table 3.1:

Table 3.1 Calculated Hamaker constants (with relevant dielectric constants and refractive indices)

| Material | Dielectric Constant $\varepsilon$ | Refractive Index $n$ | Hamaker Constant $A$ (J) |
|---|---|---|---|
| Silica (fused)[88] | 3.8 | 1.458* | |
| Sapphire ($\alpha$-$Al_2O_3$)[88] | 10.1-11.6 | 1.77* | |
| Mica (muscovite)[88] | 5.4-7.0 | 1.60 | |
| Toluene[89] | 2.38 | 1.499 | |
| *n*-Heptane[88,90] | 1.92 | 1.385 | |
| Water[88] | 80 | 1.334 | |
| Water-toluene-silica | | | $2.40 \times 10^{-21}$ |
| Water-*n*-heptane-silica | | | $-4.02 \times 10^{-23}$ |
| Water-toluene-sapphire | | | $-9.00 \times 10^{-21}$ |
| Water-*n*-heptane-sapphire | | | $-2.89 \times 10^{-21}$ |
| Water-toluene-mica | | | $-2.89 \times 10^{-21}$ |
| Water-*n*-heptane-mica | | | $-1.32 \times 10^{-21}$ |
| Water-*n*-heptane-water | | | $3.49 \times 10^{-21}$ |
| Water-toluene-water | | | $9.84 \times 10^{-21}$ |

*Provided by Edmund Optics material specification.

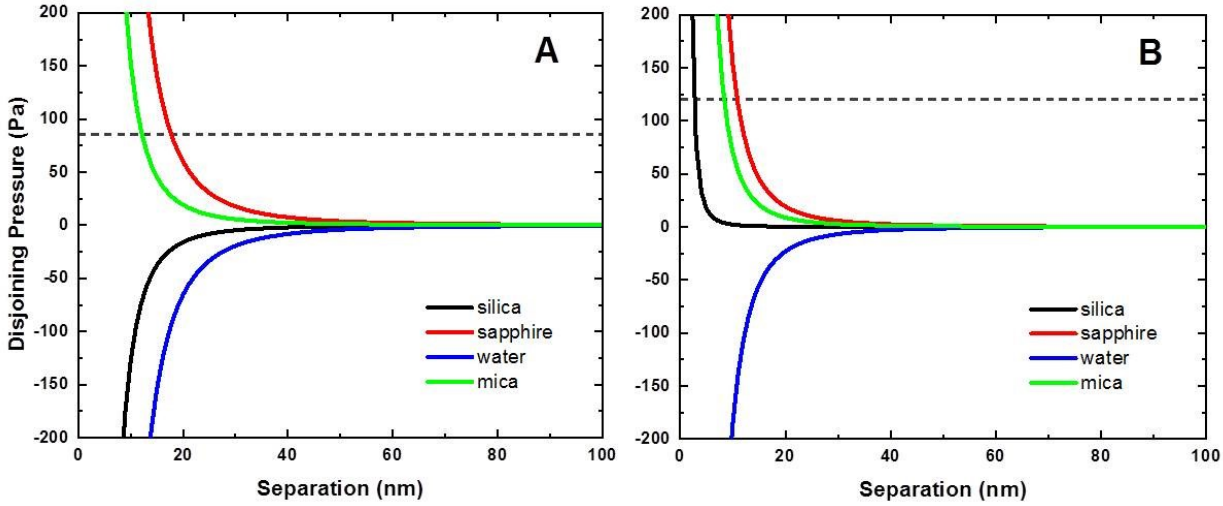


Figure 3.3 Disjoining pressure Π as a function of separation $h$ between a water drop and various materials interacting in (A) toluene and (B) *n*-heptane. The materials shown are silica (black), sapphire (red), water (blue) and mica (green). Dotted grey lines correspond to Laplace pressure inside the water drop for each solvent.

Average dielectric constants are used for Hamaker calculations in Table 3.1 for materials with a range of values (i.e. sapphire, mica). The disjoining pressure Π was calculated according to Equation 2.10 for all materials shown in Table 3.1, grouped by continuous phase solvent, and is shown in Figure 3.3. From Figure 3.3, both a repulsive ($\Pi > 0$) and attractive ($\Pi < 0$) interactions are expected for the systems in this work. The interaction of any substance with itself leads to attractive VdW force, hence the negative Π for water in both toluene and *n*-heptane. Sapphire and mica substrates are expected to result in a stable repulsive film at ~10-20 nm separation from the substrate surface in both toluene and *n*-heptane. For silica, the liquid film is expected to rupture in toluene as $\Pi < 0$, but a weekly repulsive disjoining pressure should lead to a very thin stable film at separations of ~3 nm in *n*-heptane. The Laplace pressure $P$ for a drop, as shown in Figure 3.3, can be calculated using Equation 3.2:

$$P = \frac{2\gamma}{R} \tag{3.2}$$

where $R$ is the droplet radius (0.85 ± 0.01 mm), $\gamma$ is the interfacial tension for water/toluene (51.0 mN/m) and water/*n*-heptane (36.5 mN/m), with resultant Laplace pressure of 120.0 Pa and 85.9 Pa for *n*-heptane and toluene, respectively.

While Equation 3.1 is an approximation from Lifshitz theory solution that, for example, only includes the first term in a sequence for London dispersion component and assumes the same $\nu_e$ for all materials, the resulting deviations in Hamaker constant calculations are reasonably small. In the case of water-toluene-water, the full solution to Lifshitz equations[29] results in deviations under 2% from value calculated in Table 3.1. As will be discussed in Chapters 4-5, the pure systems behave quite differently experimentally than what might be expected based on results shown in Figure 3.3.

### *3.2.2 Interfacial tension*

All interfacial tension measurements were performed using Theta optical tensiometer T200 (Biolin Scientific, Stockholm, Sweden). The tensiometer camera was calibrated prior to each measurement, and a 20 µL drop was generated using a gas-tight Hamilton syringe. Toluene and *n*-heptane values of 36.5 ± 0.2 mN/m and 50.8 ± 0.3 mN/m were obtained, in line with expected values of 36.5 and 51.0 mN/m at 22°C from the literature.[91,92] Interfacial tension measurements were performed for 0.1 g/L C5PeC11 in toluene solution at $T$ = 22°C and $T$ = 40°C, resulted in 27.5 mN/m and 26.5 mN/m values, respectively. The adsorption of C5PeC11 onto the water droplet surface was quite fast (over the course of seconds), after which time the interfacial tension value remained constant.

### *3.2.3 Contact angle*

All contact angle measurements were performed using Theta optical tensiometer T200 (Biolin Scientific, Stockholm, Sweden). The tensiometer camera was calibrated prior to each measurement. For contact angle measurements conducted in air, a transparent rectangular cuvette was used to cover droplet and substrate to avoid contact angle fluctuations due to evaporation and moving three-phase contact line.

### *3.2.4 Refractive index*

Refractive index of 0.1 g/L C5PeC11 in toluene solution was measured to be 1.49 using Abbe RMI refractometer (Exacta Optech, San Prospero, Italy). Due to the low concentration of C5PeC11 in solution, it is not unexpected that the value obtained is close to that of pure toluene[93]. Refractive indices for water and silica were obtained from the literature, as shown in Table 1. The effect of temperature on the refractive index is very small (typically on the order of $10^{-4}$; $10^{-3}$ for water[94]) and the same value is used for both $T$ = 22°C and $T$ = 40°C. All other refractive indices were used from the literature, as shown in Table 3.1.

### *3.2.5 Viscosity*

Viscosity of 0.1 g/L C5PeC11 in toluene solution was measured using a rheometer (TA Instruments, ARES-2G). The values obtained were 0.590 mPa·s at 22°C and 0.498 mPa·s at 40°C, in line with pure toluene.

## 3.3 Dynamic Force Apparatus (DFA)

### *3.3.1 Instrument design*

The Dynamic Force Apparatus,[71,95] or DFA, is a custom-built instrument which allows for the simultaneous measurement of spatiotemporal film thickness, dynamic force and macroscopic side-view video capturing the full parameters of the droplet/surface and droplet/droplet interaction. This instrument can measure simultaneously the spatiotemporal film thickness and interaction forces, at precisely controlled approach velocities (from 2 μm/s to 50 mm/s) not accessible by AFM. It has been used extensively to study bubble/solid[71,95,96] and bubble/bubble[97,98] interactions in aqueous systems. A schematic of the instrument[95] is shown in Figure 3.4.

An inverted optical microscope (Zeiss Axio Observer.D1m) was used to focus on the droplet/solid and droplet/droplet interface inside a stainless steel chamber. A monochromatic light source (546 nm, Zeiss HAL illuminator) shone on the interface during experiment resulted in observed Newton fringes, which were recorded using a high speed camera (Photron FastCam

SA4). They were converted into spatiotemporal film thickness $h(r,t)$ using mathematical relations developed and applied previously,[95,99] and discussed in more detail in section 3.3.4. The approach velocity of the capillary was precisely controlled by a motorized actuator up to 2.5 mm/s (ThorLabs Z825B) and by a speaker diaphragm above 2.5 mm/s. The velocity was independently verified by a real-time displacement sensor. The interaction force was measured by a piezoelectric bimorph. To control the initial size of the water droplet and record the approach and retraction during experiment, the interaction was recorded from a side viewing window using either a CCD camera (20 fps) or a high-speed camera (Photron FastCam SA4, 60–500,000 fps), depending on the accuracy required. All the experimental outputs (video from side and bottom cameras, signals from displacement sensor and charge amplifier) were synchronized with time through a custom-built LabVIEW program. More details about the DFA will be discussed in the next few sections.

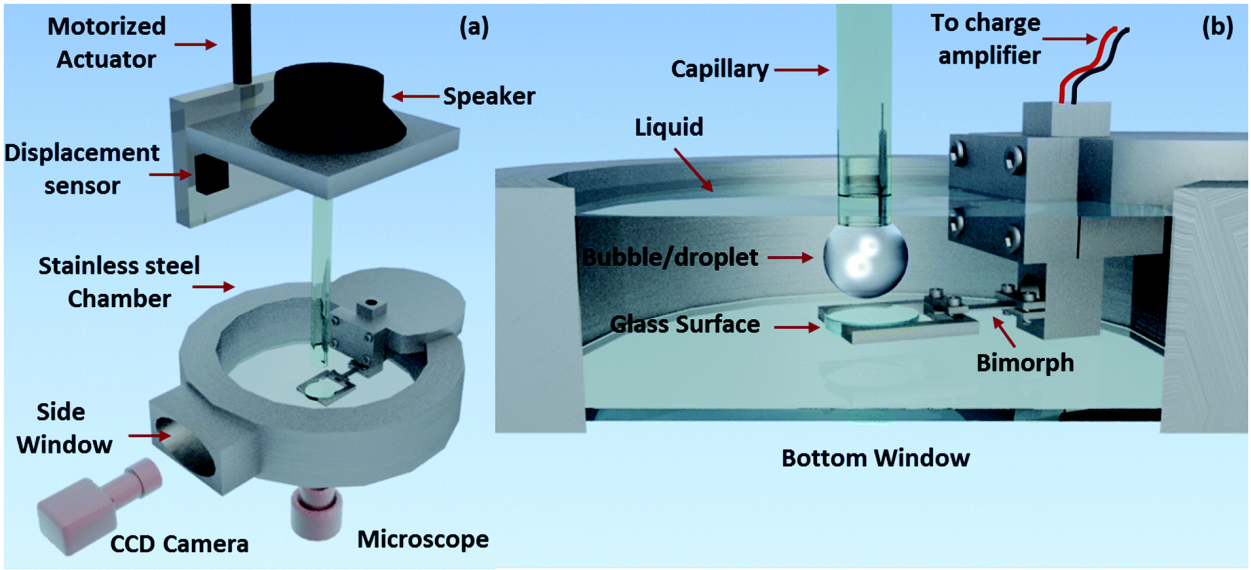


Figure 3.4[95] (a) Schematic illustration of DFA and (b) enlarged image of stainless steel chamber.

### *3.3.2 Displacement measurement*

The velocity from the motorized actuator is independently tracked by a displacement sensor, which provides the real-time velocity of the water droplet, and is essential for theoretical modeling of the dynamic drainage process. Two types of displacement sensors (sensitivity of

5 µm) were used: OMRON Z4D-F04A, which was later replaced with MicroEpsilon optoNCDT 1320. The optoNCDT 1320 has the advantage of a larger operable range (up to 5 mm) and does not require a voltage-distance calibration curve; the 0 and 5 mm positions are calibrated inside the LabView program, once the sensor was allowed to warm up for 20 minutes, which generates real-time displacement data in mm directly. For OMRON Z4D-F04A, a calibration curve was used to convert voltage signal into displacement, as shown in Figure 3.5 below:

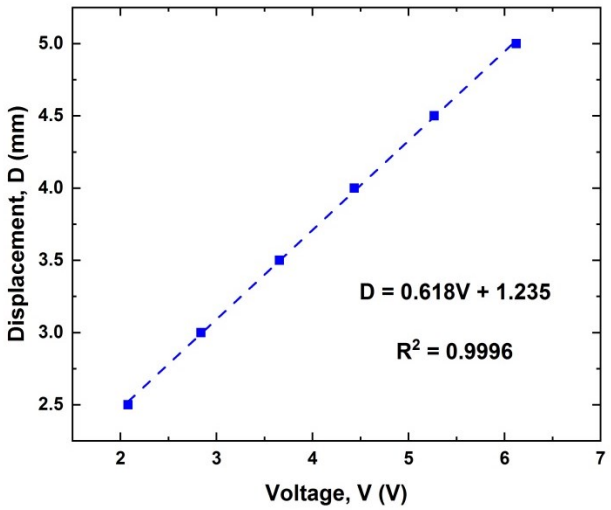


Figure 3.5 Calibration curve for the OMRON Z4D-F04A displacement sensor.

While the linear voltage-displacement range for OMRON sensor is 2.5 mm, irregular deceleration/acceleration voltage detection has been observed at the upper and lower extremes, limiting the true experimental range to between 2.7 and 4.8 mm, or 2.1 mm total.

### *3.3.3 Force measurement*

Dynamic force measurements were captured with a piezoelectric bimorph cantilever. The force of the droplet driven onto the solid surface causes a downward deflection of the bimorph, resulting in an accumulated charge. The piezoelectric bimorph, a bending-type force transducer, is made from two slabs of piezoelectric material glued together, with a schematic of the bimorph shown in Figure 3.6[100]:

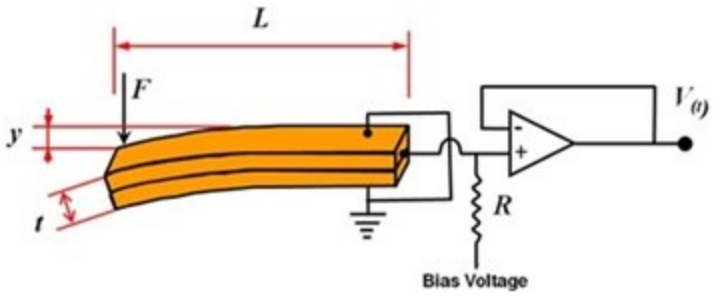


Figure 3.6 Schematic of piezoelectric bimorph.[100]

The applied force results in the compression of one slab and the expansion of the other. The charge generated from the deflection is given by Equation 3.3:[100]

$$Q = \frac{3FL^2 d_{31}}{2j^2} \tag{3.3}$$

where $Q$ is charge generated from bimorph deflection, $F$ is the applied force, $L$ is bimorph length, $j$ is bimorph thickness and $d_{31}$ is piezo material (lead zirconate titanate) charge constant. Since $L$, $j$ and $d_{31}$ are constant for a given bimorph, there is a linear relationship between applied force and charge ($Q = kF$). The bimorph can be modeled as a cantilever, with the force ($F$) and deflection ($y$) following Hooke's Law shown in Equation 3.4:[100]

$$F = \frac{L^3}{3EI} y \tag{3.4}$$

where $E$ is Young's Modulus and $I$ is the moment of inertia of the bimorph beam.

During a typical experiment, the change in voltage over time is recorded via LabVIEW program that can be converted to force using a calibration curve. Before beginning measurements, the bimorph needs to be equilibrated with the environment to minimize drifting of bimorph signal, which can be achieved by allowing the bimorph to remain on continuously for 1 hour prior to making measurement. The lead zirconate titanate bimorph (Fuji Ceramics Corp.) used here has

dimensions of 20×3×0.35 $mm^3$, capacitance of 21.5 nF, and a spring constant of 105 N/m for this experimental setup. The bimorph is enclosed in a thin flexible polytetrafluoroethylene (PTFE) sheath to prevent damage caused by contact with the reservoir fluid. Different weights in the range of 5-30 mg (pre-weighed pieces of platinum wire) were placed at the back, center and front ends of the substrate (along bimorph axis length-wise, where back is closest to the bimorph) to create three voltage/force calibration curves. This allowed for accurate interpretation of experimental results in different spots on the silica window. Only the central curve was used for all hydrophilic substrates as the water droplet covered all or a significant portion of the substrate once thin film rupture occurred and each substrate could only be used once in a given experiment. In Figure 3.7, the Voltage-Force calibration curves are shown below ($R^2$=0.999+), which allowed for the conversion of bimorph voltage signal into an interaction force:

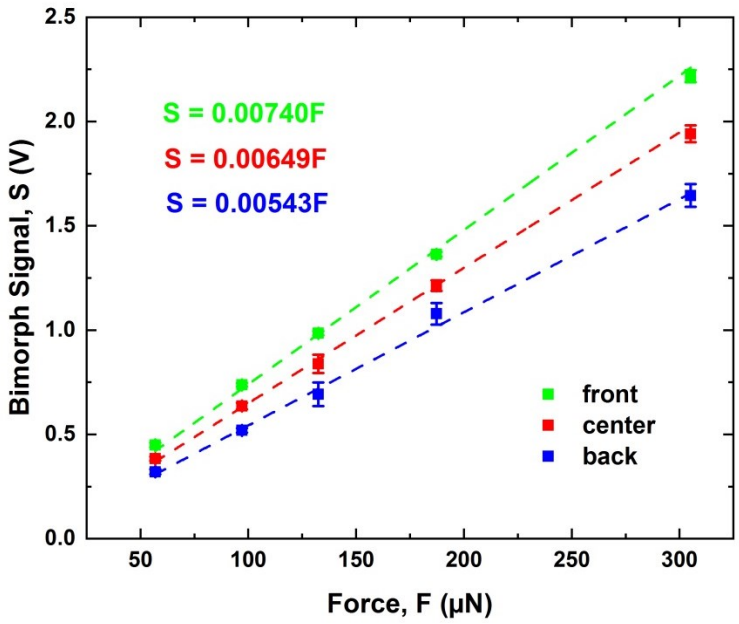


Figure 3.7 Bimorph voltage-force calibration curves at the front (green), center (red) and back (blue) of the substrate. Equation for each curve indicated in the corresponding colour.

The maximum voltage of ±7 V is accessible to the bimorph, and the correct gain should be selected depending on the experiment (lower gain is best for small forces, while a larger gain is best for large forces), with a consequent different voltage/force calibration. In this work, a

proportional gain of 50 and a cut-off frequency of 10,000 Hz were used for all experiments. It is important to note that if the bimorph setup is altered (e.g. replace bimorph sheath, adjust substrate holder, etc.) the bimorph needs to be re-calibrated. A more detailed calibration procedure can be found elsewhere.[101]

### *3.3.4 Film thickness measurement*

Monochromatic light (λ = 546 nm) from the bottom camera continuously illuminated the thin film, resulting in a series of interference fringes (Newton rings). The intensity of reflected light is measured with a low-noise Si-photodiode. Spatiotemporal film thickness $h(r,t)$ can be obtained through image analysis of the video frames using Matlab program based on Equations 3.5, 3.6 and 3.7 below[99]:

$$h(r,t) = \frac{\lambda}{2\pi n_2}\left(\frac{2m+1}{2}\pi - \frac{\delta}{2} \pm sin^{-1}\sqrt{\frac{\Delta}{1+4(1-\Delta)\dfrac{\sqrt{R_{12}R_{23}}}{\left(1-\sqrt{R_{12}R_{23}}\right)^2}}}\right) \tag{3.5}$$

$$\Delta = \frac{I(r,t) - I_{min}}{I_{max} - I_{min}} \tag{3.6}$$

$$R_{12} = \frac{(n_1 - n_2)^2}{(n_1 + n_2)^2} \quad \text{and} \quad R_{23} = \frac{(n_2 - n_3)^2}{(n_2 + n_3)^2} \tag{3.7}$$

where $\lambda$ = 546 nm is the wavelength of monochromatic light, $m$ is the order of interference ($m$ = 0,1,2..), $I(r,t)$ is the instantaneous light intensity, $I_{max}$ is the maximum light intensity, $I_{min}$ is the minimum light intensity, and $n_1$, $n_2$ and $n_3$ are the refractive indices of droplet (usually water), continuous phase (various organic solvents, including with addition of C5PeC11), and solid surface (fused silica, mica and sapphire), respectively. $\delta$ is the phase lag between incident and reflected rays, and can take the value of 0 or $\pi$. A phase change of $\pi$ occurs when light waves are reflected from the surface of a medium that has a higher refractive index than the

medium in which light waves are travelling in. All relevant refractive indices are listed in Table 3.1; $\delta = 0$ for all systems studied in this work except for the interaction of water with silica in toluene (with or without C5PeC11), where $\delta = \pi$ as $n_{toluene} > n_{silica}$. Using the $\Delta$ ratio helps account for background illumination,[102] allowing one to neglect random light fluctuations of outside sources, or the sides of the droplet.[64] An example of this process is shown in Figure 3.8 for the observed Newton rings during an interaction between a water drop and hydrophilic silica in 0.1 g/L C5PeC11-in-toluene solution. The original fringe is shown in Figure 3.8(a), which is converted into a grayscale intensity image, and the light intensity of the film extracted across one diameter (horizontal line in Figure 3-4a) through the Matlab code as shown in Figure 3.8(b). Equations 3.5, 3.6 and 3.7 are then used to generate the thin film profile, as shown in Figure 3.8(c). It must be noted that due to the small difference in refractive indices, as compared to the more commonly studied bubble/water/solid system, the interference fringes in this work do not appear as crisp as for the latter system. For recording speeds above 250 fps, a mercury lamp was used to obtain Newton rings with adequate brightness and contrast. In this work, for speeds below 5000 fps, the brightness of the mercury lamp needed to be reduced to avoid "bleaching" the image and was controlled with the shutter function of the PFV (Photron FASTCAM Viewer) software. That is, a higher shutter speed fraction results in reduced image brightness and in this work, shutter speeds of 1/5000 – 1/8000 were used.

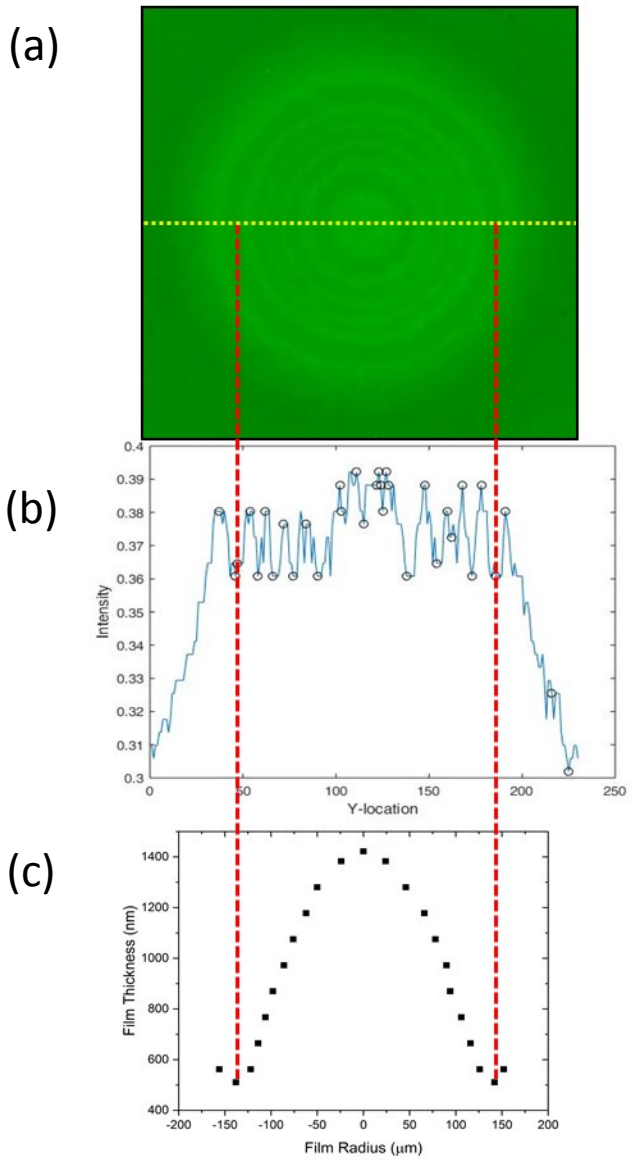


Figure 3.8 (a) Interference fringe at t=2.13 s between a water drop and hydrophilic silica surface in 0.1 g/L C5PeC11-in-toluene solution at 40°C and 1 mm/s drop approach velocity; 546 nm monochromatic light source used. (b) Instantaneous light intensity of horizontal yellow line in (a) as a function of film radius in pixels. (c) The generated film profile of (a), where vertical red line in all images corresponds to location of film rim.

### *3.3.5 Temperature control*

The cell used in this thesis is designed for precise temperature control. A stainless steel holder with channels throughout its perimeter was used, which allows the circulation of a temperature-controlled liquid (ethylene glycol in our experiments). A Haake recirculating thermostat was used to control the reservoir temperature. The transparent glass cell for reservoir fluid (7.5 x 3.6 x 3.6 $cm^3$) was placed inside the stainless steel cell, where 3 side holes and 1 bottom hole (2 cm in diameter) allowed the recording of macroscopic interaction (side-view camera) and Newton fringes (bottom camera). A thick PTFE lid cover was used to prevent reservoir evaporation and to maintain a constant temperature. This lid had a 1.5 cm diameter hole to allow for capillary movement (vertically and horizontally) during experiments. The reservoir temperature was given one hour to equilibrate (simultaneously, the bimorph was warming up, as described previously). The temperature of the reservoir was verified with a Digi-Sense thermocouple (Cole Parmer, Montreal, Canada) in several places and was found to be within ±0.5°C throughout the chamber.

### *3.3.6 DFA cell setup*

The glass cell was filled with a given organic solvent/solution and placed on a three-dimensional translation stage. The capillary tube was filled with fresh droplet solution (pure water or aqueous solution, depending on experiment), followed by an air layer before being immersed into the solvent. The air layer was used to generate a bubble, of equivalent height as desired water/aqueous solution drop, which was used to calibrate the location of the substrate (or water droplet on solid surface) prior to experiment. This bubble calibration step was necessary for the hydrophilic case, as any contact between water drop and substrate led to film rupture and deposition of water droplet on the surface.

# Chapter 4: Organic Systems – Liquid/Solid Interactions

## 4.1 Introduction

The time evolution of the water contact angle on hydrophilic silica and sapphire substrates (~0° contact angle) in-situ (submerged in toluene or *n*-heptane) was measured as a function of substrate exposure time to solvent (toluene or *n*-heptane) prior to deposition of water droplet and contact angle measurement. A given silica/sapphire substrate was placed inside a transparent cell with *n*-heptane or toluene for a specific period of time, after which a 9 μL drop of deionized water was deposited on the substrate in-situ and the contact angle measured for 5 minutes. Figure 4.1 shows the results for these in-situ water contact angle measurements. Toluene and *n*-heptane are shown in blue and red, respectively, with silica and sapphire distinguished by circle with dotted line and squares with solid line, respectively. The lines are drawn for eye guidance and all measured contact angle values remained constant over the 5 minute measurement time. Each data point represents a fresh substrate (that is, once the water contact angle was measured, this substrate was not re-used in further measurements unless it was rendered fully water-wettable (~°0) and the solvent immersion time started anew). It must be noted that in practice, it is difficult to measure 0° contact angle using the tensiometer, and typically ~0° is experimentally measured as 2-3°. From Figure 4.1, the effect of substrate hydrophobization related to solvent exposure time was much stronger for sapphire than for silica, and for both substrates, time spent in *n*-heptane (red) hydrophobized the substrate faster than toluene (blue). For sapphire, even 15 minutes of solvent exposure resulted in a water contact angle of 24° (toluene) and 58.5° (*n*-heptane). Was the observed substrate hydrophobization truly related to solvent exposure time? To verify this, ~0° silica and sapphire substrates were placed inside the measurement cell, a 9 μL water drop was deposited on the substrate surface, and solvent (toluene or *n*-heptane) was carefully added along the sides of the cell in order to not disturb the water droplet until the cell was adequately filled with solvent. The contact angle was measured over a 3 hour interval, and for all substrates and solvents, ~0° contact angle (2-4° in practice) was maintained during the entire solvent exposure time (3 hours) in all cases.

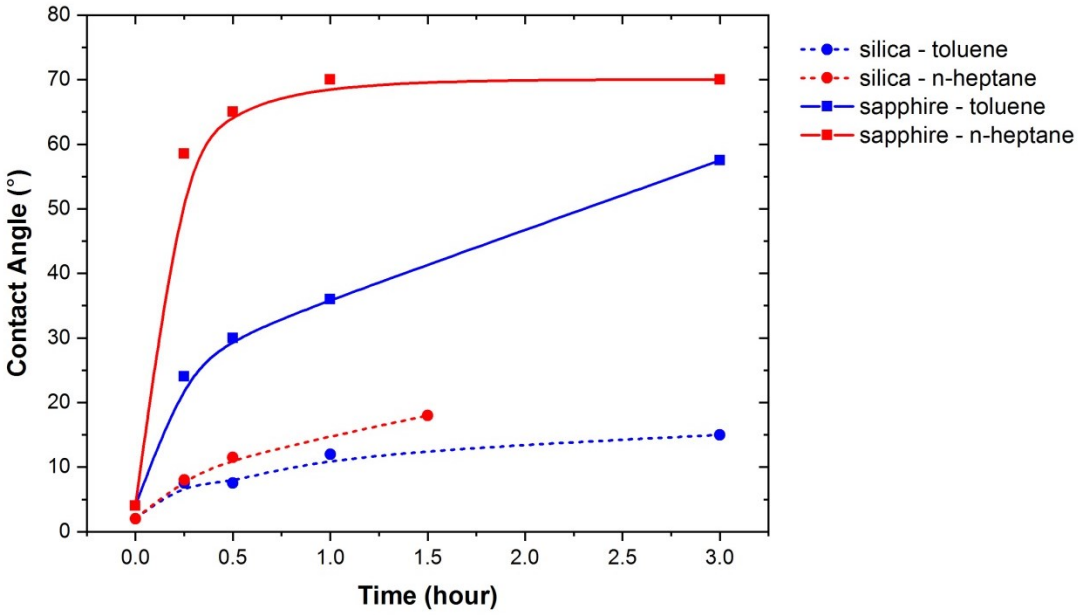


Figure 4.1 Contact angle of a water droplet deposited on silica (circle) or sapphire (square) substrates immersed in toluene (blue) or *n*-heptane (red), as a function of substrate immersion time in solvent prior to water droplet deposition.

In addition to in-situ results shown in Figure 4.1, the same type of experiment was repeated for water contact angle measured in air. A systematic study of water contact angle evolution of silica and sapphire (0°) was conducted after exposure to toluene and *n*-heptane over time. That is, after a given solvent immersion time, the substrate was removed, thoroughly dried with $N_2$ flow and a 9 μL droplet was deposited on the surface. The water contact angle was measured 3 times on the same substrate to check for repeatability (dry substrate with $N_2$ flow, re-deposit fresh water drop). Similar to in-situ experiments, a different substrate was used for each timed solvent immersion. In Figure 4.2, the water contact angle in air (red, black) and in solvent (purple; shown separately in Figure 4.1) is shown over time for ~0° silica in (A) toluene and (B) *n*-heptane, and ~0° sapphire in (C) toluene and (D) *n*-heptane. Green horizontal lines in Figure 4.2 indicate contact angle of water in air for regular silica (31°) and sapphire (38°) (did not undergo treatment to render surfaces hydrophilic). Error bars represent ±1*s* (standard deviation) for 3 successive contact angle measurements (black), with the first measurement indicated in red. In Figure 4.2(B), 40 hours refers to a sample at the last measured immersion time that was allowed to fully dry over 24 hours before measuring its final contact angle. The value (39°)

corresponds to the first contact angle measured at 16 hours shown in red. Successive measurements of contact angle using fresh water drops on the same substrate resulted in reduction of the contact angle, even with thorough drying between measurements. For this reason, the first contact angle measurement, shown in red in Figure 4.2, was assumed to be more representative of true water contact angle.

Agreement between contact angles measured in air and in solvent was generally good (Figure 4.2), with the exception of sapphire in *n*-heptane (Figure 4.2D). Here, hydrophobization effect in solvent occurred significantly faster than if the water contact angle was measured in air. Silica remained hydrophilic longer than sapphire; for both substrates, exposure to *n*-heptane increased the water contact angle faster than exposure to toluene. Only silica in toluene maintained full wettability during the first 30 minutes of solvent exposure; silica in *n*-heptane already measured 10° after 15 minutes of immersion time. At 15 minutes of immersion time, the contact angle of water on sapphire increased drastically, to 27° (toluene) and 31° (*n*-heptane), essentially returning sapphire contact angle to its untreated state (38°) by 30 minutes of solvent immersion time. Long-term exposure (16 hr) of sapphire to *n*-heptane increased the water contact angle to 60°. Based on results presented in Figure 4.1 and Figure 4.2, the solvent exposure time of a substrate prior to water droplet interaction in an experiment using DFA can have significant impact on the observed interaction force and will be discussed in more detail in the following chapters.

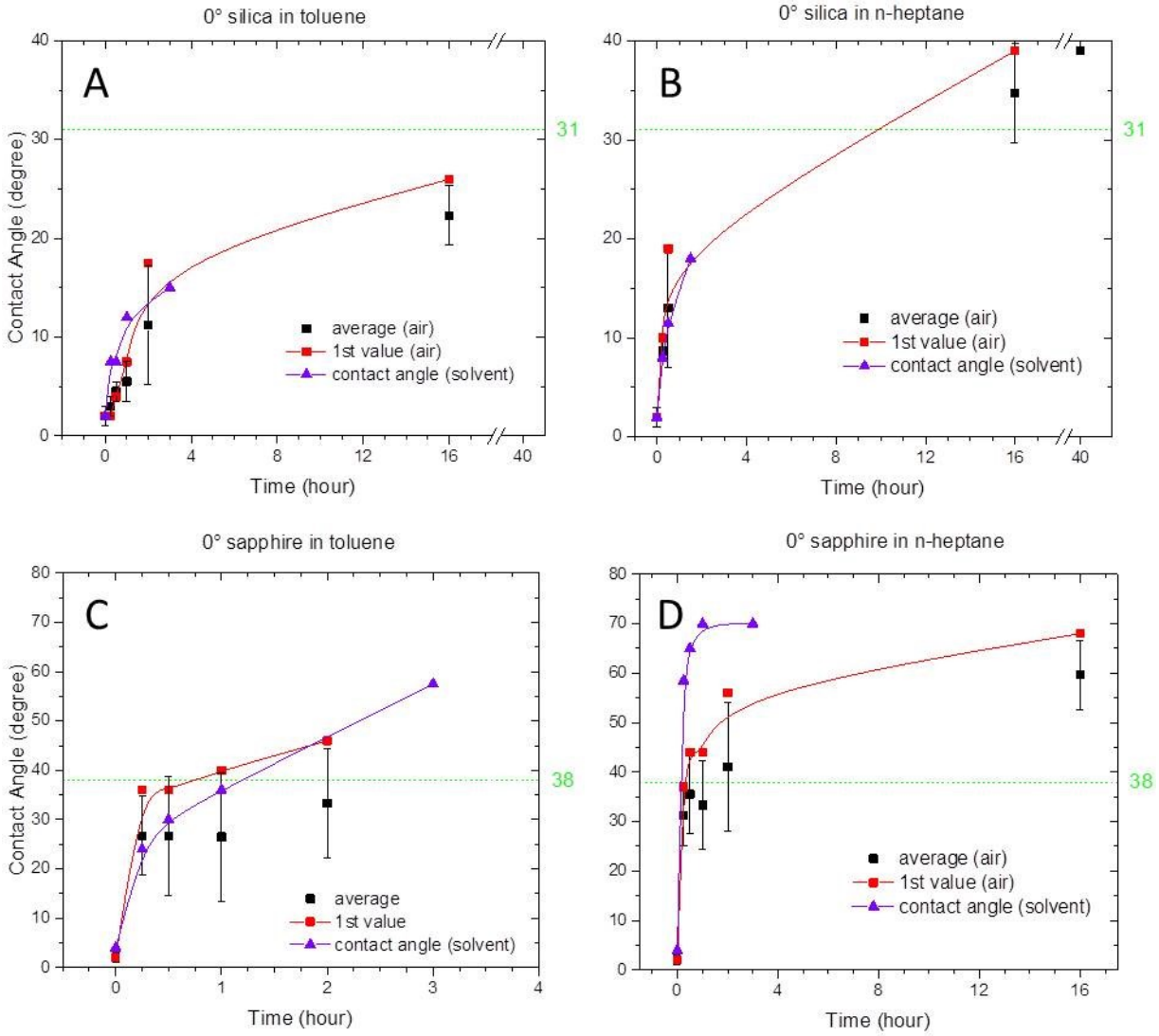


Figure 4.2 Comparison between change in water contact angle in air (red, black) and in solvent (purple) over time for ~0° silica in (A) toluene and (B) *n*-heptane, and ~0° sapphire in (C) toluene and (D) *n*-heptane. Green horizontal lines indicate contact angle of water in air for silica (31°) and sapphire (38°) substrates without any treatment to render surfaces hydrophilic; purple and red lines are shown as an eye guide.

## 4.2 Toluene

### *4.2.1 Water/silica*

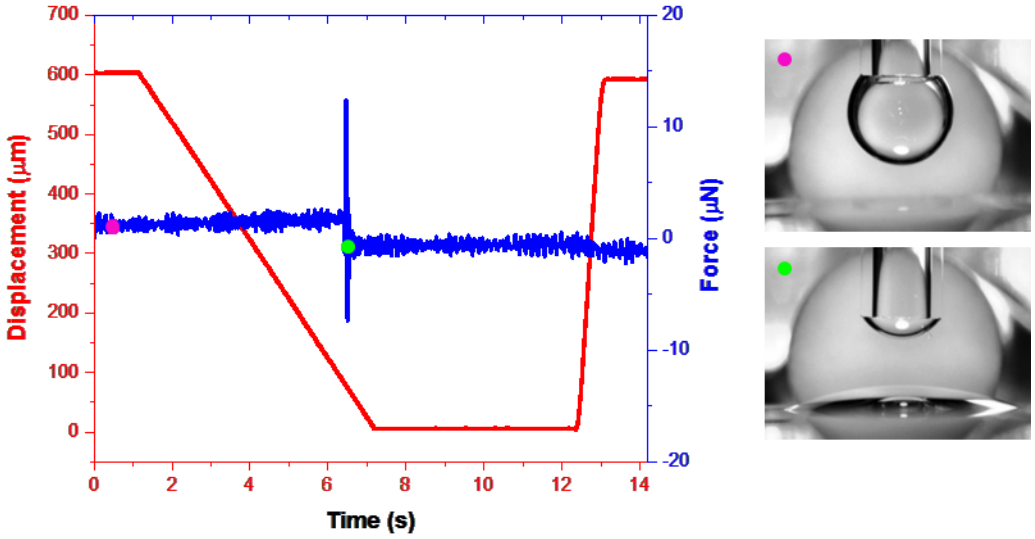


Figure 4.3 Displacement (red) and interaction force (blue), as a function of time, for a water droplet approached to 0° silica in toluene. Side-camera images are shown on the right, with corresponding times indicated with coloured dots on the force curve.

A typical interaction between a water drop and 0° silica substrate in toluene is shown in Figure 4.3. The total travel distance of the water drop was 600 μm with 100 μm overlap (that is, there was 500 μm between the bottom of drop and the silica surface at the start of the experiment). Figure 4.3 shows the force-displacement curve, where the force is shown in blue and displacement in red. The water drop began its descent toward the silica surface after 1 s holding period (pink dot side-camera image in Figure 4.3) at an approach velocity of $V = 0.1$ mm/s. The interaction force remained close to zero during the droplet descent, until the bimorph detected an interaction force when drop/silica contact occurred. In the case of freshly cleaned 0° silica, no discernable Newton Rings were observed from the inverted microscope, with near instant film rupture, followed by drop detachment from capillary in about 10 ms (green dot side-camera image in Figure 4.3). More interesting interaction phenomena were observed for the "contaminated" toluene/water system (in the presence of model asphaltene compound C5PeC11)

and will be discussed in in Chapter 6. The remainder of this chapter will focus on water/substrate interactions in *n*-heptane.

## 4.3 *n*-Heptane

### *4.3.1 Water/silica*

#### *4.3.1.1 Effect of substrate ageing time*

How important are the findings of changing contact angle of water on silica based on *n*-heptane exposure time, as shown previously in Figure 4.1 and Figure 4.2? As it turns out, it is one of the critical pieces related to the observation of a very long-range attractive force. A typical force and displacement curve for a water droplet in *n*-heptane approached to a 0° silica substrate that has been aged (exposed to *n*-heptane) prior to experiment is shown in Figure 4.4.

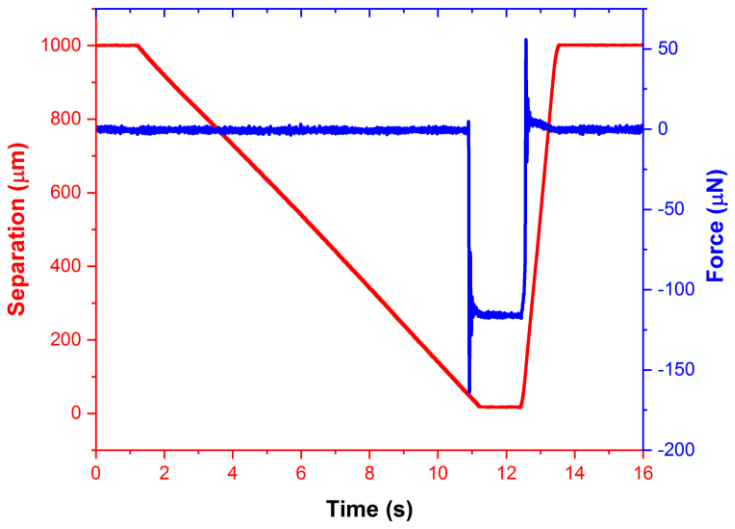


Figure 4.4 Effect of ageing time on interaction force between water and 0° silica in *n*-heptane: no long-range attractive force was observed; high silica exposure time in *n*-heptane prior to experiment and silica substrate treatment with piranha 5 days prior to experiment.

The separation of the bottom of the water droplet and the silica disc surface was 1000 μm (shown in red), with an approach velocity of the water drop at $V = 0.1$ mm/s. No long-range attractive force (shown in blue) was observed, and instantaneous rupture occurred on contact with no

Newton fringes observed at 3600 fps imaging (film lifetime was less than 0.3 ms). Silica substrate was exposed to *n*-heptane in the DFA cell for 100 minutes prior to starting the experiment, and the water droplet was fresh (the experiment was started within seconds of the droplet being generated; this is done by releasing bubble layer inside the capillary separating *n*-heptane continuous phase from water column inside the capillary). In this experiment, silica substrates were cleaned 5 days prior to use and stored submerged in deionized water. From side-view camera images, the contact angle of ruptured water drop on silica was much higher than expected and the water droplet remained attached to the capillary after film rupture. The contact angle of water in air on the silica substrates cleaned 5 days prior in piranha was measured at ~0°. To eliminate this issue, all substrates were freshly cleaned in piranha and used within hours for experiments, and solvent exposure time of silica to *n*-heptane prior to experiment was also closely monitored.

With careful experimental setup, including freshly cleaned silica substrates and minimization of silica substrate exposure time to *n*-heptane prior to water droplet approach, a very different experimental result was observed, as shown in Figure 4.5. In Figure 4.5A, the displacement (red) and interaction force (blue) curves are shown as a function of time for a water droplet driven toward a 0° silica surface in *n*-heptane; with side-camera images of the water droplet at $t = 0$ (Figure 4.5B) and at $t = 18.268$ s, where the elongated water droplet made contact with silica substrate surface (Figure 4.5C). Unlike the case shown in Figure 4.4, there was an observed extra long-range attractive force that resulted in downward elongation of the water droplet towards the silica surface prior to any physical contact between droplet and surface. This elongation was followed by a drop "jump-in" (top drop detachment from the capillary onto the silica substrate), where the water drop quickly detached from the capillary and spread on the silica surface. Here, the total travel distance, or displacement, of the water drop was 2100 μm, with 100 μm overlap (that is, there was 2000 μm between bottom of water drop and silica surface at the start of the experiment), at an approach velocity of $V = 0.1$ mm/s. The silica disc was cleaned in piranha on the day of the experiment and was used within hours. The exposure time of the silica disc to *n*-heptane prior to approaching the water drop was 32 minutes; the water droplet was used within seconds of being generated. The side and bottom cameras were recording the experiment at 1000 and 4500 fps, respectively.

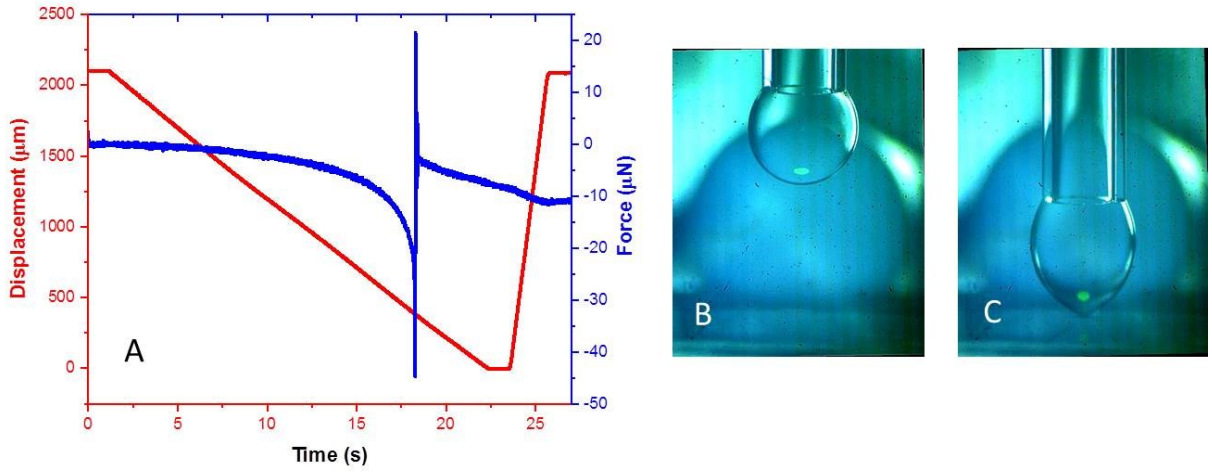


Figure 4.5 (A) Displacement (red) and interaction force (blue), as a function of time, for a water droplet approached to 0° silica in *n*-heptane; side-camera image of water droplet: (B) $t = 0$ and (C) $t = 18.268$ s, where elongated water droplet contacts the silica surface.

The force curve presented in Figure 4.5A was generated by processing the bimorph signal using two levels of Savitsky-Golay (SG) smoothing, as shown in Figure 4.6. In Figure 4.6A, 2000 points SG smoothing curve (red) is overlaid on a 400 points SG smoothing curve (black). Using a large point count (2000) resulted in under-estimation of the measured force during film rupture and droplet detachment from the capillary, thus using a lower point SG (400) was necessary during this part of the interaction to preserve the original force signal. This is demonstrated more clearly in the zoomed-in area of the force curve in Figure 4.6B. It should be noted that in order to maintain stable bimorph signal during experiment but also minimize and precisely control silica solvent exposure time, the bimorph was allowed to equilibrate with the environment for over 1 hour, briefly disconnected in order to add silica disc onto holder, and then immediately re-connected upon submersion in solvent inside DFA cell.

Returning to Figure 4.5A, the bimorph detected an attractive force as soon as the droplet started moving at $t = 1.22$ s, indicating the range of the observed attractive force is at least 2000 µm. Changes in water drop dimensions (height and width) were measured by analyzing side-camera images. While there was an immediate detection of an interaction force by the bimorph, droplet elongation was not visible from side-camera images until $t = 9$ s ($D = 1292$ µm, $F = -2$ µN). As

the water drop was driven closer to the silica surface, it progressively increased in length, or elongated, and decreases in width, with half of the total drop elongation occurring during 55 ms preceding droplet/silica contact.

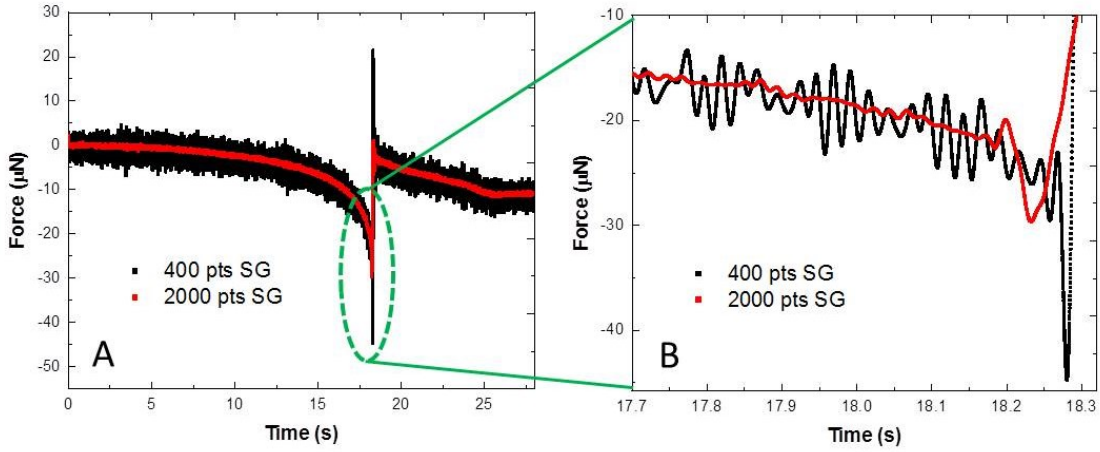


Figure 4.6 The impact of Savitsky-Golay (SG) choice of smoothing point number on interaction force curve between water droplet and silica in *n*-heptane (A – full force curve, B – water droplet elongation prior to detachment), where 400 and 2000 points SG are shown in black and red, respectively.

At surface contact (Figure 4.5C), the drop width had decreased by 4.7% and the drop length had increased by 20.3%. Contact occurred at $t$ = 18.268 s ($D$ = 383 μm, $F$ = -23.1 μN), with rupture observed immediately after from the side-camera at $t$ = 18.269 s ($D$ = 383 μm , $F$ = -23.3 μN); from the bottom camera, the film had a lifetime of 0.22 ms, including a tiny Newton ring visible at $t$ = 18.2684 s. The graphic representation of water drop elongation and consequent rupture for this system is illustrated in Figure 4.7, where side-camera images are shown for the various steps of the water drop interaction with 0° silica in *n*-heptane: drop elongation (a-f), drop/silica contact (g), film rupture (h) and drop "jump-in" (g-q). Drop "jump-in" time is defined as the time between drop/surface contact and detachment from the capillary. The corresponding time stamp, in seconds, is shown in the top left corner for each side-camera image in Figure 4.7. The high affinity of water to the 0° silica surface resulted in fast spreading of water on the silica surface after rupture, quickly overcoming the cohesive energy of the water droplet and leading to an

observed drop jump-in time of 10 ms. In Figure 4.8, the droplet elongation (green) is plotted as a function of distance to the silica surface in red (Figure 4.8A) and interaction force in blue (Figure 4.8B). The displacement curve in Figure 4.5 includes a 100 μm overlap, and for this reason the distance to the surface in Figure 4.8 starts at 2000 μm versus the 2100 μm total displacement

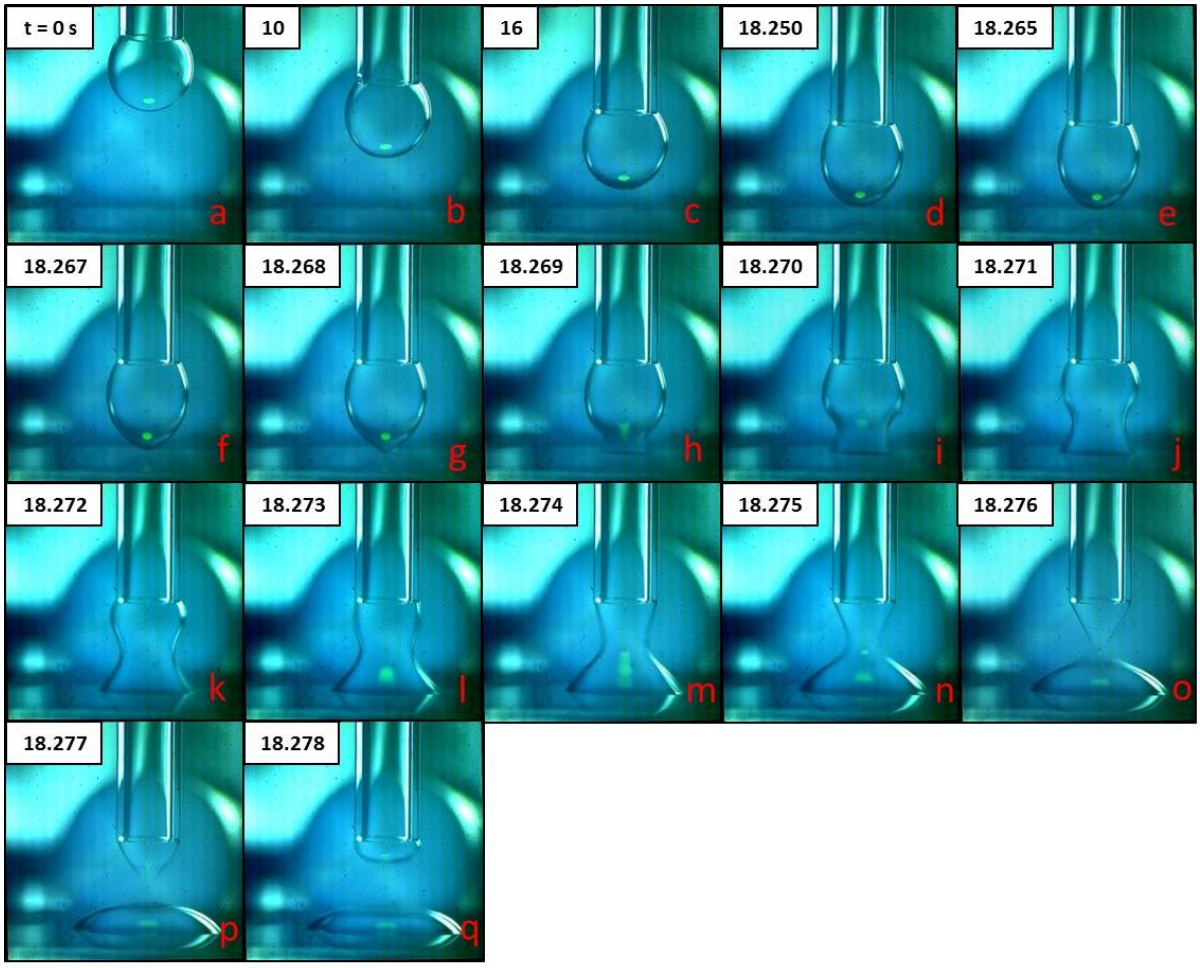


Figure 4.7 Side-camera images of water interaction with 0° silica in *n*-heptane: drop elongation (a-g), film rupture (h) and drop "jump-in" (g-q). Time stamps, in seconds, are shown in the top left corner for each side-camera image.

shown in Figure 4.5. From the distance curve, there was 283 μm remaining between (undeformed) drop and silica surface at $t$ = 18.268 s, which is reasonably close to the value of droplet elongation obtained from the side-view camera images (297 μm), given that 1 pixel is 7.26 μm in the side-camera images. In total, on contact with the silica surface, the drop had

elongated by 20.3%, with a reduction in width by 4.7%, as compared with an undeformed drop at the beginning of the experiment. The undeformed drop height for all systems was 1.47 ± 0.03 mm, measured from capillary edge to bottom of drop. From Figure 4.8B, it is clear most of the drop elongation occurred in a short time preceding drop/silica contact: 50% of total drop elongation occurred within 68 ms prior to drop/surface contact, with 25% of drop elongation occurring during 3 ms prior to surface contact (at this stage, water drop elongated into a pointed spheroid, as shown in Figure 4.7(e-g)). After film rupture, the force rapidly decreased to -42.2 μN at $t$ = 18.278 s ($D$ = 382 μm), when drop jump-in occurred (Figure 4.7q) and the force returned to ~-2.9 μN once the bimorph stabilized. Interestingly, from Figure 4.5A, the attractive force continued to increase as the capillary continued its descent, including during the 1 s hold at $D$ = 0 prior to capillary withdrawal at 1 mm/s. The force remained stable at -11 μN during the final 1 s hold once the capillary was withdrawn to its original position at $D$ = 2100 μm.

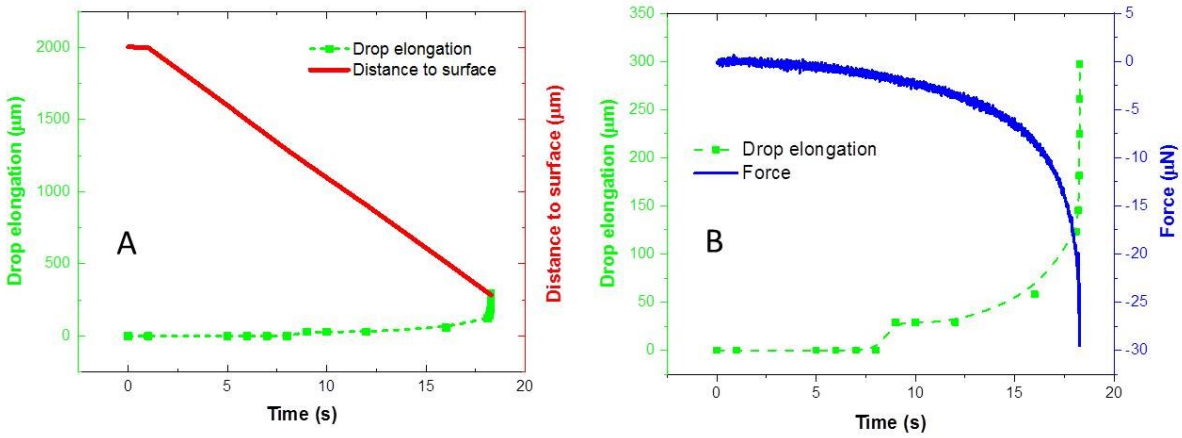


Figure 4.8 Water drop elongation (until surface contact; green) over time, interacting with 0° silica in *n*-heptane, as a function of: (A) Distance to the silica surface (based on undeformed drop; red) and (B) Interaction force (blue).

*4.3.1.2 Effect of water droplet ageing time*

The effect of water droplet exposure to *n*-heptane on drop elongation and interaction force was tested for a 0° silica substrate (exposed to *n*-heptane for 32 minutes). The data presented in the previous section (fresh water droplet) is here compared with a water droplet that has been "aged"

in *n*-heptane for 15 minutes prior to the experiment (water drop was generated at 17 min silica exposure to *n*-heptane and aged until the experiment start time at 32 minutes). The results are shown in Figure 4.9, where the total travel distance of the water drop was 2100 μm with 100 μm overlap (with an initial separation of 2000 μm between the bottom of the water drop and the silica surface at the start of the experiment).

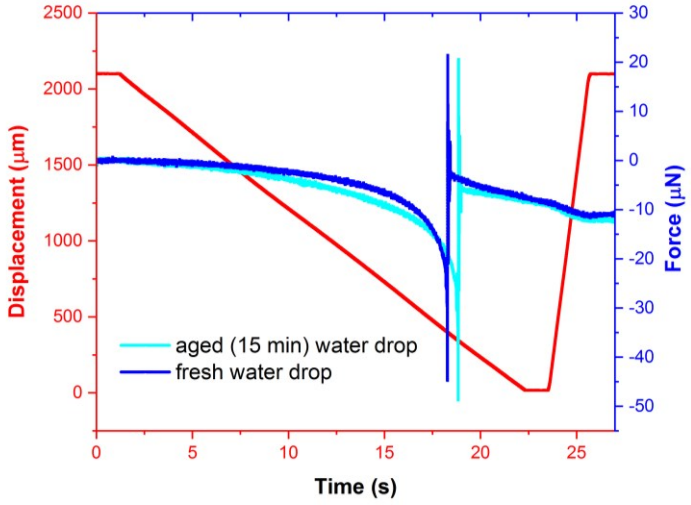


Figure 4.9 Displacement (red) and interaction force (aged water drop - cyan, fresh water drop - blue), as a function of time, for a water droplet approached to 0° silica in *n*-heptane.

As before, brand new silica discs were used in this experiment, cleaned in piranha and used within hours of cleaning. Bimorph began detecting attractive force at $t$ = ~1.22 s, or as soon as the droplet started moving, and at 2000 μm away from surface. The water drop progressively elongated, until the bottom "funneled" down to the surface at $t$ = 18.827 s ($D$ = 345 μm, $F$ = -28.1 μN ), with film rupture at $t$ = 18.828 s (from the inverted microscope, contact occurs at 18.827333 s, with several small newton rings before rupture at $t$ = 18.828222 s; $D$ = 345 μm, $F$ = -29.0 μN) and the drop jump-in at $t$ = 18.837 s ($D$ = 344 μm, $F$ = -44.8 μN). Figure 4.10 shows the force curve during drop contact and jump-in, with side-camera images labeled as pink and blue dots, respectively, on both the images and force curve. The maximum attractive force ($F$ = -48.8 μN) was slightly larger here than for the un-aged water drop ($F$ = -44.8 μN). Why this is the case is not clear, it may be related to the slight difference in water droplet height at the

beginning of experiment (1416 μm vs. 1459 μm for aged and fresh water drop, respectively); the aged water droplet appeared to shrink slightly in size after 15 minutes of ageing ($R$ = 0.83 mm). The difference in drop height is also related to the difference in surface contact time: 18.827 s vs. 18.268 s (at $V$ = 0.1 mm/s, the time difference corresponds to an extra 56 μm travel). The drop width decreased by 4.8% and the drop height increased by 20.5% at contact/rupture. This is very similar to the un-aged water drop (decreased by 4.7% and drop length had increased by 20.3%; section 4.3.1.1), indicating that the drop ageing did not impact drop elongation, with the substrate solvent exposure time being the most important factor. However, unlike the case of a fresh drop, the observed film lifetime before rupture for an aged drop was longer (1.1 ms vs. 0.2 ms).

It is interesting to note a continued decrease in the force in Figure 4.9 after drop detachment, which stabilized at ~-11 μN once the capillary returned to the original position. As shown in the last image of Figure 4.10, a residual water drop was left on the substrate after detaching of the water drop from the capillary. Such drop would exert a gravity force on the bimorph to appear as a "repulsive" force. This bimorph behaviour is system-dependent, and is different from some of the other systems in the literature: an "attractive" force was detected by the DFA bimorph in (a) bubble/bubble[101] interactions if coalescence occurred with a large bubble resting on the substrate, caused most likely by lifting force of residual bubble or droplet under buoyancy effects[101] and in (b) bubble/solid[95, 101] or drop/drop[101] interactions after three-phase contact line formation (in the case of thin film rupture). Although the measured forces were reproducible most of the time (75% time) for the current system, the measured long-range interaction forces could vary significantly sometimes due to complex nature of the system. Since the measured forces are extremely sensitive to the contamination, keeping everything (apparatus, substrate, solvent, water, etc.) clean is a well-recognized challenge for the current system, and the observed variation for certain cases is not unexpected and will not be discussed further in this chapter. It is also worth noting that the long-range attractive force observed here and elsewhere in Chapters 4 and 5 is not caused by any hydrostatic effects. The DFA instrument had been used extensively to study interaction forces in aqueous systems,[95-98,101] with no force detected due to drop/bubble capillary motion outside the hydrodynamic and disjoining pressure interaction zone near the

surface. Similarly, no hydrostatic effects were observed when a long-range attractive interaction was absent for organic systems, as shown previously in Figure 4.3 and Figure 4.4.

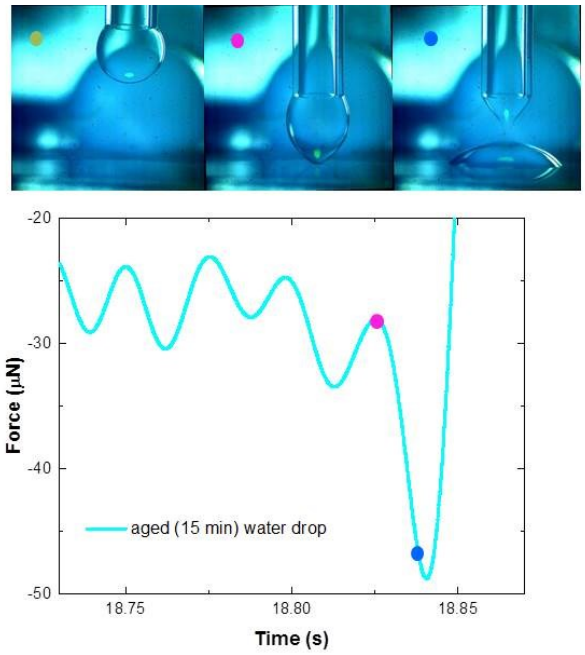


Figure 4.10 Force curve as a function of time, for a water drop (aged 15 minutes) approached to 0° silica in *n*-heptane, with corresponding side camera images (indicated with matching coloured dots on the force curve): $t = 0$ s (green); $t = 18.827$ s (pink); $t = 18.837$ (blue).

*4.3.1.3 Effect of water saturation of n-heptane*

To compare experimental results for the effect of water saturation level of *n*-heptane on the interaction of a water droplet with a 0° silica substrate, the data needed to be normalized to a common, lower displacement level. Namely, results discussed previously for pure *n*-heptane (see Figure 4.5) were conducted at 2000 μm from silica surface ($D = 2100$ μm), while experiments for *n*-heptane saturated with water were conducted at 1500 μm from silica surface ($D = 1600$ μm). The procedure for a typical normalization is demonstrated in Figure 4.11. Time was redacted by -5.9578 s (where $D = 1600$ μm), with the 1.22 s added back to account for initial stationary hold (1 s hold setting resulted in observed droplet motion starting at 1.22 s). With initial time changed to $t = -4.7378$ s, the new displacement curve now starts at $D = 1600$ μm when $t = 1.22$ s. For the force curve, in addition to time adjustment, the value of the detected

force was modified to begin at zero before the droplet motion began. In Figure 4.11, at $t = 5.9578$ s, the detected force was -0.6817 µN. Thus, 0.6817 µN was added to the force curve, with the normalized force curve now showing $F = 0$ at $t = 1.22$ s. In this way, the droplet contact distance was maintained ($D$ = 383 µm or 283 µm from silica surface), with the time and force curves modified accordingly.

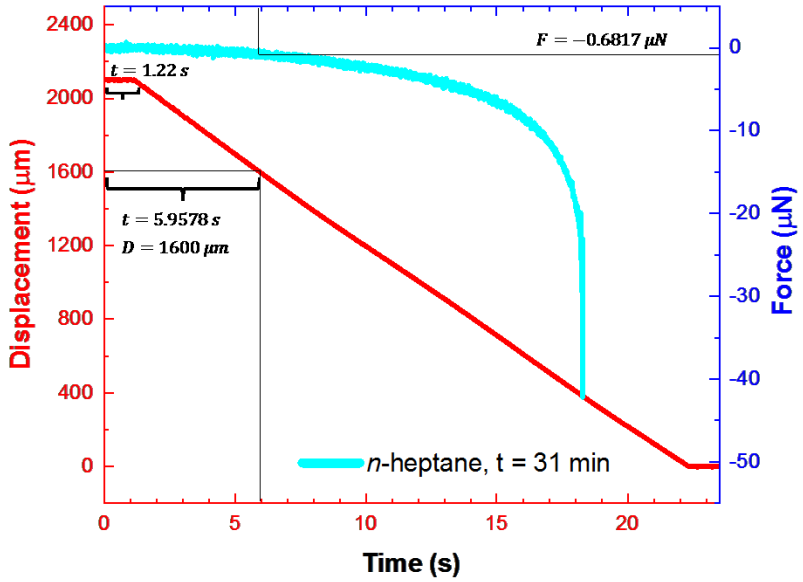


Figure 4.11 Displacement (red) and interaction force (cyan), as a function of time, for a water droplet approached to 0° silica in regular *n*-heptane. Necessary scaling parameters for time and force to modify starting point from 2100 µm to 1600 µm indicated on the graph.

The normalized curve from Figure 4.11 for regular *n*-heptane is plotted with results of the same water drop/silica system conducted in water-saturated *n*-heptane, as shown in Figure 4.12. Silica exposure time to solvent prior to experiment was the same in both cases (32 min for regular *n*-heptane and 31 min for water-saturated *n*-heptane). Water-saturated and regular *n*-heptane are shown in blue and cyan, respectively, with displacement for both cases indicated in red. In Figure 4.12, the full drop/silica interaction curves are shown on the left (A), with the enlarged contact/rupture region shown on the right (B). Drop/silica contact and jump-in are indicated with pink dots and yellow arrows, respectively.

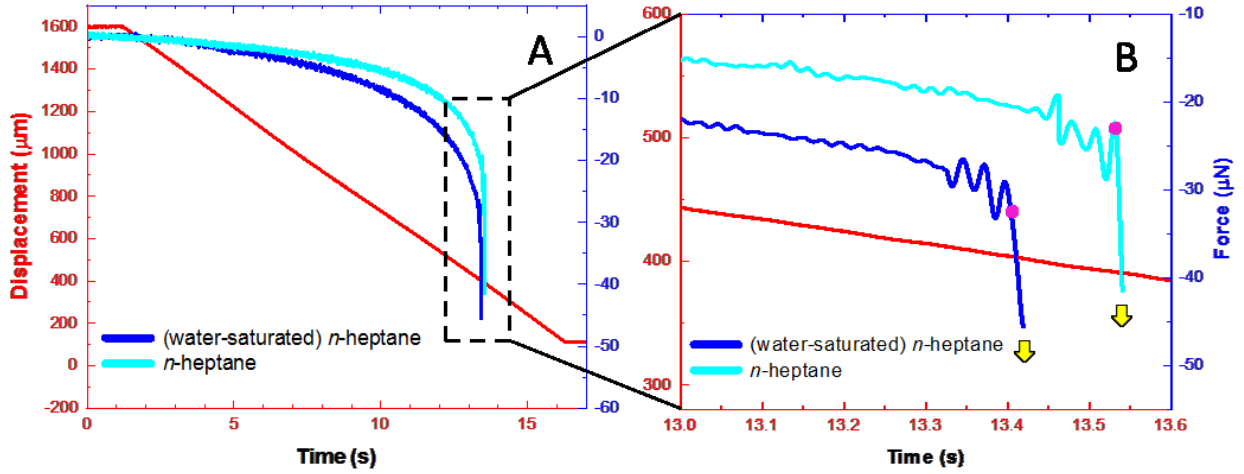


Figure 4.12 Displacement (red) and interaction force (blue, cyan), as a function of time, for a water droplet approached to 0° silica in *n*-heptane: (A) original curves, (B) enlarged contact/rupture. Water-saturated and regular *n*-heptane force curves are shown in blue and cyan, respectively. Drop/silica contact and jump-in are indicated with pink dots and yellow arrows, respectively.

For regular *n*-heptane (cyan curve), the drop elongated during the descent, with drop/silica contact at $t$ = 13.530 s ($D$ = 383 μm, $F$ = -22.4 μN), followed by film rupture at $t$ = 13.531 s ($D$ = 383 μm, $F$ = -22.6 μN) and drop jump-in at $t$ = 13.540 s ($D$ = 382 μm, $F$ = -41.5 μN). As discussed previously in section 4.3.1.1, the drop had elongated by 20.3%, with a 4.7% decrease in drop width. In the case of *n*-heptane saturated with water (blue curve), drop/silica contact occurred sooner, as a consequence of larger droplet elongation. Similar to regular *n*-heptane, the water drop progressively elongated during descent, with drop/silica contact observed at $t$ = 13.408 s ($D$ = 403 μm, $F$ = -32.6 μN), followed by film rupture at $t$ = 13.409 s ($D$ = 403 μm, $F$ = -34.3 μN) and drop jump-in at $t$ = 13.418 s ($D$ = 402 μm, $F$ = -45.6 μN). In water-saturated *n*-heptane, the water drop elongated by 22.0% and decreased in width by 6.4%. In both cases, drop elongation mostly occurred in close proximity to the surface. For example, about a third of total droplet elongation was observed 5 ms prior to drop/silica contact (120 μm and 109 μm for saturated and regular *n*-heptane, respectively), and 50%+ total elongation within 50 ms prior to drop/silica contact (205 μm and 145 μm for saturated and regular *n*-heptane, respectively). In the 5 ms and 50 ms intervals, the capillary covered a distance of 0.5 μm and 5 μm, respectively,

indicating that the droplet elongation in the final stages did not cover a large displacement range of the system. Water saturation of *n*-heptane leads to stronger droplet elongation (22.0% vs. 20.3%), as well as steeper attractive force curve during capillary displacement and larger attractive force on drop/silica contact (-32.6 μN vs. -22.4 μN).

The effect of silica exposure time in water-saturated *n*-heptane on the interaction force is shown in Figure 4.13: displacement (red) and interaction force (blue, cyan, green), as a function of time, are shown for a water droplet approached to 0° silica in *n*-heptane (water-saturated). Here, the exposure time of the silica substrate to *n*-heptane was 31, 23 and 17 minutes, with force curves shown in blue, cyan and green, respectively. The separation between the bottom of the water drop and the silica surface was 1500 μm at the start of the experiment ($D$ = 1600 μm), and a freshly generated water drop was used. Silica/drop contact and drop jump-in are indicated in Figure 4.13 with pink dots and yellow arrows, respectively. For all drops, an attractive force was observed as soon as the drop began moving at $t$ = 1.22 s. In all cases, the water drop progressively elongated during descent. For 31 minutes solvent exposure (blue curve in Figure 4.13), the results were described previously (section 4.3.1.3), but are shown again for ease of comparison: drop/silica contact was observed at $t$ = 13.408 s ($D$ = 403 μm, $F$ = -32.6 μN), followed by film rupture at $t$ = 13.409 s ($D$ = 403 μm, $F$ = -34.3 μN) and drop jump-in at $t$ = 13.418 s ($D$ = 402 μm, $F$ = -45.6 μN). The water drop elongated by 22.0%, with a 6.4% decrease in drop width. For 23 minutes solvent exposure (cyan curve in Figure 4.13), drop/silica contact was observed at $t$ = 12.770 s ($D$ = 466 μm, $F$ = -36.4 μN), followed by film rupture at $t$ = 12.772 s ($D$ = 466 μm, $F$ = -37.3 μN) and drop jump-in at $t$ = 12.781 s ($D$ = 465 μm, $F$ = -48.5 μN). The water drop elongated by 25.2%, with a 7.1% decrease in drop width. For 17 minutes solvent exposure (green curve in Figure 4.13), drop/silica contact was observed at $t$ = 11.731 s ($D$ = 558 μm, $F$ = -42.7 μN), followed by film rupture at $t$ = 11.732 s ($D$ = 558 μm, $F$ = -43.7 μN) and drop jump-in at $t$ = 11.741 s ($D$ = 557 μm, $F$ = -49.3 μN). The water drop elongated by 33.3%, with an 8.4% decrease in drop width. Similar to previous results, drop elongation mostly occurred in close proximity to the silica surface. In 5 ms prior to drop/silica contact, the total drop elongation was 35-40%, with 50-60% of total drop elongation observed within 50 ms of drop/silica contact for all cases shown in Figure 4.13. Interestingly, the minimum force required to observe drop deformation is in the 1.5-10 μN range and does not necessarily correlate with the

total drop deformation at drop/silica contact. Drop elongation was first visible at $t$ = 10.9 s, 3 s and 6 s for silica solvent exposure of 31 min, 23 min and 17 min, respectively.

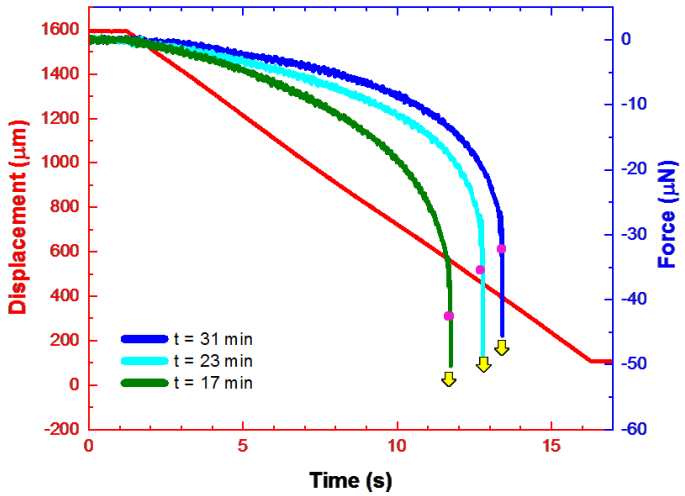


Figure 4.13 Displacement (red) and interaction force (blue, cyan, green), as a function of time, for a water droplet approached to 0° silica in *n*-heptane (water sat.). The silica exposure time in *n*-heptane prior to the experiment is indicated for each curve in the legend (bottom left). Drop/silica contact and jump-in are shown with pink dot and yellow arrow, respectively.

As seen from the results presented in Figure 4.13, decreasing the silica immersion time in *n*-heptane prior to drop/silica interaction led to: (a) larger drop elongation, (b) steeper attractive force curve during drop approach, (c) larger attractive force at drop/silica contact and (d) larger attractive force at drop jump-in. These observations are in line with results shown in Figure 4.1, which indicated the increasing contact angle of water placed on 0° silica surface as silica is exposed for larger periods of time to *n*-heptane prior to contact angle measurements. That is, a stronger hydrophilic attractive force and drop elongation were observed for a more hydrophilic silica surface (less *n*-heptane immersion time).

*4.3.1.4 Effect of KCl*

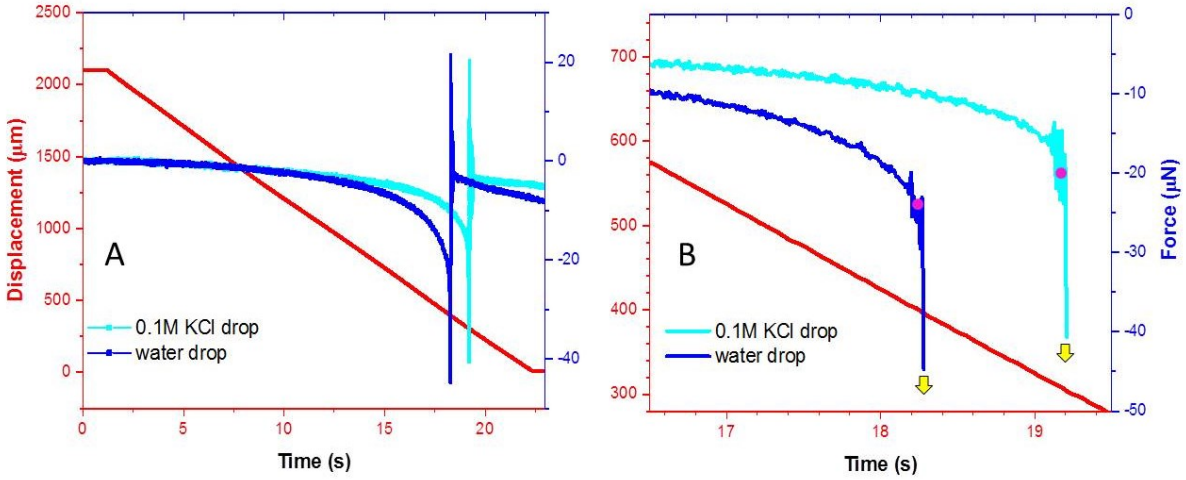


Figure 4.14 Displacement (red) and interaction force (0.1 M KCl - cyan, pure water drop - blue), as a function of time, for a droplet approached to 0° silica in *n*-heptane: (A) overall interaction, (B) region of strong drop elongation and jump-in. Drop/silica contact and jump-in are shown with pink dot and yellow arrow, respectively.

The total travel distance of the water drop was set at 2100 µm with 100 µm overlap (that is, there was an initial separation of 2000 µm between bottom of 0.1 M KCl drop and silica surface at the start of the experiment). Brand new silica discs were cleaned in piranha and used within hours in the experiment. The silica disc was exposed to *n*-heptane for 32 minutes, and a freshly generated 0.1 M KCl drop was used during the experiment. Interaction force as a function of time and displacement for both 0.1 M KCl drop and pure water drop is shown in Figure 4.14. Drop displacement is displayed in red, while the interaction force is shown in cyan and blue for 0.1 M KCl and pure water drop, respectively. As with pure water drop discussed previously (section 4.3.1.1), 0.1 M KCl drop also elongated as it approached the silica surface, with surface contact observed at $t$ = 19.191 s ($D$ = 306 µm, $F$ = -19.6 µN), followed by film rupture at $t$ = 19.192 s ($D$ = 306 µm, $F$ = -20.7 µN) and drop jump-in at $t$ = 19.201 s ($D$ = 305 µm, $F$ = -40.7 µN). Figure 4.14A shows the overall drop/silica interaction, while Figure 4.14B shows the strong droplet elongation region, with drop/silica contact and jump-in indicated by pink dots and downward arrows, respectively. The long-range interaction between 0.1 M KCl and silica was weaker than for silica with a pure water drop, as indicated by the longer interaction time required

(19.191 s vs. 18.268 s, respectively) prior to drop contact with the surface, as well as slower rate of force growth (cyan curve) as a function of displacement. Figure 4.15 shows side-camera images of 0.1 M KCl drop at the beginning of experiment (a), at drop/silica contact (b), and at drop jump-in (c). For 0.1 M KCl, the drop width decreased by 3.4% and the drop elongated by 10.8% at contact/rupture. The observed film lifetime of under 1 ms was comparable between pure water drop and 0.1 M KCl drop. All other conditions equal, 0.1 M KCl had a retarding effect on droplet elongation, with about half the change in drop height observed (10.8%), compared to the pure water drop (20.3%); the difference is clearly visible when compared with the pure water drop side-camera images (see Figure 4.7).

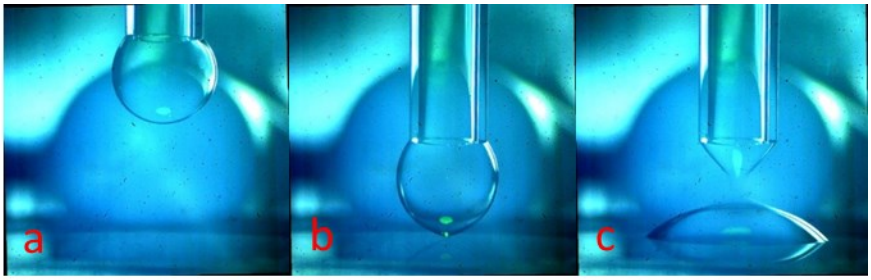


Figure 4.15 Side-camera images of 0.1 M KCl drop interaction with 0° silica in *n*-heptane: (a) undeformed drop ($t$ = 0 s), (b) drop/silica contact ($t$ = 19.191 s), (c) drop jump-in ($t$ = 19.201 s).

The effect of salt addition on the interaction force between the water drop and the silica surface in water-saturated *n*-heptane is shown in Figure 4.16: (A) displacement (red) and interaction force (blue – pure water, cyan – 0.1 M KCl), as a function of time; (B) pertinent side-camera images of drop profiles. The exposure time of silica substrate to *n*-heptane was the same in both cases (23 and 22 minutes for pure water drop and 0.1 M KCl drop, respectively), but less than in the previously discussed pure *n*-heptane (Figure 4.14, 32 minutes). Separation between the bottom of the water drop and the silica surface was 1500 μm at start of experiment ($D$ = 1600 μm), and a freshly generated water drop was used. The water drop before approach, at silica/drop contact and at drop jump-in is indicated in Figure 4.16 with orange dot, pink dot and yellow arrow, respectively.

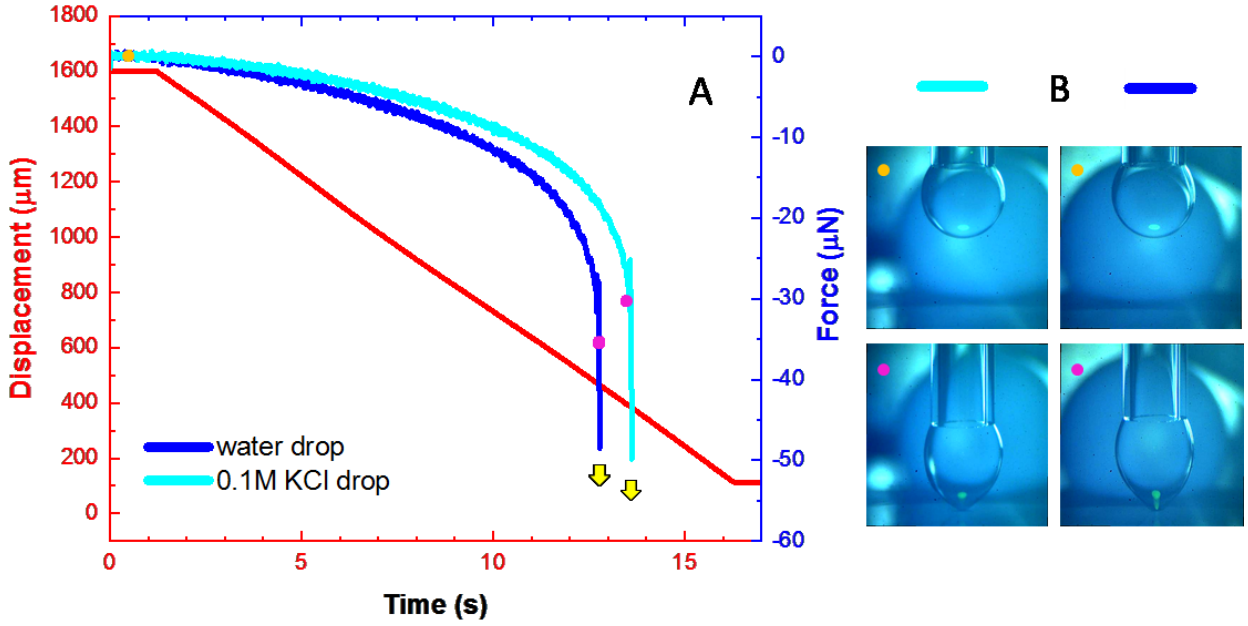


Figure 4.16 (A) Displacement (red) and interaction force (0.1M KCl drop - cyan, water drop - blue), as a function of time, for a droplet approached to 0° silica in *n*-heptane (water-sat.), (B) side-camera drop images before approach and at drop/silica contact. Drop before approach, drop/silica contact and drop jump-in are indicated with orange dot, pink dot and yellow arrow, respectively.

For both drops, an attractive force was observed as soon as the drop began moving at $t$ = 1.22 s and the drops progressively elongated during descent. For pure water drop (blue curve in Figure 4.16), results have been discussed previously in section 4.3.1.3 (see Figure 4.13, cyan curve), but are repeated here for ease of comparison with 0.1 M KCl drop. For pure water drop, drop/silica contact was observed at $t$ = 12.770 s ($D$ = 466 μm, $F$ = -36.4 μN), followed by film rupture at $t$ = 12.772 s ($D$ = 466 μm, $F$ = -37.3 μN) and drop jump-in at $t$ = 12.781 s ($D$ = 465 μm, $F$ = -48.5 μN). The water drop elongated by 25.2% (369 μm), with a 7.1% decrease in drop width. For 0.1 M KCl drop (cyan curve in Figure 4.16), drop/silica contact was observed at $t$ = 13.607 s ($D$ = 384 μm, $F$ = -30.2 μN), followed by film rupture at $t$ = 13.608 s ($D$ = 384 μm, $F$ = -31.4 μN) and drop jump-in at $t$ = 13.617 s ($D$ = 383 μm, $F$ = -49.8 μN). The 0.1 M KCl water drop had elongated by 18.5% (270 μm), with a 4.6% decrease in drop width. Similar to pure

water drop discussed previously, 0.1 M KCl drop elongation occurred predominantly within a short time before silica/drop contact: 42% total elongation and 60% total elongation within 5 ms and 50 ms, respectively. The observed film lifetime of (under 1 ms from the bottom camera) was comparable between pure water drop and 0.1 M KCl drop.

The larger drop elongation for the water drop (25.2%) than for 0.1 M KCl (18.5%) is clearly visible in the side-camera images (Figure 4.16B). Similar to pure *n*-heptane discussed previously, in water-saturated *n*-heptane, 0.1 M KCl had a retarding effect on the drop elongation, as well as reduction in attractive force at drop/silica contact and during jump-in. However, the effect of salt for water-saturated *n*-heptane is less pronounced than for pure *n*-heptane: drop elongation was reduced by about only a quarter for the former, while it was about half for the latter (20.3% vs. 10.8% drop elongation for water and 0.1 M KCl, respectively, in pure *n*-heptane). Reduced exposure time of silica to *n*-heptane prior to the experiment (23 minutes vs. 32 minutes) and the presence of trace water in *n*-heptane (saturated vs. none) increased the elongation of both pure water drop (25.2% vs. 20.3%) and 0.1 M KCl drop (18.5% vs. 10.8%), with the salty water drop affected more strongly.

*4.3.1.5 Effect of pH*

To study the effect of pH on the interaction between a water droplet and silica in *n*-heptane, the pure water droplet was replaced with NaOH solution at two different pH strengths. The effect of pH is first presented as a function of silica/*n*-heptane exposure time and pH level. Next, a comparison between the strength of the interaction force and droplet deformation is discussed for relevant pure water drop studies.

The effect of pH and silica exposure time in *n*-heptane prior to droplet/silica interaction is shown in Figure 4.17. The total travel distance of the alkaline water drop was 2100 μm with 100 μm overlap (that is, there was a separation of 2000 μm between bottom of the drop and the silica surface at the start of experiment). A droplet of NaOH (freshly generated) was approached to silica substrates in water-saturated *n*-heptane. In Figure 4.17, displacement (red) and interaction force (blue, cyan, green) are shown, as a function of time, for a NaOH droplet approached to 0° silica in *n*-heptane (water sat.). Specifically, pH 9.7 drop with silica solvent exposure time of 78

and 31 minutes is shown in blue and cyan, respectively, and pH 12.2 with silica solvent exposure time of 20 minutes is shown in green.

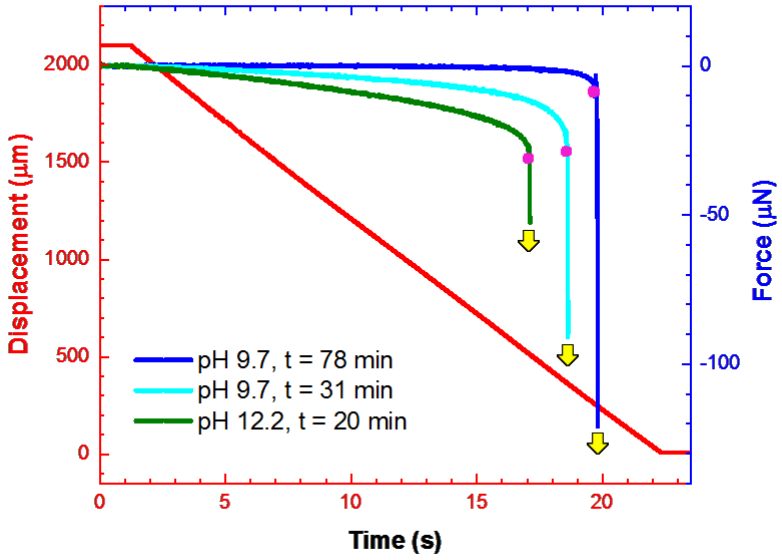


Figure 4.17 Displacement (red) and interaction force (blue, cyan, green), as a function of time, between a NaOH droplet and to 0° silica in *n*-heptane (water sat.). The pH and silica exposure time in *n*-heptane prior to the experiment are indicated for each curve in the legend (bottom left). Drop/silica contact and jump-in are shown with pink dot and yellow arrow, respectively.

In the case of 78 minutes of solvent exposure with pH = 9.7 droplet (blue curve in Figure 4.17), attractive force began at $t$ = 13 s ($D$ = 918 μm), while droplet deformation became visible at $t$ = 18.5 s. The droplet progressively deformed until the bottom of droplet funneled toward the silica surface. From side-camera images, the droplet contacted the silica surface at $t$ = 19.776 s ($D$ = 249 μm, $F$ = -9.7 μN), with film rupture observed at 19.777 s ($D$ = 249 μm, $F$ = -9.8 μN), as shown with a pink dot in Figure 4.17. No Newton fringes were visible from the bottom camera, with rupture observed at $t$ = 19.7764, for an estimated film lifetime of 0.4 ms. The drop jump-in occurred at 19.817 s ($D$ = 245 μm, $F$ = -68.1 μN), as indicated by a yellow arrow; shortly after the peak attractive force of $F$ = -120.8 μN at $t$ = 19.8039 s. From side-camera image analysis, the

drop elongated by 144 μm (9.7%) in height between $t = 0$ and $t = 19.777$ s, very close to 149 μm from displacement curve; the drop decreased in width by 2.1%.

For 31 minutes of solvent exposure with pH = 9.7 droplet (cyan curve in Figure 4.17), attractive force was observed immediately (at $t = 1.22$ s) as the droplet began its descent towards the silica substrate. The droplet progressively deformed into an elongated shape during descent, with droplet/silica contact (pink dot in Figure 4.17) observed at $t = 18.602$ s ($D = 360$ μm, $F = -30.3$ μN), and with film rupture at $t = 18.604$ s ($D = 359$ μm, $F = -30.4$ μN). No Newton fringes were visible on the bottom camera, with film rupture observed at $t = 18.6033$ s and an estimated film lifetime of ~1.5 ms. After rupture, the attractive force began increasing rapidly, with a maximum at 18.628 s ($D = 357$ μm, $F = -90.9$ μN,) shortly before droplet detachment (jump-in) at $t = 18.635$ s ($D = 356$ μm, $F = -81.7$ μN). From side-camera images, the drop elongated by 273 μm (18.3%) in height between $t = 0$ and $t = 18.6033$ s, close to 260 μm from the displacement curve. The drop decreased in width by 6.0%. This indicates that a reduced solvent exposure time (78 vs. 32 minutes) leads to stronger elongation and stronger attractive force between the water droplet and the silica substrate.

Finally, for 20 minutes of solvent exposure with pH = 12.2 droplet (green curve in Figure 4.17), attractive force was observed immediately as the droplet began its descent towards the silica substrate (at $t = 1.22$ s). The droplet progressively deformed into an elongated shape during descent, until the bottom of the droplet funneled to the surface, with silica/droplet contact (pink dot in Figure 4.17) observed at $t = 17.100$ s ($D = 503$ μm, $F = -31.2$ μN), and film rupture occurring at $t = 17.101$ s ($D = 503$ μm, $F = -31.7$ μN). No Newton fringes were visible on the bottom camera, with film rupture observed at 17.1006 and an estimated film lifetime of 0.6 ms. Droplet jump-in was observed at $t = 17.126$ s ($D = 500$ μm, $F = -51.5$ μN). From side-camera images, the drop decreased in width by 8.4% and had elongated by 410 μm (28.1%), the largest drop elongation of the three curves shown in Figure 4.17. This value is close to the expected amount of 403 μm from the displacement curve. From Figure 4.17 and the results discussed above, for high-pH drop interactions with silica substrate, less silica exposure time to *n*-heptane prior to drop/silica interaction leads to: (a) an attractive force with bigger range (detected by the bimorph at larger drop/silica separation), (b) larger drop elongation on contact, (c) larger

attractive force on contact and (d) shorter drop jump-in time. The drop jump-in time had decreased significantly from 41 ms to 33 ms to 26 ms from blue, to cyan, to green curve, respectively, in Figure 4.17. The strong drop elongation observed at pH 12.2 compared with pH 9.7 could be related to both an increase in pH of the drop and shorter silica exposure time to *n*-heptane. More work is required to determine which effect is dominant.

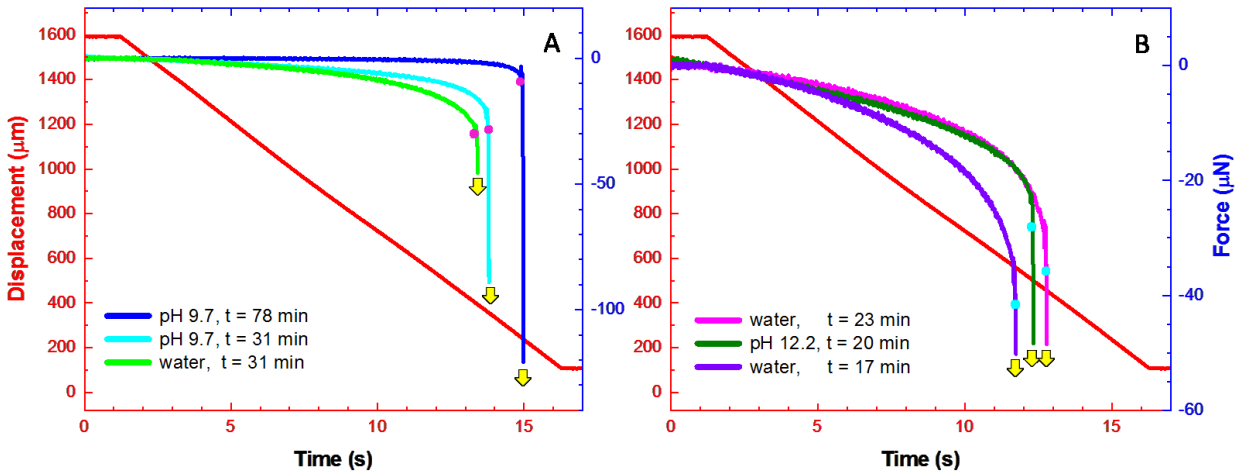


Figure 4.18 Displacement (red) and interaction force (blue, cyan, neon, pink, green, purple), as a function of time, between a drop (A – pH 9.7 vs. water, B – pH 12.2 vs. water) and 0° silica in *n*-heptane (water sat.). The drop pH and silica exposure time in *n*-heptane prior to the experiment are indicated for each curve in the legend. Drop/silica contact and jump-in are shown with dot (A – pink, B – cyan) and yellow arrow, respectively.

A comparison of various drops (pure water, alkaline pH) and 0° silica interactions in water-saturated *n*-heptane is presented in Figure 4.18. Displacement (red) and interaction force (blue, cyan, neon, pink, green and purple) are shown, as a function of time, with initial separation at $D = 1600$ (1500 μm between the bottom of the drop and the silica surface). Comparison between pH 9.7 and water is shown in Figure 4.18A, while between pH 12.2 and water is shown in Figure 4.18B. For ease of visualization, the alkaline pH interaction curves have the same colour schematic as in Figure 4.17, while pure water drop interactions are shown in neon, purple and pink. The drop pH and *n*-heptane exposure time of silica prior to experiment are indicated for

each curve in the legend, with drop/silica contact and jump-in shown with a dot (Figure 4.18A – pink, Figure 4.18B – cyan) and yellow arrow, respectively. Results of alkaline pH drop/silica interactions were adjusted from 2100 μm to 1600 μm (an example is shown in Figure 4.11) in order to compare with previous water drop results; both discussed in detail previously in section 4.3.1.3. From Figure 4.18A, at the same *n*-heptane exposure time to silica (31 min), the drop/silica interaction was stronger (-32.6 μN vs. -28.4 μN), faster (contact time: 13.408 s vs. 13.779 s), and with a larger drop elongation (22.0% vs. 18.3%) for pure water than for pH 9.7, as seen for neon and cyan curves, respectively. In Figure 4.18B, pH 12.2 drop interaction with silica exposed to *n*-heptane for 20 min (green curve) is compared to water drop interaction with silica exposed to *n*-heptane for 23 min (pink curve) and for 17 min (purple curve). The pH 12.2 curve follows the trajectory of water at $t$ = 23 min closely, but drop/silica contact appears sooner (12.314 s vs. 12.770 s), at a weaker attractive force (-27.0 μN vs. -36.4 μN) and at a larger drop elongation on contact (28.1% vs. 25.2%). When compared with pure water drop at 17 min *n*-heptane silica exposure, pH 12.2 drop has weaker interaction force (-27.0 μN vs. -42.7 μN), longer time to surface contact (12.314 s vs. 11.731 s) and smaller drop elongation (28.1% vs. 33.3%). Since the *n*-heptane exposure time of pH 12.2 drop (20 min) was intermediate to that of water drop (23 min and 17 min), it is not straightforward which element has dominance for the observed intermediate drop elongation: the alkaline nature of the 12.2 pH drop or the silica *n*-heptane exposure time. However, the lower attractive force on contact for pH 12.2 drop than either of the water drops indicates that a pure water drop has a stronger attractive interaction with 0° silica than an alkaline drop, in line with earlier observations at pH 9.7 in Figure 4.18A. In all cases, a larger attractive force at jump-in was observed for alkaline drops than for pure water drops, which is related to the longer jump-in time for alkaline drops than for water drops (26-41 ms vs. 10-11 ms).

*4.3.1.6 Effect of approach velocity*

The effect of approach velocity is compared by conducting experiments at $V$ = 0.5 mm/s and $V$ = 0.1 mm/s. Results for $V$ = 0.5 mm/s are presented first, followed by comparison with previously discussed results at $V$ = 0.1 mm/s. The former was conducted using the new displacement sensor (optoNCDT 1320) that allowed for a larger experimental range of 5 mm.

For $V$ = 0.5 mm/s approach velocity, the total travel distance of the water drop was 5000 µm with 100 µm overlap (that is, there was 4900 µm between the bottom of water drop and the silica surface at the start of the experiment). The silica disc (freshly cleaned in piranha) was exposed to *n*-heptane (water sat.) for 21 minutes prior to drop approach, and a freshly generated water drop was used during the experiment. Interaction force (blue) as a function of time and displacement (red) for this system is shown in Figure 4.19, along with several side-camera drop images to the right, corresponding to $t$ = 5 s (pink, original drop size), $t$ = 10.439 s (green, drop/silica contact) and $t$ = 10.449 s (yellow arrow, drop jump-in).

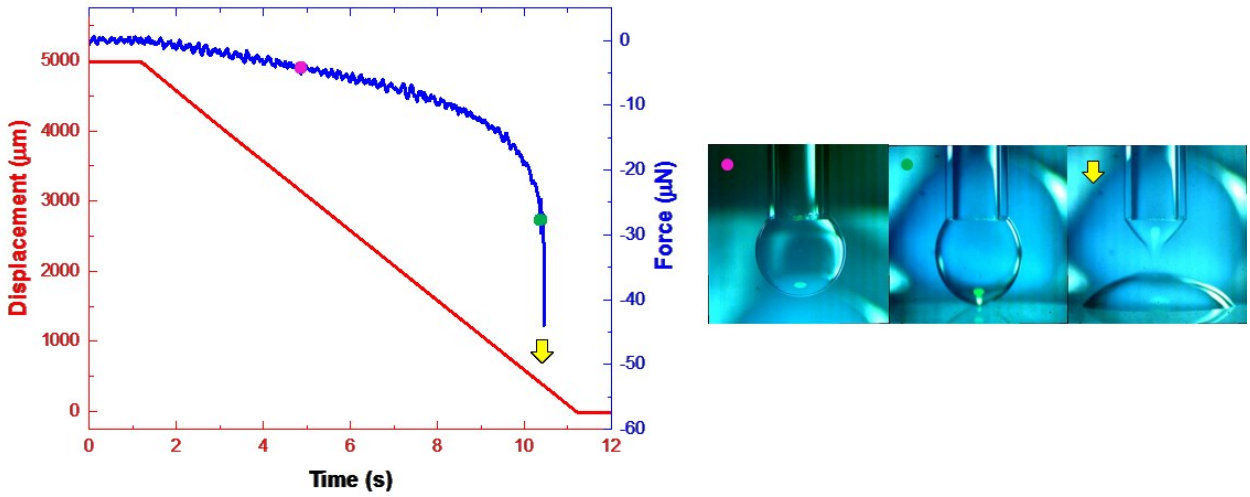


Figure 4.19 Displacement (red) and interaction force (blue) for a water droplet approaching a 0° silica substrate in *n*-heptane (water sat.) with corresponding side camera images (indicated with matching symbols on force curve): $t$ = 5 s (pink); $t$ = 10.439 s (green); $t$ = 10.449 (yellow arrow).

Attractive interaction force was observed the moment the drop started moving (~1.22 s), increasing in a linear fashion (slope = -1.33) until ~7 s ($D$ = 2081 µm, $F$ = -7.4 µN). However, the water drop elongation toward the silica substrate was not visually detected until $t$ = 9.5 s ($D$ = 840 µm, $F$ = -15.5 µN). At contact/rupture ($t$ = 10.439 s, $F$ = -27.7 µN), the water drop had elongated by 9.7%. After film rupture ($t$ = 10.440 s), drop jump-in was observed at $t$ = 10.449 s ($F$ = -43.9 µN). The effect of approach velocity on the observed interaction force between the water drop and silica in *n*-heptane (water sat.) is shown in Figure 4.20. Displacement (red,

orange) and force (blue, cyan) are shown for $V$ = 0.5 mm/s and $V$ = 0.1 mm/s, respectively. Drop/surface contact and jump-in are indicated by a green dot and downward arrows, respectively. Figure 4.20A shows displacement and force curves as a function of time, while Figure 4.20B compares the force curves for $V$ = 0.5 mm/s and $V$ = 0.1 mm/s as a function of displacement.

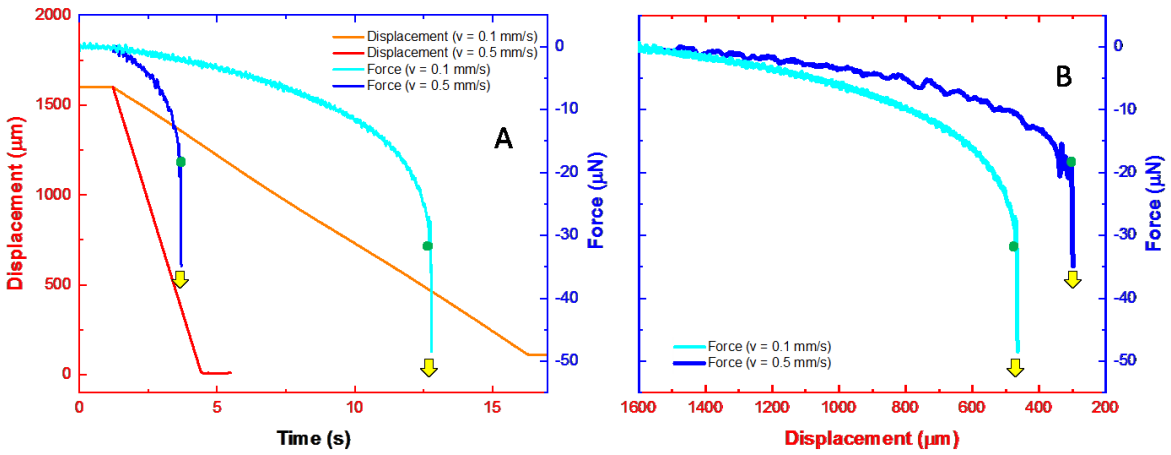


Figure 4.20 Effect of velocity on the interaction between water droplet and 0° silica in *n*-heptane (water sat.): Displacement (red, orange) and force (blue, cyan) are shown for $V$ = 0.5 mm/s and $V$ = 0.1 mm/s, respectively. Drop/surface contact and jump-in are indicated by a green dot and downward arrows, respectively. A – Displacement and force as a function of time, B – Force as a function of displacement.

For effective comparison, the interaction for $V$ = 0.5 mm/s from Figure 4.19 was scaled to show the force starting from $D$ = 1600 µm, to match available data from $V$ = 0.1 mm/s done prior to purchase of the large-range displacement sensor. That is, only force data from displacement of 1600 µm and closer is shown and the curve was moved upward to start at $F$ = 0, as would be expected to be observed had the experiment been conducted only in this displacement range. The exposure time of silica substrates was slightly different, at 23 and 21 minutes for $V$ = 0.1 mm/s and $V$ = 0.5 mm/s, respectively. Results from $V$ = 0.1 mm/s have been discussed previously in section 4.3.1.3 (see Figure 4.13). For $V$ = 0.1 mm/s, the drop elongated 25.2%, while for $V$ = 0.5 mm/s it elongated only 9.7%. The observed interaction force at drop/silica contact was -36.4 µN

and -18.5 μN for $V$ = 0.1 mm/s and $V$ = 0.5 mm/s, respectively. The increase in force between drop contact and drop jump-in is similar in both cases (12.1 μN vs. 16.2 μN for 0.1 mm/s and 0.5 mm/s approach velocities, respectively), which is reasonable given the same drop size and time between drop contact and jump-in (10 ms). Slower approach velocity led to a larger drop elongation (drop/silica contact at larger displacement) and stronger interaction force at drop/silica contact, which is clearly visible from Figure 4.20B. Such observation is expected, as the majority of the drop elongation occurred in close proximity to the silica substrate, and at higher approach velocities, the drop spent less time in this drop/silica interaction zone. The exact relationship is less clear; at 0.1 mm/s, the drop elongation was 2.6 times larger, but the observed force was only 1.76 times stronger, while the difference in velocity was five-fold (0.1 mm/s versus 0.5 mm/s).

*4.3.1.7 Effect of surface roughness*

How the presence of surface roughness on silica substrate affects the water/silica interaction is explored in this section. For $V$ = 0.5 mm/s approach velocity and total vertical drop displacement of 5000 μm (including 100 μm overlap), a surface-roughened silica disc (freshly cleaned in piranha) was exposed to *n*-heptane (water sat.) for 20 minutes prior to water drop approach (freshly generated). Interaction force (blue) as a function of time and displacement (red) for this system is shown in Figure 4.21, with several side-camera images of the water drop shown in Figure 4.22. Attractive interactive force was observed the moment the drop started moving (~1.22 s), increasing in a linear fashion (slope = -3.01) until ~7 s; the undeformed water drop is shown in Figure 4.22a. However, the water drop elongation toward the silica substrate was not visually detected until $t$ = 9.0 s ($D$ = 1108 μm, $F$ = -26.9 μN). Drop/silica contact occurred at $t$ = 10.542 s ($D$ = 343 μm, $F$ = -54.0 μN), shown in Figure 4.22b and indicated with a green dot in Figure 4.21. The water drop had elongated by 16.7%, with a 4.5% reduction in width. Due to surface roughness, drop/silica contact was not visible from the bottom camera. The drop/silica contact area increased slightly over several milliseconds (Figure 4.22c), followed by film rupture at $t$ = 10.547 s ($D$ = 342 μm, $F$ = -56.1 μN) shown in Figure 4.22d. Unlike interactions between water drop and smooth silica, no jump-in was observed for roughened silica; the water drop continued to slowly spread on the silica surface after film rupture (Figure 4.22e). On capillary retraction, the water drop remained on the silica surface and detached from the capillary at $t$ =

15.492 s ($D$ = 666 µm, $F$ = -108.1 µN), also indicated with a cyan dot in Figure 4.21. Experiments with roughened silica proved difficult to reproduce and more work should be done to understand the underlying cause.

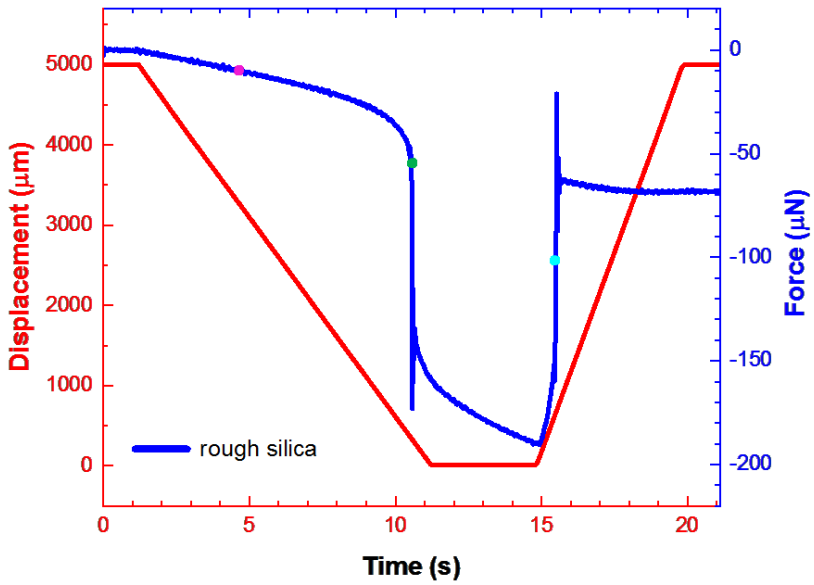


Figure 4.21 Displacement (red) and interaction force (blue) for a water droplet approached to a 0° roughened silica substrate in *n*-heptane (water sat.). The force curve indicates the undeformed drop (pink dot, $t$ = 6 s), drop/silica contact (green dot, $t$ = 10.542 s) and drop detachment on retraction (cyan dot, $t$ = 15.492 s).

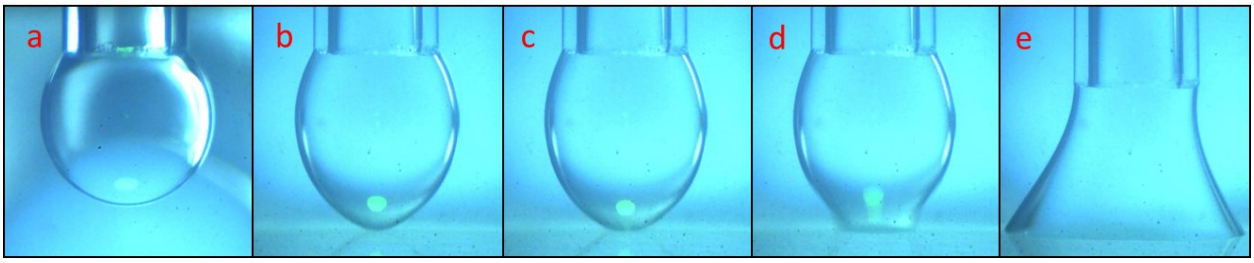


Figure 4.22 Side-camera images of water interaction with 0° roughened silica in *n*-heptane (water sat.): (a) undeformed drop (6 s), (b-c) drop/silica contact (10.542 s, 10.546 s), (d) film rupture (10.547 s), (e) drop attached to capillary (12 s).

*4.3.1.8 Effect of wettability*

A water droplet was driven toward a silica substrate in *n*-heptane with contact angle of 107° (water drop in air) at three different velocities: $V$ = 1 mm/s, $V$ = 0.1 mm/s and $V$ = 0.01 mm/s. Unlike the cases described previously, there was no long-range interaction force observed for hydrophobic silica in *n*-heptane. For 1 and 0.1 mm/s, the total travel distance was 600 μm, with bottom 100 μm as overlap (distance between water droplet and silica surface was 500 μm). For 0.01 mm/s, due to memory space constraints, the approach distance was limited to 300 μm, of which 100 μm was the overlap and the retraction portion could not be saved. The retraction speed for all cases was 1 mm/s. Figure 4.23 shows the displacement and force curves at (A) $V$ = 1 mm/s, (B) $V$ = 0.1 mm/s and (C) $V$ = 0.01 mm/s approach velocities, where "1" indicates droplet approach and "2" indicates droplet retraction. The spatiotemporal thin film drainage profiles (calculated from interference fringes, as shown in Figure 3.8) and corresponding SRYL modeling are shown in Figure 4.24.

For $V$ = 1 mm/s (Figure 4.23A1-A2), drop/silica contact occurred at $t$ = 1.721 s, with the first Newton ring visible from the bottom camera at $t$ = 1.744 s. Once the full 100 μm overlap ($D$ = 0) was reached at $t$ = 1.934 s, the measured repulsive force was $F$ = 16.3 μN. The capillary retraction began at $t$ = 37.08 s, and the repulsive force began decreasing rapidly until a strong attractive force of $F$ = -42.1 μN was present even as the droplet stopped moving at $t$ = 37.84 s. The attractive force reached a maximum at $F$ = -45.8 μN when $t$ = 38.25 s, at which point the droplet detached from the silica substrate and the force returned to zero. A small water droplet

remained on the silica surface. For $V$ = 0.1 mm/s (Figure 4.23B1-B2), drop/silica contact occurred at $t$ = 6.187 s, with the first Newton ring visible at $t$ = 6.248 s. After 100 μm overlap was reached at $t$ = 7.187 s, the measured repulsive force was 14.8 μN. Once retraction began at $t$ = 37.35 s, repulsion decreased rapidly until a strong attractive force of $F$ = -40.4 μN at $t$ = 37.90 s was observed, after which the droplet detached from the silica surface at $t$ = 37.952 s and the force returned to zero. The capillary returned to its original position of $D$ = 600 μm at $t$ = 38.13 s. A small water droplet remained on the silica surface. Finally, for $V$ = 0.01 mm/s (Figure 4.23C1), the water droplet began moving at $t$ = 1.24 s and drop/silica contact ($D$ = 100 μm) was reached at $t$ = 24.495 s. Once the full 100 μm overlap ($D$ = 0) was reached at $t$ = 36.237 s, the repulsive force was measured at $F$ = 12.8 μN. No water drop remained on the silica surface after the capillary returned to its original position.

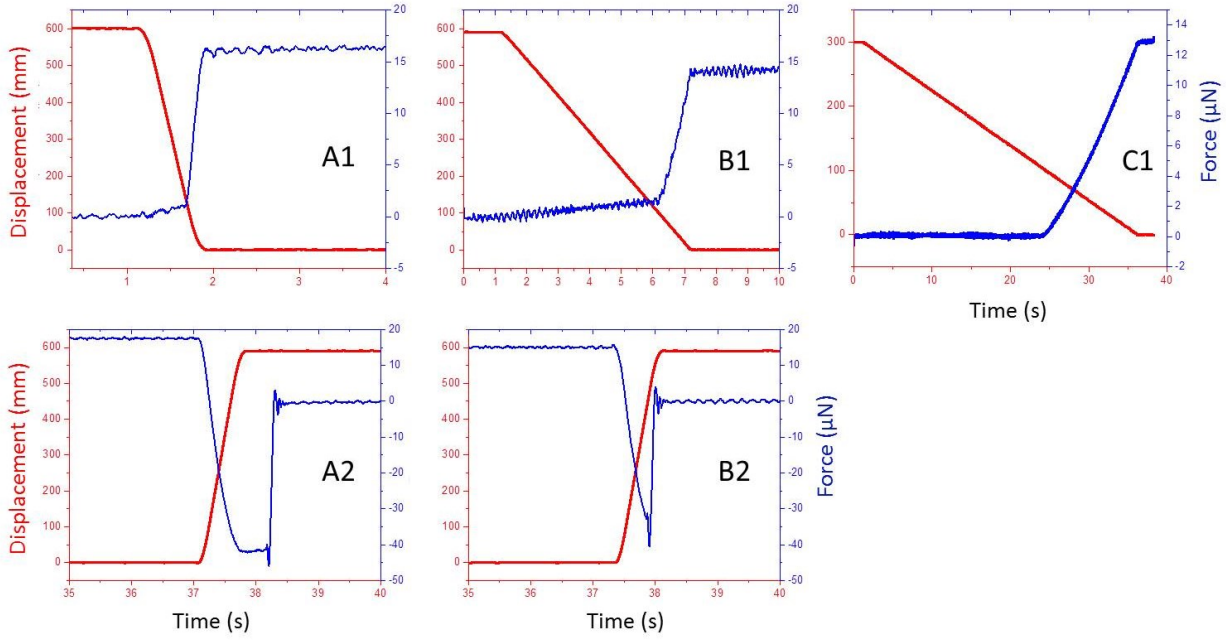


Figure 4.23 Displacement (red) and interaction force (blue) curves, as a function of time, for a water droplet and 107° silica in *n*-heptane at (A) 1 mm/s, (B) 0.1 mm/s and (C) 0.01 mm/s approach velocities; 1 indicates droplet approach and 2 indicates droplet retraction.

The input variables used for the SRYL modeling of these experimental results are shown in Table 4.1, with the spatiotemporal thin film profiles shown in Figure 4.24 for approach velocity of (A) 1 mm/s and (B) 0.1 mm/s.

Table 4.1 Input parameters for the SRYL theoretical model

| Parameter ($T$ = 22°C) | Value |
|---|---|
| *n*-Heptane viscosity, $\mu$ | 0.402 mPa·s |
| Water viscosity, $\mu$ | 1.002 mPa·s |
| Droplet radius, $R$ | 0.85 mm |
| *n*-Heptane/water interfacial tension, $\gamma$ | 51.0 mN/m |

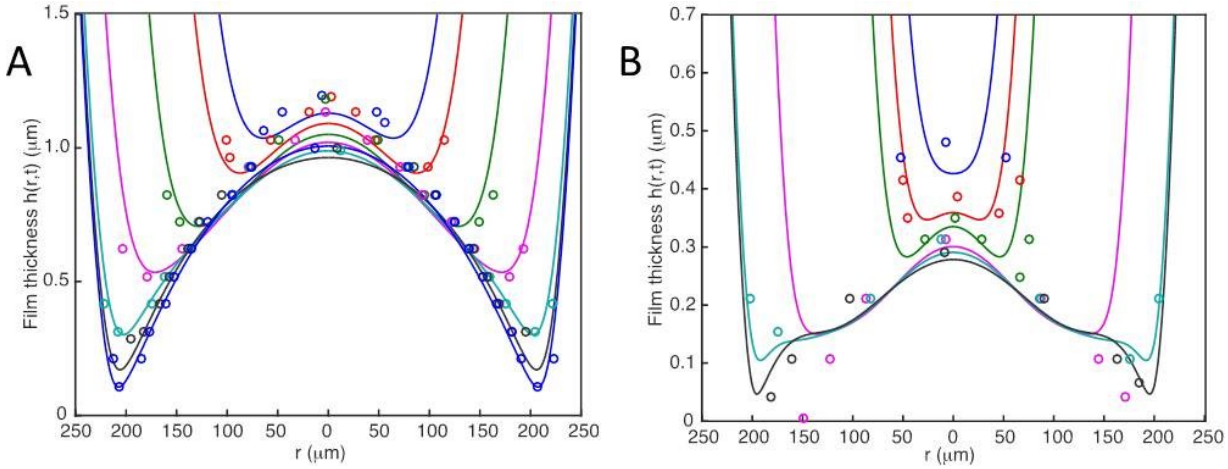


Figure 4.24 Spatiotemporal thin film drainage profiles for water droplet approached to 107° silica in *n*-heptane at velocities of (A) 1 mm/s and (B) 0.1 mm/s. Experimental data (open circles) shown with corresponding SRYL model (solid line). Time progresses downward in each image as follows: (A) 1.744, 1.760, 1.800, 1.860, 1.976, 2.260, 2.996 s; (B) 6.248, 6.296, 6.368, 7.028, 7.580, 8.808 s.

The theoretical curves agreed with the experimental data quite well, with better matching observed for 1 mm/s versus 0.1 mm/s. At both velocities, the Newton rings became asymmetrical during the film drainage process, and it was no longer possible to extract the film profile

information after that point. For all three velocities, the asymmetric Newton ring film drainage was related to film rupture, as evidenced by an adhesion force and water droplet deformation observed during retraction of the capillary. The strongest adhesion force (45.8 μN) was observed at $V$ = 1 mm/s, where the droplet detached from the surface after capillary finished retracting to its original position (Figure 4.23A2). A slightly weaker adhesion force (40.4 μN) was observed at $V$ = 0.1 mm/s.

### *4.3.2 Water/sapphire*

For sapphire, as shown in Figure 4.1 and Figure 4.2, even 15 minutes of solvent exposure resulted in water contact angle of 24° (toluene) and 58° (*n*-heptane). Without a hydrophilic coating, it does not seem to be practically feasible to conduct measurements with a truly hydrophilic sapphire surface. For this reason, no interactions between ~0° sapphire and water droplet are presented here. Instead, the results discussed below will focus on interactions with a 60° sapphire surface.

A water droplet was approached to a sapphire substrate with contact angle of 60° (water drop in air) at three different velocities: $V$ = 1 mm/s, $V$ = 0.1 mm/s and $V$ = 0.01 mm/s. No long-range interaction force was observed. For $V$ = 1 mm/s and $V$ = 0.1 mm/s, the total travel distance was 600 μm, with the bottom 100 μm as overlap (distance between water droplet and silica surface was 500 μm at the start of the experiment). For $V$ = 0.01 mm/s, due to memory space constraints, the approach displacement was limited to 300 μm, of which 100 μm was the overlap. For $V$ = 1 mm/s and $V$ = 0.1 mm/s approach velocities, the retraction distance was larger (~1500 μm) to capture the droplet adhesion force, followed by droplet detachment. The retraction speed for all cases was 1 mm/s. Figure 4.25 shows the displacement and force curves for (A) $V$ = 1 mm/s, (B) $V$ = 0.1 mm/s and (C) $V$ = 0.01 mm/s approach velocities. In addition to force and displacement curves, spatiotemporal thin film drainage profiles for $V$ = 1 mm/s and $V$ = 0.1 mm/s are shown in A and B of Figure 4.26, respectively. Experimental data points for spatiotemporal thin film drainage profiles are shown with open circles, with corresponding SRYL modeling shown with solid lines. Relevant input parameters for the SRYL model are shown in Table 4.1.

For all approach velocities, film rupture was observed, with film lifetime decreasing with decreasing approach velocity: 0.476 s, 0.382 s and 0.208 s film lifetimes were observed for $V$ = 1 mm/s, $V$ = 0.1 mm/s and $V$ = 0.01 mm/s, respectively. As observed in previous studies,[12,71] a higher approach velocity leads to a larger observed dimple, and can be seen when comparing $V$ = 1 mm/s (Figure 4.26A) and $V$ = 0.1 mm/s (Figure 4.26B).

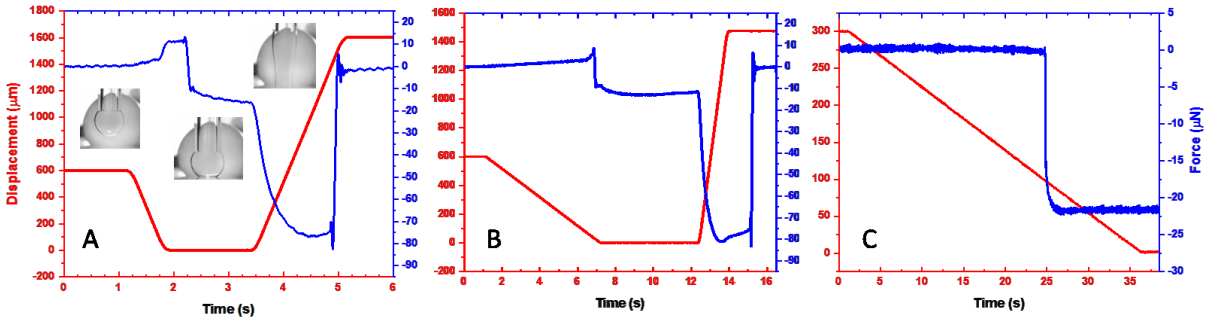


Figure 4.25 Displacement (red) and interaction force (blue), as a function of time, between water droplet and 60° sapphire in *n*-heptane at (A) 1 mm/s, (B) 0.1 mm/s and (C) 0.01 mm/s approach velocities.

For $V$ = 1 mm/s, the drop reached the sapphire surface at $t$ = 1.729 s ($D$ = 100 μm), with the first Newton ring visible at 1.768 s. Full overlap was reached at $t$ = 1.941 s ($D$ = 0 μm, $F$ = 11.3 μN), with film rupture observed at $t$ = 2.244 s. The capillary began retracting from the surface at $t$ = 3.41 s, with the drop continuously elongating (bottom of drop attached to the sapphire surface and moving upward with the capillary) for a maximum adhesive force of 82.5 μN at $t$ = 4.90 ($D$ = 1412 μm), and drop detachment at $t$ = 5.00 s, $D$ = 1515 μm (part of the droplet remained on the sapphire surface). The agreement between experimental data (open circles) and SRYL model (lines) for spatiotemporal film profiles at $V$ = 1 mm/s was good, as shown in Figure 4.26A.

For $V$ = 0.1 mm/s, the first Newton ring became visible at $t$ = 6.512 s ($F$ = 3.48 μN). Maximum repulsive force of 8.75 μN was reached at $t$ = 6.849 s ($D$ = 34 μm), with film rupture occurring at $t$ = 6.884 ($D$ = 31 μm, $F$ = 4.14 μN). The corresponding film profiles and SRYL model of the data are shown in Figure 4.26B; SRYL model showed better fit with experimental data for 1 mm/s (Figure 4.26A) than for 0.1 mm/s. There was a slight bimorph signal drift upward during

approach, where the measured force was 8.25 μN, corresponding to an actual interaction force of 4.3 μN with subtraction of the initial bimorph drift ~4 μN. The strong adhesion force upon droplet withdrawal for both 1 mm/s and 0.1 mm/s was comparable at 77-83 μN, as shown in Figure 4.25(A,B). The observed adhesive force between a water droplet and 60° sapphire in *n*-heptane is about double that of a water droplet and 107° silica in *n*-heptane (section 4.3.1.8): 77-83 μN vs. 40-45 μN. This is a reasonable observation given a stronger affinity of the water droplet to a surface of a higher level of hydrophilicity (60° vs. 107°).

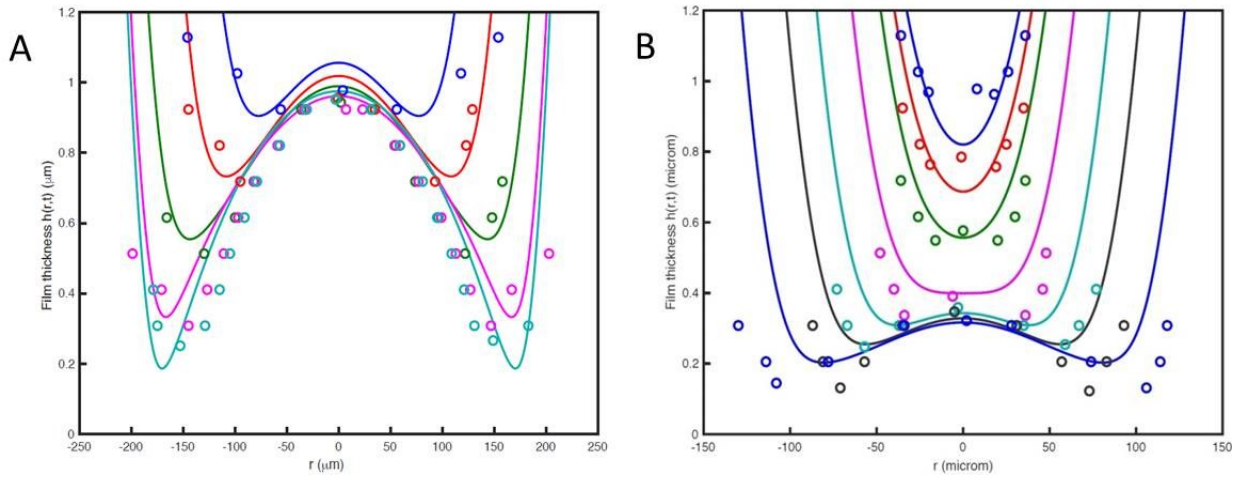


Figure 4.26 Spatiotemporal thin film drainage profiles for a water droplet approached to 60° sapphire in *n*-heptane at velocities of (A) 1 mm/s and (B) 0.1 mm/s. Experimental data (open circles) with corresponding SRYL model (solid lines). Time progresses downward in each image as follows: (A) 1.798, 1.828, 1.878, 1.970, 2.242 s; (B) 6.512, 6.520, 6.532, 6.570, 6.644, 6.728, 6.882 s.

For $V$ = 0.01 mm/s, the first Newton ring was visible at 24.588 s ($D$ = 100.2), and the drop reached the sapphire surface at $t$ = 24.597 s ($D$ = 100 μm). The film quickly ruptured thereafter, as observed from the bottom camera at $t$ = 24.796 s ($D$ = 98.5 μm), resulting in an attractive force of -22 μN (Figure 4.25C) due to formation of 3-phase contact line and drop spreading on the sapphire surface. In this case, the agreement between the SRYL model and experimental film profile curves was poor, the reason for this discrepancy is not clear.

Summary of film lifetime and comparison between thin film thickness at the center and rim of the film for all three approach velocities (1, 0.1 and 0.01 mm/s) is shown in Figure 4.27.

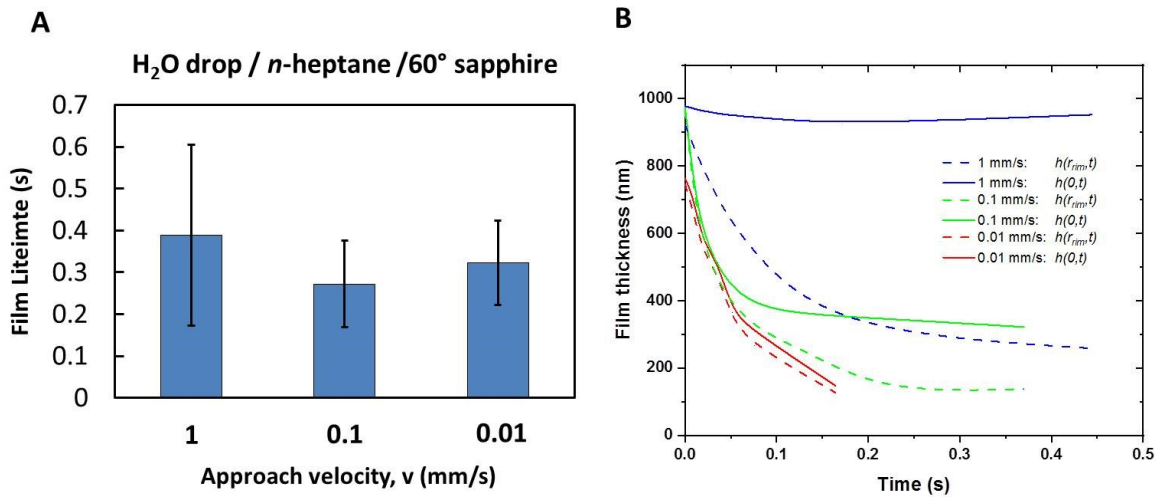


Figure 4.27 Characterization of thin film profiles between water droplet and 60° sapphire in *n*-heptane: (A) film lifetime comparison at each velocity, (B) film thickness as a function of time at the center [$h(0,t)$, solid line] and rim [$h(r_{rim},t)$, dotted line] of the thin film at $V$ = 1 mm/s (blue), $V$ = 0.1 mm/s (green), and $V$ = 0.01 mm/s (red).

In Figure 4.27A, the film lifetime (first observed Newton ring until film rupture) is shown for 3-4 experiments at each condition. The error bars represent $\pm 1s$ (standard deviation). The film lifetime variation between experiments was fairly significant, especially at the higher approach velocity of $V$ = 1 mm/s. In Figure 4.27B, the film thickness is shown over time at the center $h(0,t)$ (solid line) and rim $h(r_{rim},t)$ (dotted line). The three approach velocities (1, 0.1, 0.01 mm/s) are shown in blue, green and red, respectively. Time $t$ = 0 in Figure 4.27B represents the observation of the first Newton ring for each approach velocity. The end of the curve represents the last processed Newton ring, with film rupture occurring a few milliseconds later. For $h(0,t)$, the fastest decrease in dimple film height was observed at the slowest approach speed, with very little change in film height at $V$ = 1 mm/s. For $V$ = 0.1 mm/s, the film center height stabilized at ~350 nm, while for $V$ = 0.01 mm/s, the film height continuously decreased during the entirety of the film drainage process. For $h(r_{rim},t)$, increased approach velocity led to longer film lifetime. For $V$ = 0.01 mm/s and $V$ = 0.1 mm/s, the minimum film thickness was reached, but for the

former, the film ruptured immediately, while for the latter, it remained in this state for ~150 ms prior to film rupture.

### *4.3.3 Water/mica*

To complement water/silica and water/sapphire interactions discussed previously, water/mica experiments were also conducted. The results for water/mica experiments are presented below, and compared with water/silica interactions (no comparison with water/sapphire is provided due to absence of a long-range attractive interaction).

Figure 4.28 shows water/mica interactions in *n*-heptane for pure water drop (blue) and 0.1 M KCl drop (cyan). The total travelled distance (red) of the drop was 2100 μm with 100 μm overlap (that is, there was 2000 μm between the bottom of the drop and the mica surface at start of the experiment). The drops were freshly generated, and the mica discs treated with sticky tape (remove top layer to create fresh surface) and used within 3 hours after cleaning in piranha solution. Due to experimental variability, results shown in Figure 4.28 have mica discs at different *n*-heptane exposure time prior to experiment: 28 minutes for pure water drop and 13 minutes for 0.1 M KCl drop. Figure 4.28 shows the force-displacement curves at various points of interest.

In the case of pure water drop, the bimorph began detecting attractive force at $t$ = ~15 s, where $D$ = 725 μm (shown in Figure 4.28, blue force curve), or 625 μm (minus 100 μm overlap) from the mica surface. Change in drop shape was not visible from side-camera images until $t$ = 20 s ($D$ = 226 μm, $F$ = -5.5 μN). Contact between water drop and mica occurred at $t$ = 20.256 s ($D$ = 206 μm, $F$ = -7.0 μN; yellow dot in Figure 4.28), with rupture immediately after at $t$ = 20.257 s ($D$ = 206 μm, $F$ = -7.6 μN). From the displacement curve, droplet elongation was 106 μm, which is very close to the value obtained from side-view camera images (103 μm) and within visual error of +/-2 pixels, or +/-15 μm. Unlike for water/silica interactions, no "jump-in" was observed and the drop remained attached to the capillary after film rupture. At contact/rupture, the drop width decreased by 0.8% and the drop height increased by 7.3%. After rupture, the force rapidly decreased to -157 μN at $t$ = 20.288 s ($D$ = 202 μm), and returned to ~-125 μN once the bimorph stabilized. However, from Figure 4.28, the attractive force continued to increase as the capillary

continued its descent, with a force of -157 μN observed during 3 s hold (indicated by purple dot in Figure 4.28). The local force minimum corresponded to the arrest of spontaneous water drop spreading on the mica surface, after which the force continued decreasing more slowly, due to the continued lowering of the capillary. Upon withdrawal (not shown), the attractive force decreased slowly until the drop detached from the capillary at $t$ = 23.734 s.

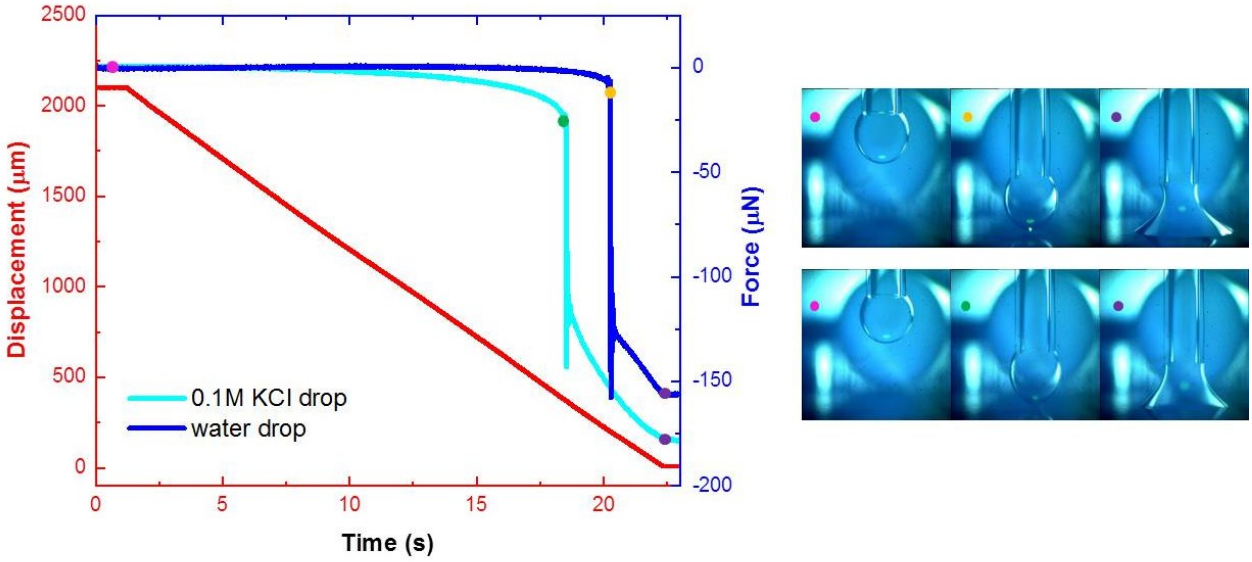


Figure 4.28 Displacement (red) and interaction force, as a function of time, for a droplet (pure water drop – blue, 0.1 M KCl - cyan) approached to 0° mica in *n*-heptane (solvent exposure time of 13 min and 28 min for cyan and blue curves, respectively). Side-camera images, for corresponding coloured dots indicated on force curves, are shown on the right, for $t$ ~ 0 s (pink), $t$ = 18.512 s (green), $t$ = 20.256 s (yellow) and $t$ = 22.5 s (purple).

In the case of 0.1 M KCl drop, the bimorph began detecting attractive force at $t$ = ~6 s, where $D$ = 1600 μm (see Figure 4.28, cyan), or 1500 μm from the mica surface. The mica substrate solvent exposure time was 13 minutes (less than the case for fresh water drop at 28 minutes). Surprisingly, the interaction force and elongation for 0.1 M KCl drop was stronger than for pure water drop (-25.6 μN vs. -7.0 μN, respectively), contrary to expectations based on previous observations for silica (see Figure 4.14, section 4.3.1.4). In previous silica experiments, at the same solvent exposure time (32 minutes), 0.1 M KCl showed half the elongation compared to

observed elongation of a pure water drop. Clearly, substrate solvent exposure time is one of the most important variables affecting the interaction force range and drop elongation. For mica, the attractive interaction force of 0.1 M KCl drop is about 3 times larger than for a pure water drop – simply due to solvent exposure time of 13 vs. 28 min, respectively. Comparison between silica and mica is shown Figure 4.29 and will be discussed in the next paragraph. For 0.1 M KCl drop/mica system, despite force detection at $t$ = 8 s, change in drop shape was not visible until $t$ = 17 s ($D$ = 524 μm, $F$ = -11.5 μN), as shown in Figure 4.28. Drop/mica contact occurred at $t$ = 18.512 s ($D$ = 370 μm, $F$ = -25.6 μN; green dot in Figure 4.28), with rupture immediately after at $t$ = 18.513 s ($D$ = 370 μm, $F$ = -25.7 μN). As mentioned above and visible in side-camera images shown in Figure 4.28, droplet elongation was observed, but no "jump-in": at contact, drop width decreased by 3.9% and height increased by 17.3%. 0.1 M KCl generally decreases drop elongation compared to pure water for silica, and the same trend is likely true for mica. However, despite salt addition, there was significantly more elongation percentage here compared to silica: 17.3% vs. 10.8% (see Figure 4.14). Clearly, solvent exposure time of mica (28 vs. 13 min.) to *n*-heptane plays a critical role in determining droplet elongation behaviour. After film rupture, the force rapidly decreased to -143 μN at $t$ = 18.545 s ($D$ = 368 μm), and returned to ~-120 μN once the bimorph stabilized. However, from Figure 4.28, the attractive force continued increasing as the capillary approached the surface, similar to the case of pure water drop. Upon withdrawal, the attractive force began slowly decreasing, with droplet detachment from capillary occurring at $t$ = 26.097 s.

Comparison between force curves of silica and mica interactions in *n*-heptane is shown in Figure 4.29. Here, interactions with pure water drop are shown in Figure 4.29A (solvent exposure: 32 minutes for silica, 28 minutes for mica), while interactions with 0.1 M KCl (solvent exposure: 32 minutes for silica, 13 minutes for mica) are shown in Figure 4.29B. Force curves are shown in blue for mica and in cyan for silica substrates, with drop/substrate contact time indicated on each force curve with a green dot. For the water drop interacting with mica, as shown in Figure 4.29A, the bimorph detected an attractive force at $t$ = ~15 s, where $D$ = 725 μm. This is 625 μm (minus 100 μm overlap) from the mica surface, and at least 3 times less force range than for silica at similar substrate solvent exposure time (2000 μm or more, Figure 4.14). This also corresponds to about one third of the drop elongation compared to pure water drop interacting with silica

(20.3% vs. 7.3% for silica and mica, respectively), and the same relationship of about one third was observed with interaction force at drop/substrate contact (-23.1 μN vs. -7.0 μN for silica and mica, respectively). In the case of 0.1 M KCl interactions (Figure 4.29B), there was a significant difference in substrate exposure time to *n*-heptane, prior to the experiment, between mica and silica (13 vs. 32 minutes, respectively). This helps explain that despite the expected trend from Figure 4.29A (weaker elongation and weaker attractive force for mica substrate, compared with silica), the lower *n*-heptane exposure time resulted in a larger interaction force and larger drop elongation for mica. Specifically, about 60% larger drop elongation (17.3% vs. 10.8% for mica and silica, respectively), and about 30% larger attractive force on contact (-25.6 μN vs. -19.6 μN for mica and silica, respectively). Due to the difference in substrate exposure time, the relationship between elongation and interaction force is not as clear as it was for the water drop discussed earlier.

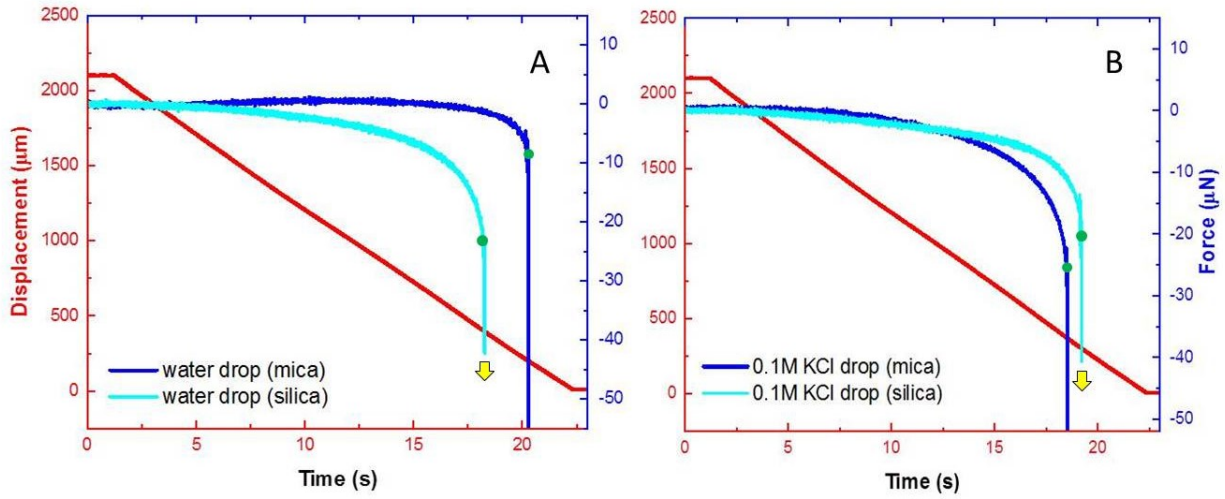


Figure 4.29 Displacement (red) and interaction force (blue, cyan) as a function of time, for a droplet (A - water, B - 0.1 M KCl) approached to 0° substrate (mica - blue, silica - cyan) in *n*-heptane. Drop contact time (green dot) and jump-in (yellow arrow) are indicated on each curve; no jump-in observed for mica.

## 4.4 Discussion

First, let us refer back to the expected disjoining pressure Π as a function of separation for a water drop interacting with various substrates in toluene or *n*-heptane, as shown in Figure 3.3. From these calculations, the only system where film thinning ($\Pi < 0$) is expected was for a water drop interacting with silica in toluene. The interaction between water and silica in *n*-heptane was expected to be very weakly repulsive (a very thin stable film of ~3 nm is expected), while the other systems discussed in this chapter (water/*n*-heptane/mica, water/*n*-heptane/sapphire) were expected to be firmly repulsive with a stable film forming 10-15 nm from the substrate surface.

For the case of water drop interacting with silica in toluene, film thinning and rupture were indeed observed for this system, as expected. The results of other experiments discussed in this chapter were different from those anticipated based on calculated disjoining pressure plots shown in Figure 3.3. Specifically, film thinning and rupture were observed for all water/silica and water/mica interactions in *n*-heptane. Even more unexpected was the long-range (up to 5 mm in some cases) hydrophilic attraction force between water and silica/mica in *n*-heptane that led to significant drop deformation and elongation in close proximity to the silica/mica surface. The magnitude of this attractive force (as well as drop elongation) was influenced by several variables, such as drop pH, drop ageing time, presence of KCl, drop approach velocity and surface roughness. The biggest factor of influence was substrate exposure time to *n*-heptane prior to experiment, which was shown to increase the water contact angle over time, leading to the eventual "disappearance" of this long-range attractive force or any drop deformation/elongation. In those cases, film thinning and rupture were still observed, instead of the expected ~3 nm stable repulsive film anticipated for the water/*n*-heptane/silica system. For the case of sapphire, due to the very rapid deterioration of the substrate hydrophilicity over time of exposure to *n*-heptane, no long-range attractive force or drop deformation were observed (there are practical limits of experimental calibration and setup (15 min+)). Localized thin film rupture was observed even for 60° silica and 107° sapphire in *n*-heptane, as evidenced by large adhesion forces (40-45 μN and 77-83 μN, respectively) observed during vertical capillary withdrawal from the surface. What could be the cause of the long-range hydrophilic attraction observed for water/ *n*-heptane/mica and water/*n*-heptane/silica systems? Some hypotheses will be discussed below.

Conventionally, the electrical double layer is not considered to have any significant presence in non-polar liquids. Due to a very low solubility of ions in non-polar liquids (electrostatic barrier to charging is much greater than $k_BT$)[103], a diffuse layer of charge cannot be generated. However, in certain circumstances, surface charging has been observed in non-polar media. For example, amphiphilic molecules that can form inverse micelles could facilitate the charging of surfaces by enhancing the solubility of ions in the non-polar liquid. Briscoe and Horn[104] measured a long-range repulsive force between two mica surfaces immersed in *n*-decane with trace levels of water and some anionic surfactant (sodium di-2-ethylhexylsulfosuccinate (AOT)) by using the SFA. This phenomenon is unlikely to be responsible for the long-range attractive force observed in this work as no surfactants were added to *n*-heptane.

The closest to a long-range "hydrophilic" interaction between a water drop and solid in a non-polar solvent was observed by Shi *et al.*, who looked at interactions between water drops and polyelectrolyte surfaces in toluene using AFM.[77] They observed a long-range "hydrophilic" interaction for all polyelectrolyte surfaces (cationic, anionic and zwitterionic), with the strongest interaction measured for the zwitterionic PMAPS, or poly(3-[dimethyl(2-methacryloyloxyethyl) ammonium] propanesulfonate), surface. For PMAPS, an attractive force (reached ~0.75 nN before attachment) with ~500 nm range was observed for an 88 μm water drop approaching the PMAPS surface at 1 μm/s. The authors attributed the long-range "hydrophilic" force to strong dipolar interactions due to large dipole moment of polyelectrolytes and ion hopping.[77] While intriguing, the clean silica, sapphire or mica surfaces used in this work did not have polyelectrolytes present on their surface (or elsewhere in the system).

There have also been reports of a long-range attractive force in the range of 1 μm in non-polar ($\varepsilon$ = 2.0) solvents such as cyclohexane[105] and *n*-dodecane[106] between silica and mica surfaces measured using AFM. In *n*-dodecane, Barbagini *et al.*[106] used $H_2SO_4/H_2O_2$ piranha solution for cleaning of silica surfaces right before experiment, similar to this work. Interestingly, they observed a decay in the measured attractive force between a spherical silica probe and flat silica surface over the course of 60 minutes, in both ambient (60% relative humidity) and nitrogen atmosphere. They hypothesized this attractive force to be electrostatic in nature, with accumulation of charge on silica (an insulator; electrical resistivity of ~$10^{16}$ Ω·m) surfaces due to

cell setup procedure (pumping solvent into AFM liquid cell using Teflon tubing) and the static charge dissipating over time, resulting in the observed diminishing of attractive force. Kanda *et al.*[105] measured interaction force between spherical silica probe and freshly cleaved mica in cyclohexane, and found a similar long-range attractive force due to a hypothesized initial charging of surfaces. They observed a reduction in attractive force magnitude over time, with no long-range attractive force observed at 7 minutes of solvent exposure time prior to AFM measurement. While these results are not directly applicable to the system in this chapter (solid particle approached to the surface, in place of a water drop), electrostatics is an interesting proposition.

Electrostatics is active over a wider range of distance compared with surface forces, and would generally require that the surfaces of the water drop and silica/mica be oppositely charged for an attractive force to be observed (in the case of conducting objects, it is possible to observe attraction between like-charged non-flat entities[107,108]). How such surface charge could be generated inside the DFA cell setup is not clear. While the high resistivity of *n*-heptane ($\sim 10^{16}$ $\Omega \cdot m$), as with other hydrocarbons, makes it susceptible to electrostatic charging during flow[109] (e.g. through non-conductive pipes, tubing, etc.), the DFA cell (see Figure 3.4) has a vertical metal channel (carries bimorph wiring to charge amplifier) that can effectively act as a conductive channel. All users must wear an anti-static bracelet while the bimorph is operational (protect sensitive electronics inside signal amplifier), which excludes any electrostatic contribution from the user. In addition, the cell was filled with *n*-heptane at least 1 hour prior to commencement of experiment, in order to pre-warm the bimorph (important to obtain reliable signal), which could help dissipate any electrostatic charging. Finally, it is unclear why long-range interaction in toluene or with hydrophobic substrates would be absent if the cause is purely static charging due to DFA cell setup. For these reasons, it is not clear if the charging mechanism as described by Barbagini *et al.*[106] and Kanda *et al.*[105] could be responsible for the long-range hydrophilic attractive force observed here.

The relevant long-range attractive force data from researchers described above, as well as findings of this work, are shown in Table 4.2. The probe-scaled force values (mN/m) in this work are significantly larger than any attractive force observed by other researchers. For the

water drop interacting with PMAPS-coated silica surface, it was ×600-3200+ larger, while results between silica and mica in cyclohexane were closer but still significantly less (×13-74 smaller than this work). The distance range of detected force is significantly larger in this work as well, at 4-10+ thousand times larger than Shi *et al.*[77], and 2-5 thousand times larger than Kanda *et al.*[105] and Barbagini *et al.*[106]

Table 4.2 Comparison of attractive force magnitude and range for different systems

| Experiment | System | Water/particle radius, $R$ | Attractive Force, $F$ | $F/R$ (mN/m) | Range |
|---|---|---|---|---|---|
| Shi *et al.*[77] | water drop / PMAPS, in toluene | 44 μm | 0.75 nN | 0.02 | 500 nm |
| Barbagini *et al.*[106] | silica sphere / silica, in dodecane | 10 μm | – | 0.20 | 1 μm |
| Kanda *et al.*[105] | silica sphere / mica, in cyclohexane | 4.55 μm | 4 nN | 0.88 | 1 μm+ |
| This work | water drop / silica or mica, in *n*-heptane | 0.85 mm | 10-55 μN | 11.8 – 64.7 | up to 2 mm+ |

Water droplet elongation and consequent rupture is a well-documented phenomenon in the presence of an electric field, also known as electrocoalescence. When a uniform electric field is applied to an elastic conductive body, such as a water drop, it will deform in the direction of the electric field due to the electric stress on the surface.[110] Once the electrostatic pressure exceeds the capillary pressure, the water droplet will break up. This is often observed when deformed water drop ratio of major axis to minor axis reached 1.9, and corresponds to an electric field strength of 3.5 kV/cm for 1.2 mm drop in *n*-heptane.[111] However, no external electric field was applied to the experimental system in this work and cannot explain the observed water droplet elongation and long-range attractive phenomena described in this chapter. For a successful force measurement on the DFA instrument, the bimorph must be fully insulated from the organic continuous phase (toluene, *n*-heptane) using a Teflon sheath. In case of any leaks inside the sheath, this would be immediately apparent as the bimorph would become damaged and no signal would be generated. For example, fluorinated ethylene propylene (FEP) sheaths have been used to protect the bimorph for aqueous systems by other users of DFA instrument, but these

sheaths are penetrable to organic solvents (toluene, *n*-heptane), with the damage and loss of bimorph functionality promptly observed.

There are a few items of special consideration with these experiments that should be noted in order to successfully observe an extra long-range attractive force and water droplet elongation on approach to a hydrophilic silica or mica surface. In addition to low substrate exposure time to *n*-heptane prior to experiment, the entire setup must be very clean to observe drop elongation. In some cases, despite meticulous attention paid to system cleanliness, setup, fresh substrates, etc., no long-range force or drop elongation were observed in some experimental runs. The reason for this is hypothesized to be related to minute contamination of the system (no long-range force was observed with "dirty" systems, as will be discussed in more detail in Chapter 6), but the true cause is unknown and more work is required to understand the underlying issue. In some of the earlier experiments, vibrations from the camera motor/cooling fan were visible in high-speed side-camera images, as evidenced by slight sideways movements of the water drop. The small oscillation of descending drop observed in earlier experiments had no effect on the extra long-range attractive force or droplet elongation; these camera-induced vibrations were removed in later experiments with the use of a custom-built camera mount that fully decoupled the camera from the vibration-free air table on which the DFA experiment was conducted. It is difficult to say at what *n*-heptane exposure time the contact angle of 0° silica has increased significantly enough so as to remove any long-range interaction force and drop elongation. In some cases, one can observe an attractive interaction force between a drop and silica as far as over an hour of silica exposure time to *n*-heptane prior to experiment (for example, in the case of pH 9.7 water drop at 78 minutes of *n*-heptane exposure). Finally, the true maximum range of the attractive force at low exposure time to *n*-heptane prior to experiment could not be determined. As shown in Figure 4.19, even at 5 mm separation between drop and silica substrate, which is the maximum possible given limitations of the cell setup and the displacement sensor, an attractive force was detected by the bimorph as soon as the water droplet began its descent towards the silica substrate. It is worth noting that based on Coulomb's law the electrostatic force, similar to the universal gravitation force, has a $1/d^2$ dependence, where $d$ is the separation between two charges. From this perspective, the extra long-range attractive force would have an essentially infinite range, with detection limit dictated by the sensitivity of the bimorph (0.1 μN). However,

since the mechanism behind the observed extra long-range attractive force is not yet understood, conducting drop/silica experiments in *n*-heptane at larger separations would be of interest, as well as a baseline experiment measuring the drop/silica interaction in air (high resistivity medium).

Various parameters related to long-range attractive force and drop elongation described in this chapter for liquid/solid clean systems are shown in Table 4.3. The cases where no long-range force was observed, such as not fully hydrophilic substrates (60° sapphire, 107° silica) and where the continuous phase was toluene, are not shown in this table. As described earlier, *D* refers to displacement and *F* refers to observed force at drop/substrate contact. As displacement also included the programmed overlap, the undeformed drop/substrate separation was 100 μm less than the displacement. The force shown in Table 4.3 refers to the original, unadjusted value (in some cases, the force was adjusted when compared to systems with smaller total displacement).

Table 4.3 Summary of long-range attractive force in various liquid/solid clean systems

| Substrate | Substrate Exposure Time (min) | Drop | *n*-Heptane type | *D* (μm) | *F* (μN) | Elongation (%) | Velocity (mm/s) |
|---|---|---|---|---|---|---|---|
| silica | 32 | water | regular | 383 | -23.1 | +20.3 | 0.1 |
| | 31 | water | water sat. | 403 | -32.6 | +22.0 | |
| | 23 | water | | 466 | -36.4 | +25.2 | |
| | 17 | water | | 558 | -42.7 | +33.3 | |
| | 32 | 0.1 M KCl | regular | 306 | -19.6 | +10.8 | |
| | 22 | 0.1 M KCl | water sat. | 384 | -30.2 | +18.5 | |
| | 78 | pH = 9.7 | | 249 | -9.7 | +9.7 | |
| | 31 | pH = 9.7 | | 360 | -30.3 | +18.3 | |
| | 20 | pH = 12.2 | | 503 | -31.2 | +28.1 | |
| | 21 | water | | 373 | -27.7 | +9.7 | 0.5 |
| mica | 28 | water | regular | 206 | -7.0 | +7.3 | 0.1 |
| | 13 | 0.1 M KCl | | 370 | -25.6 | +17.3 | |

Details regarding experimental reproducibility for this Chapter are described below. The underformed water drop dimensions were $R$ = 0.85±0.02 mm and height of 1.47±0.03 mm.

Results discussed in this chapter and summarized in Table 4.3 were reproducible, and typically experiments were repeated 2-3+ times, with the most representative force curve data shown in figures. The magnitude of the attractive force on contact varied within ±5 μN. Percent drop elongation values at drop/silica contact were within ±0.5%, where 1% drop elongation corresponded to a 14-15 μm increase in drop height. It should be noted that in some experimental runs, qualitatively around 25% of the time, no long-range force or drop elongation were observed, despite the best efforts to maintain a clean and meticulous experimental setup.

Regardless of water drop composition (pure, alkaline, high salt), reducing exposure of substrate to *n*-heptane prior to approach of the drop to the surface led to a stronger attractive force on contact, and larger drop elongation. As discussed in the Introduction sub-section, the contact angle of the water drop deposited on clean, ~0° substrate (silica, sapphire) immersed in solvent (*n*-heptane, toluene) increased with increasing substrate exposure time to solvent prior to contact angle measurement. The mechanism behind this observation is not fully understood, but it is hypothesized that trace impurities in the solvent that adsorb onto the substrate surface over time may decrease the surface hydrophilicity and influence the observed water contact angle, thereby reducing the magnitude of the attractive force and drop elongation observed in DFA experiments. The saturation of *n*-heptane with water also led to higher attractive force and increased drop elongation, but the effect was not as pronounced as the substrate exposure time to *n*-heptane. The content of water in water-saturated *n*-heptane is estimated to be in the range of 82-151 ppm, based on values from the literature.[112] Alkaline drop jump-in time is sensitive to silica substrate exposure time to *n*-heptane (33 ms vs. 26 ms for 31 minute and 20 minute solvent exposure time), while no change was observed for pure water or 0.1 KCl drops regardless of silica solvent exposure time (10-11 ms jump-in time). The density and viscosity of the droplet remained unchanged for pure water, 0.1 KCl and alkaline pH, namely at 1 g/mL and 1 mPa·s, respectively. The slower jump-in time for alkaline drops may be related to the silica substrate: vicinal hydroxyl groups on the silica surface (generated after piranha cleaning) can dissociate and become charged when in contact with an alkaline environment (typically pH 10-11).[113]

Resistivity quantifies how strongly a substance resists the flow of an electric current and is an important determinant in electrostatic charging and charge decay. Conductivity (inverse of

resistivity; in S/m) and resistivity (in Ω·m) values for various components of the liquid/solid organic systems discussed in this chapter are shown in Table 4.4. It is interesting to note that the strongest attractive force and largest drop elongation correspond to the drop/solvent/substrate system with the highest resistivity values, namely water droplet/*n*-heptane/silica with resistivity values of $1.82 \times 10^5$ Ω·m, $10^{16}$ Ω·m and $10^{16}$ Ω·m, respectively. The electrostatic surface charge density $q$ as a result of decay can be described by $q = q_0 \cdot e^{-t/\tau}$, where $q_0$ is the initial surface charge density, $t$ is the time and $\tau$ is the relaxation time ($\tau = \rho\varepsilon$; product of resistivity and dielectric constant). From this relation, higher resistivity leads to a slower decay of electrostatic charge, potentially supporting the observation of higher attractive force and drop elongation for the pure water droplet/*n*-heptane/silica system relative to others shown in Table 4.3. Similarly, the drop elongation and attractive force on contact decreases with decreasing resistivity of the water droplet for the *n*-heptane/silica system, namely water ($1.82\times10^5$ Ω·m) > alkaline drop (1-1.25 Ω·m) > 0.1 M KCl (0.81 Ω·m). Comparing results for mica and silica in *n*-heptane, a stronger drop elongation and attractive force on contact was observed for silica ($10^{16}$ Ω·m) than for mica ($10^{11}$ - $10^{15}$ Ω·m). In all cases, exposure of the substrate to *n*-heptane prior to drop/substrate contact was a key determinant of attractive force and drop elongation on contact (less exposure increased the observed force and elongation). This is especially interesting when comparing silica and mica (see Table 4.3): in the case of water, the percent elongation and force on contact was about 3 times weaker for mica than silica (-7.0 μN vs. -23.1 μN, +7.3% vs. +20.3%) at similar substrate exposure time (~30 min.); but in the case of 0.1 M KCl, interaction with mica (-25.6 μN, +17.3%) was stronger than with silica (-19.6 μN, +10.8%) due to the shorter solvent exposure time for mica (13 min. vs. 32 min.). An intriguing resistivity observation is that while toluene ($10^{14}$ Ω·m) < *n*-heptane ($10^{16}$ Ω·m), and sapphire resistivity ($10^{14}$ Ω·m) is less than silica and (likely) mica, it is not clear why for toluene/silica or for *n*-heptane/sapphire systems, the long-range attractive force or drop elongation were not detected. It appears a combination of an electrostatic component and change in substrate wettability (increasing water contact angle) with substrate exposure time to *n*-heptane prior to drop/substrate contact could be responsible for the observed long-range attractive force and drop elongation. As discussed previously, the cause of any potential electrostatic charging is not clear. While the low resistivity of *n*-heptane (~$10^{16}$ Ω·m), as with other hydrocarbons, makes it susceptible to

electrostatic charging during flow, very high flow rates (1-2 m/s) through a small cross-section would be required.[109]

Table 4.4 Liquid/solid system conductivity and resistivity values

| Substrate | Conductivity (S/m) | Resistivity (Ω·m) |
|---|---|---|
| *n*-heptane[109] | $10^{-16}$ | $10^{16}$ |
| toluene[109] | $10^{-14}$ | $10^{14}$ |
| water (Millipore)[114] | $5.49\times10^{-6}$ | $1.82\times10^{5}$ |
| 0.1 M KCl [114] | 1.24 | 0.81 |
| pH = 9.7, 12.2 [114] | 0.8, 1.0 | 1.25, 1.0 |
| fused silica[109] | $10^{-16}$ | $10^{16}$ |
| mica[109] | $10^{-11}$ - $10^{-15}$ | $10^{11}$ - $10^{15}$ |
| sapphire[115] | $10^{-14}$ | $10^{14}$ |

## 4.5 Summary

The effect of different variables was explored on the presence, magnitude and range of an attractive, extra long-range attractive force between a water drop and a solid substrate (silica/mica/sapphire) in *n*-heptane or toluene. It was established that no long-range attractive force was observed between a water drop and 0° silica in toluene, as well as with non-hydrophilic substrates (60° sapphire, 107° silica) in *n*-heptane. In the latter case, a larger dimple was observed at higher water drop approach velocities, as expected from previous results in the literature,[12,71] with good agreement between experiment and SRYL modeling at 1 mm/s and 0.1 mm/s approach velocities. No long-range attractive force was observed between 0° sapphire and water in *n*-heptane, hypothesized to be due to the fast reduction in the observed level of hydrophilicity of sapphire once submerged in *n*-heptane.

An attractive force was observed between a water drop and 0° silica or 0° mica in *n*-heptane, with observed drop vertical elongation and decrease in drop width, especially at small (several μm) water drop/substrate separation. Immediate thin film rupture occurred on contact, with film

lifetime typically under 1 ms, followed by rapid movement of the three-phase contact line leading to jump-in (drop detachment from capillary) in ~10 s (longer for high pH; no jump-in for mica or rough surface). The range of the extra long-range attractive force is (a) at least 5 mm at short silica ageing time in *n*-heptane, and (b) disappears after a long (~1.5-2 hours) silica ageing time in *n*-heptane. No clear cause for this long-range hydrophilic attractive force has been identified, with electrostatics and decreasing substrate hydrophilicity with exposure time in *n*-heptane (increasing contact angle of water deposited on solid with longer *n*-heptane immersion) hypothesized as key contributing factors.

Ageing of the water drop (up to 15 minutes) in *n*-heptane prior to experiment did not have a significant impact on the drop elongation or attractive force magnitude. The magnitude of the attractive force and vertical drop elongation both decreased with increasing silica exposure time to *n*-heptane prior to water drop/surface contact, as expected from the increasing contact angle of water placed on silica as a function of submersion time in *n*-heptane. This *n*-heptane exposure time effect was also present when the composition of the water drop was altered (0.1 M KCl, alkaline pH drop). In general, larger drop elongation on drop/substrate contact was accompanied by (a) a steeper attractive force curve during drop approach, (b) larger attractive force at drop/silica contact, and (c) decreased drop width at drop/silica contact. For the same *n*-heptane exposure time of silica prior to water/silica contact, water-saturated *n*-heptane increased force strength and drop elongation, while 0.1 M KCl had the opposite effect. For 0.1 M KCl, the attractive force in regular *n*-heptane saw a stronger "screening" effect (10.8% vs. 18.5% drop elongation) over water-saturated *n*-heptane (20.3% vs. 25.2% drop elongation), when compared with equivalent conditions for a pure water drop, respectively. For an alkaline drop at pH 9.7, the drop elongation was somewhat weaker than for pure water (18.3% vs. 22.0%); this observation is likely true at pH 12.2 but was difficult to ascertain among competing parameters of substrate ageing in *n*-heptane and drop alkalinity level. A faster drop approach velocity (0.5 mm/s vs. 0.1 mm/s) led to smaller drop elongation and weaker attractive force at drop/silica contact; the majority of the drop elongation occurred close to the silica substrate (e.g. up to 60% occurred over 5 μm vertical travel), and at a higher approach velocity, the drop spent proportionally less time in this zone. Drop elongation and long-range attractive force were also observed between a water drop and a hydrophilic roughened silica substrate, but with mixed reproducibility. For

mica substrate, the interaction with a water drop in regular *n*-heptane showed weaker attractive force on drop/mica contact and smaller drop elongation than at equivalent conditions for silica (7.3% vs. 20.3%, respectively). Interaction with 0.1 M KCl drop and mica showed a strong time dependence, with longer drop elongation at 13 minutes mica exposure to *n*-heptane than for pure water drop at 28 minutes of *n*-heptane exposure (17.3% vs. 7.3% elongation, respectively). Unlike for silica, no jump-in (drop detachment from capillary) was observed for mica. Finally, experiments were limited to 5 mm vertical displacement range due to displacement sensor and DFA cell setup limitations.

# Chapter 5: Organic Systems – Liquid/Liquid Interactions

## 5.1 Introduction

In real-world systems such as W/O emulsions in bitumen production, there are many species that could stabilize emulsified water droplets, such as fine solids (e.g. clays) and surface-active molecules (e.g. asphaltenes, naphthenic acids).[1,3,13] In addition to studying impacts of specific stabilization mechanisms of "contaminated" systems, it is important to gain a better understanding of interaction forces of pure water drops in organic media or "clean" systems, including in higher *Re* hydrodynamic regime that is inaccessible in a typical AFM drop probe experiment ($Re > 0.02$). In this chapter, the interaction force between two water drops in *n*-heptane is studied using the DFA instrument.

## 5.2 Toluene

No long-range attractive force was detected in the interaction between a droplet deposited on 0° silica and a water droplet approached with a capillary, while immersed in toluene, as also confirmed previously in the literature.[29] These observations are in line with similar observations discussed in Chapter 4 and will not be expounded on here.

## 5.3 *n*-Heptane

The interaction between water drops in *n*-heptane is discussed in this section, with the effect of the bottom water drop and silica ageing time (exposure to *n*-heptane prior to experiment), as well as the effect of pH, discussed in more detail. All experimental results presented in this chapter used water-saturated *n*-heptane.

*5.3.1.1 Effect of water droplet ageing time*

To explore the effect of ageing time of the bottom water drop on the interaction force between two water drops, the exposure time of the bottom water drop on silica to *n*-heptane (water-saturated) prior to experiment was tested at 35 and 20 minutes exposure time. Interaction force curves are shown in Figure 5.1, where force curves for 35 and 20 minutes exposure time are shown in blue and cyan, respectively. Figure 5.1A shows the full drop/drop interaction ($V = 0.5$

mm/s approach, 3 s hold, and retraction at $V$ = 1 mm/s), while Figure 5.1B shows the approach trajectory only, until drop/drop jump-in. Drop/drop contact and drop jump-in are indicated in Figure 5.1B with pink dots and yellow arrows, respectively. Separation between water drops (vertical distance between the bottom of the top water drop and the top of bottom water drop) was 4900 µm at the start of the experiment ($D$ = 5000 µm). The bottom water drop was placed on 0° silica surface prior to careful submersion of silica into *n*-heptane, and a freshly generated top water drop was approached to the bottom drop (after 35 or 20 minutes ageing in *n*-heptane) at $V$ = 0.5 mm/s. As in Chapter 4, the precise location of the surface (in this case, the top of the bottom water drop) was detected by observing the first Newton rings from the bottom camera between an air bubble and the bottom drop; a side-camera image is shown in Figure 5.2A. For both the 35 and 20 minutes cases, an attractive force was observed as soon as the top drop began moving at $t$ = 1.22 s, and the top water drop progressively elongated downward during descent.

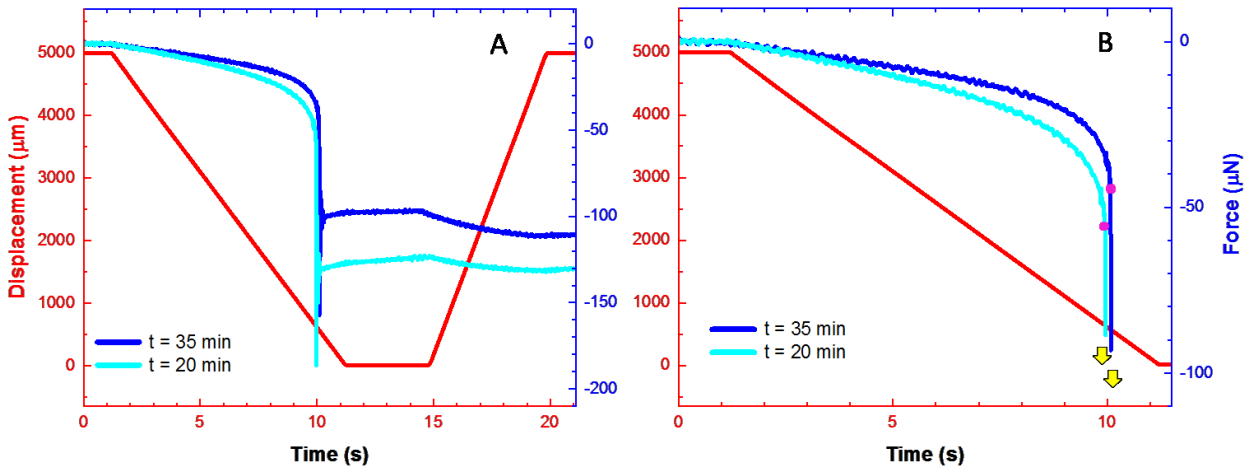


Figure 5.1 Displacement (red) and interaction force (blue, cyan) as a function of time, for a water drop approached to a water drop (deposited on 0° silica) in *n*-heptane. Drop on silica ageing time (35 min, 20 min) is shown in the legend. Drop/drop contact time (pink dots) and jump-in (yellow arrow) are indicated on each curve. (A) full interaction curve, (B) jump-in section only.

For 35 minutes *n*-heptane exposure (blue curve in Figure 5.1), drop/drop contact was observed at $t$ = 10.077 s ($D$ = 613 μm, $F$ = -44.2 μN), followed by film rupture at $t$ = 10.078 s ($D$ = 613 μm, $F$ = -46.4 μN) and drop jump-in at $t$ = 10.086 s ($D$ = 609 μm, $F$ = -93.1 μN). For the drop/drop interaction, jump-in time is defined as the time between drop/drop contact and the detachment of top drop from the capillary; for 35 minutes *n*-heptane exposure, jump-in time was 9 ms. The top water drop elongated by 17.2% (270 μm), with a 5.6% decrease in drop width. Surprisingly, the bottom water drop also elongated, or "pinched", upwards towards the top drop by over 200 μm (it is not possible to calculate the percentage value as the original height of the bottom drop is not easily discerned from side-camera images), as can be seen in the side-camera image in Figure 5.2B. It should be noted that, due to the bottom water drop "pinching" upwards, film rupture and film lifetime were not discernable from the bottom camera (no Newton fringes were visible, due to the objective focal plane aligned on the original, un-deformed bottom drop surface) and were observed from side-camera images only.

For 20 minutes *n*-heptane exposure (cyan curve in Figure 5.1), drop/drop contact was observed at $t$ = 9.956 s ($D$ = 674 μm, $F$ = -56.7 μN), followed by film rupture at $t$ = 9.957 s ($D$ = 674 μm, $F$ = -58.2 μN) and drop jump-in at $t$ = 9.963 s ($D$ = 671 μm, $F$ = -88.6 μN). A drop jump-in time of 7 ms was observed, which is shorter compared to 9-10 ms commonly observed for drop/silica interactions discussed in Chapter 4, as well as the drop/drop interaction at 35 minute *n*-heptane exposure time discussed in the previous paragraph. As with 35 minutes *n*-heptane, for 20 minutes *n*-heptane exposure the top water drop elongated downwards by 21.5% (327 μm), with a 6.9% decrease in drop width. The bottom drop elongated upwards by 242 μm. The total increase in height for both (top and bottom) drops of 569 μm is in good agreement with expected separation of un-deformed drops of 574 μm at $t$ = 9.956 s ($D$ = 674 μm). A visual comparison of top and bottom drop elongation at both bottom drop ageing times (35 and 20 minutes) is shown in side-camera images in Figure 5.2. As mentioned previously, Figure 5.2A indicates the location of the top of the bottom droplet via a calibration air bubble, while Figure 5.2(B,C) shows drop/drop contact time for 35 minutes exposure (10.077 s) and 20 minutes exposure (9.956 s), respectively. The increased elongation of the top drop with shorter exposure time of the bottom water drop to *n*-heptane prior to experiment is visible from side-camera images in Figure 5.2(B,C). This difference is somewhat surprising, as contact angle measurements of a water drop on 0° silica in

*n*-heptane (water drop was deposited on a 0° silica disc prior to immersion in *n*-heptane) remained constant at ~0° for the duration of the experiment (several hours).

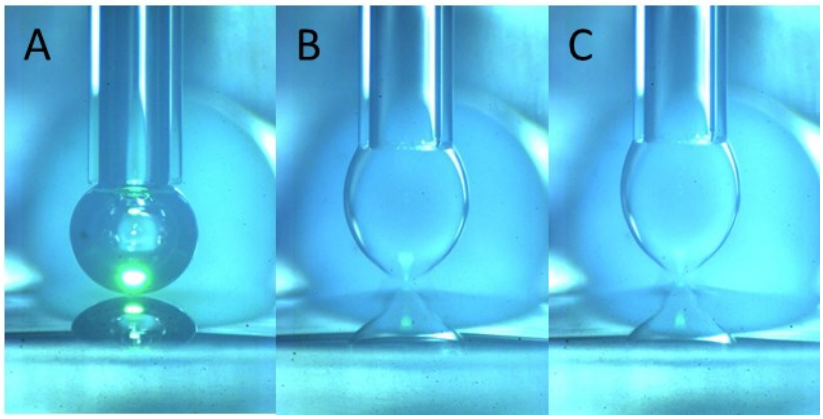


Figure 5.2 Side-camera images: (A) calibration bubble (establish location of undeformed bottom drop), (B-C) drop/drop contact for 35 min and 20 min ageing time of bottom drop, respectively.

Similar to results in Chapter 4 for water drop and silica interactions, both top and bottom drop elongation had mostly occurred in close proximity to each other. For example, for 20 minutes *n*-heptane exposure, the details regarding change in drop dimensions over time are shown in Figure 5.3 and Figure 5.4. In Figure 5.3, change in top drop dimensions are shown as a function of distance (Figure 5.3A) and force (Figure 5.3B). In Figure 5.3, changes in top drop height and width (zero represents original drop size) are shown in dark green and light green, respectively, with dotted lines shown as an eye guide only. From Figure 5.3, 41% of total top drop elongation was observed within 5 ms prior to drop/drop contact, with 63% of the total top drop elongation observed within 50 ms of drop/drop contact. Similarly, 47% of total top drop width reduction was within 50 ms of drop/drop contact (width was measured at the widest point of the drop). From Figure 5.3B, the observed attractive force increased rapidly as the top drop began progressively elongating (within 50 ms of drop/drop contact). These changes are illustrated with a time-lapse of side-camera drop images shown in Figure 5.4: drop elongation (a-l), film rupture (m), drop "jump-in" (l-r) and drop bounce (s-t), with time stamps, in seconds, indicated in the top right corner for each side-camera image. The original drop size is shown in Figure 5.4a, with the first top drop deformation visible at $t = 9$ s (Figure 5.4b). As the top drop progressively elongated (Figure 5.4c-k), changes in the bottom drop dimensions, though more subtle, also became

apparent. Specifically, the top of the bottom water drop near the back center, while initially out of focus (Figure 5.4b), became increasingly more clear (Figure 5.4c,d), most likely due to increased drop height in the center of the bottom drop (upward elongation), located in the side-camera focal plane at the capillary/top drop (experiments were conducted in the center of the silica substrate). Another interesting aspect was the reflection of the top drop visible in the bottom drop. Under un-deformed conditions, this reflection remains symmetrical (as seen with the calibration bubble in Figure 5.2A). Upon careful observation, the asymmetrical reflection of the top drop became apparent after $t$ = 9.9 s (Figure 5.4d), commensurate with increased curvature (upwards elongation) of the bottom drop. The bottom drop became increasingly "pointed" (Figure 5.4e-k), with progressive distortion in top drop reflection. Finally, over the course of 1 ms (Figure 5.4*l*), a total elongation of 142 µm was observed, split roughly equally between the top drop "funneling" downward and the bottom drop "funneling", or pinching, upward (78 µm and 64 µm for top drop and bottom drop, respectively). Following jump-in (Figure 5.4*l*-r), the remaining top drop detached, with observed bouncing (Figure 5.4s-t).

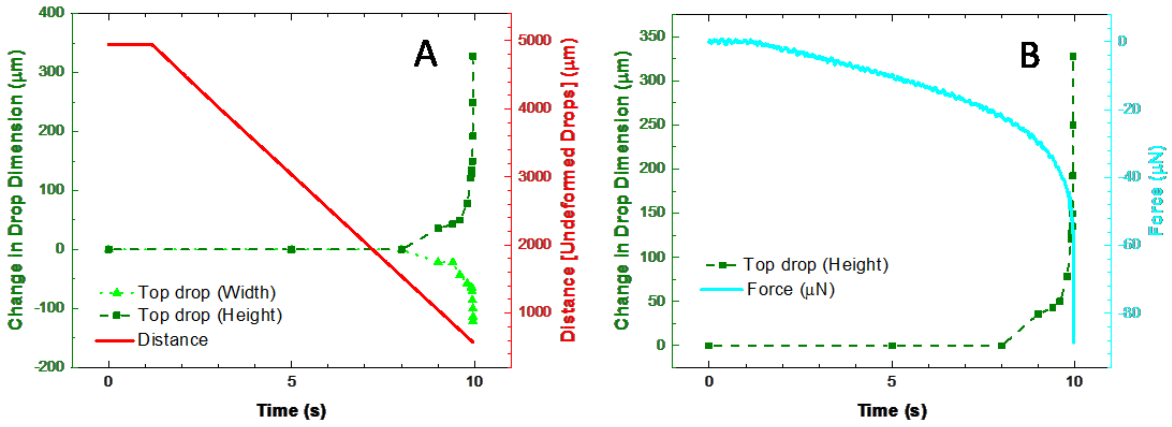


Figure 5.3 Change in dimension of the top water drop (dark green) over time, interacting with the bottom water drop (light green) on 0° silica in *n*-heptane (water sat.), as a function of (A) distance (based on undeformed drops; red) and (B) interaction force (cyan).

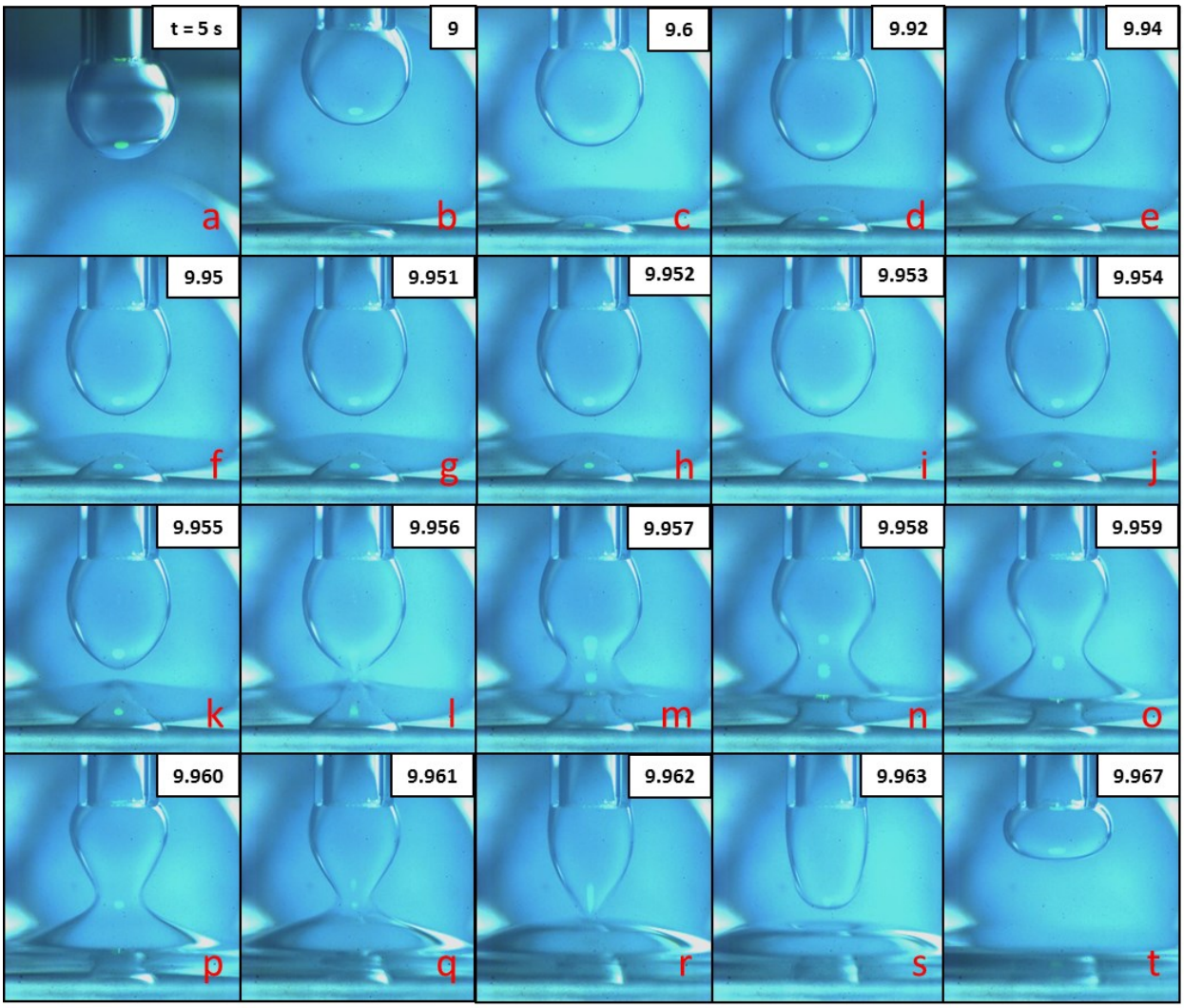


Figure 5.4 Side-camera images of a water drop approached to another water drop (deposited on 0° silica) in *n*-heptane (water sat.): drop elongation (a-l), film rupture (m), drop "jump-in" (l-r) and drop bounce (s-t). Time stamps, in seconds, are shown in the top right corner for each side-camera image.

*5.3.1.2 Effect of substrate ageing time*

To explore the effect of substrate ageing time in *n*-heptane on the interaction force between two water drops, the exposure time of the silica substrate was tested at two different conditions (17 and 23 minutes) while the ageing of the subsequently deposited water drop on the silica substrate was maintained the same (17 minutes). It should be noted that the drop left on the silica surface after a drop/silica interaction was used as the bottom drop for these experiments, and the precise height of this water drop was not known. Displacement (red) and interaction force curves are shown in Figure 5.5, where force curves for 23 and 17 minutes silica exposure time (prior to bottom water drop deposition) are shown in blue and cyan, respectively. The displacement curve represents the distance between the bottom of the drop and the silica surface, and for this reason, it is shown as a dotted line: for the drop/drop interaction, the separation is not precisely known (slightly less than between drop and silica surface). Figure 5.5 shows the drop/drop interaction ($V$ = 0.1 mm/s) until drop/drop jump-in, with drop/drop contact and drop jump-in indicated with pink dots and yellow arrows, respectively. Separation between the bottom of the top water drop (freshly generated) and the silica surface was 1500 μm at the start of the experiment ($D$ = 1600 μm); this is the displacement curve shown in Figure 5.5. It should be noted that the location of the top of the bottom water drop was not calibrated with a bubble (due to experimental constraints) and was not precisely known. For both drops, an attractive force was observed as soon as the top drop began moving at $t$ = 1.22 s, and the top water drop progressively elongated during descent.

For 23 minutes *n*-heptane exposure prior to bottom drop deposition (blue curve in Figure 5.5), drop/drop contact was observed at $t$ = 12.462 s ($D$ = 494 μm, $F$ = -13.1 μN), followed by film rupture at $t$ = 12.463 s ($D$ = 494 μm, $F$ = -14.4 μN) and drop jump-in at $t$ = 12.470 s ($D$ = 493 μm, $F$ = -38.8 μN), for a drop jump-in time of 8 ms. The top water drop elongated by 13.9% (199 μm), with a 3.8% decrease in drop width. Similar to prior results, the bottom water drop also elongated, or "pinched", upwards towards the top drop, with a total bottom drop height of 195 μm at contact from the displacement curve. As discussed previously, due to the bottom water drop "pinching" upwards, film rupture and film lifetime could not be detected from the bottom camera. As previously, the majority of droplet elongation occurred close to the bottom drop: 43% within 5 ms of drop/drop contact, and 57% within 50 ms of drop/drop contact.

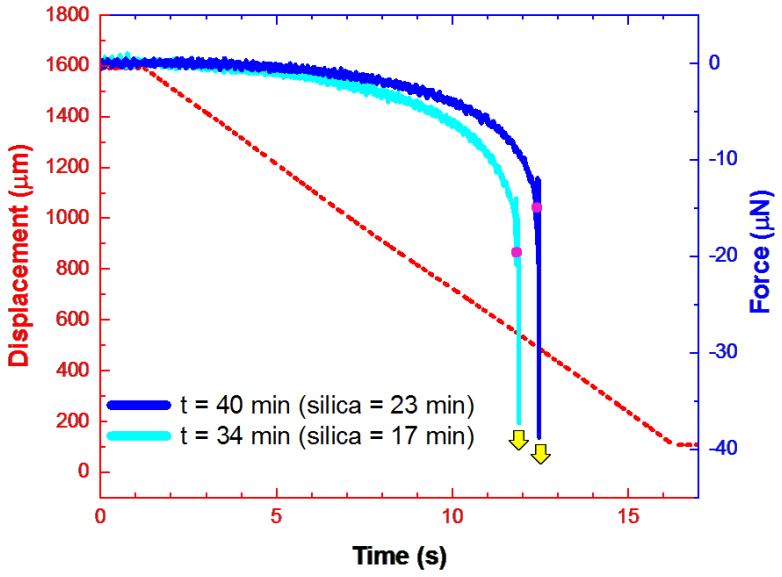


Figure 5.5 Displacement (red) and interaction force (blue, cyan) as a function of time, for a water drop approached to another water drop deposited on 0° silica (silica exposed to *n*-heptane for 23 and 17 minutes for blue and cyan curves, respectively) in *n*-heptane. Drop/drop contact time and jump-in are indicated with pink dot and yellow arrow, respectively.

For 17 minutes *n*-heptane exposure (cyan curve in Figure 5.5), drop/drop contact was observed at $t$ = 11.881 s ($D$ = 551 μm, $F$ = -20.3 μN), followed by film rupture at $t$ = 11.882 s ($D$ = 551 μm, $F$ = -21.1 μN) and drop jump-in at $t$ = 11.889 s ($D$ = 550 μm, $F$ = -37.3 μN), for a drop jump-in time of 8 ms. As with 23 minutes *n*-heptane case, for 17 minutes *n*-heptane exposure, the top water drop elongated downwards by 15.4% (220 μm), with a 4.3% decrease in drop width. The bottom drop "pinched" upward, with total bottom drop height on contact at 230 μm from the displacement curve. The majority of droplet elongation occurred close to the bottom drop: 45% within 5 ms of drop/drop contact, and 62% within 50 ms of drop/drop contact. Thus, the ageing of silica in *n*-heptane prior to deposition of bottom water drop impacts the top drop elongation and strength of the observed attractive force, with less *n*-heptane ageing resulting in stronger attractive force on drop-drop contact (-20.3 μN vs. -13.1 μN) and larger top drop elongation (15.4% vs. 13.9%).

The impact of silica ageing time in *n*-heptane on the strength of the interaction force is not as pronounced for the bottom water drop ageing in drop/drop experiments as it was for the silica substrate ageing in drop/silica experiments in Chapter 4. This difference is illustrated in Figure 5.6, where the drop/drop interactions shown in Figure 5.5 are paired with the equivalent force curves for the drop/silica systems, indicated in dark and light green for 23 and 17 minutes *n*-heptane ageing time, respectively (as shown previously in Figure 4.13). The force curves in Figure 5.6 are shown until drop/silica or drop/drop jump-in.

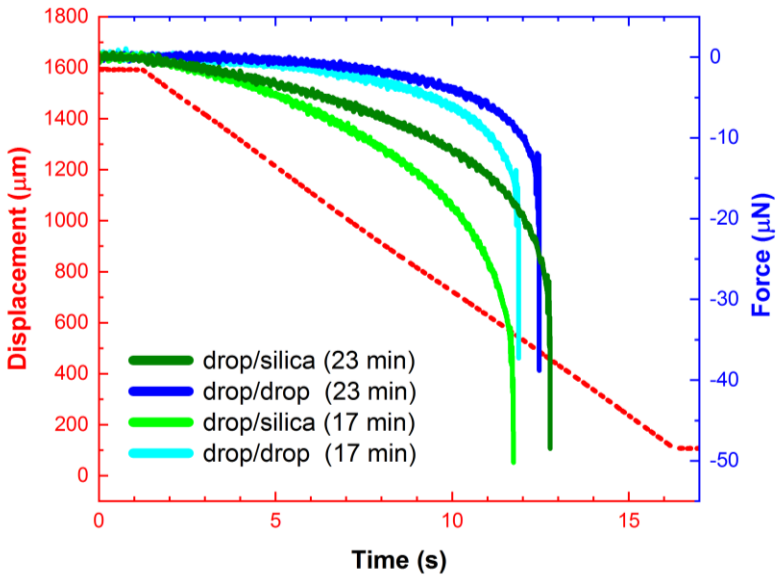


Figure 5.6 Displacement (red) and interaction force for drop/silica (dark green, light green) and drop/drop (blue, cyan) systems, as a function of time, in *n*-heptane. The time in brackets indicates exposure of 0° silica substrate to *n*-heptane prior to experiment (drop/silica) or prior to deposition of the bottom water drop onto the silica (drop/drop). For drop/drop experiments, the water drop was exposed to *n*-heptane for 17 minutes prior to experiment.

The typical volume that detached after drop/silica contact was ~2.4 μL (estimated from side-camera images using spherical cap formula). If this drop had fully spread on the 10 mm silica substrate, it would be expected to have a height of ~60 μm at the center (due to camera viewing limitations (~4.5 mm horizontal range) and difficulty discerning the top surface location of a spread-out drop, the true height of the drop could not be verified). With this assumption in mind,

both the blue and cyan force curves (drop/drop interactions) in Figure 5.6 would need to be shifted to the right by $t$ + 0.6 s ($D$ = 1540 μm at start to account for 60 μm less separation, at $V$ = 0.1 mm/s). In this case, for both *n*-heptane ageing times (23 and 17 minutes), the contact time between drop/silica would be faster than for equivalent drop/drop system: 12.770 s vs. 13.062 s for 23 minutes silica ageing, and 11.731 s vs. 12.481 s for 17 minutes silica ageing, respectively. Interestingly, both the magnitude of the force on contact and drop elongation was stronger for drop/silica interactions than it was for drop/drop interactions. For 23 minutes silica ageing time, there was 25.2% and 13.9% drop elongation for drop/silica and drop/drop interactions, respectively. For 17 minutes silica ageing time, there was 33.3% and 15.4% drop elongation for drop/silica and drop/drop interactions, respectively. This difference is partly related to some of the total system elongation occurring via the upward pinching of the bottom drop for drop/drop interactions. For the interaction force, the magnitude was approximately double for drop/silica interaction compared to drop/drop interaction: -36.4 μN vs. -13.1 μN for 23 minutes silica ageing, and -42.7 μN vs. -20.3 μN for 17 minutes silica ageing.

*5.3.1.3 Effect of pH*

The effect of pH was explored on the interaction force between two alkaline water droplets in water-saturated *n*-heptane for two different conditions: pH 9.7 and pH 12.2 (at $V$ = 0.1 mm/s). The bottom droplet was deposited after the detachment of an alkaline water drop during a drop/silica interaction. As discussed in the previous sub-section, the precise height of the bottom droplet in this experiment was not known; due to experimental limitations, a bubble could not be used to calibrate the location of the top of the bottom drop in this instance. The full interaction curves for pH 9.7 (blue) and pH 12.2 (cyan) are shown in Figure 5.7A, with the interaction force on drop/drop contact indicated on the curves using pink dots. In Figure 5.7B, alkaline drop/drop interactions (pH 9.7 – blue, pH 12.2 – cyan) are compared with alkaline drop/silica interactions (pH 9.7 – green, pH 12.2 – orange), where force at drop/silica contact and jump-in is shown using pink dot and yellow arrow, respectively. For image clarity in Figure 5.7B, jump-in for blue curve and drop/silica contact for orange curve are not indicated via arrow/dot: they are -36.5 μN at 17.037 s and -31.2 μN at 17.100 s, respectively. The displacement curve in Figure 5.7 is shown as a dotted red line to indicate it is accurate for drop/silica systems, but approximate for drop/drop interactions. The legend in Figure 5.7 shows silica and bottom water drop exposure (as

applicable) to *n*-heptane prior to experiment. Side-camera images of alkaline drop/drop interactions for pH 9.7 and pH 12.2 are shown in Figure 5.8. These figures are discussed in more detail in the following paragraphs.

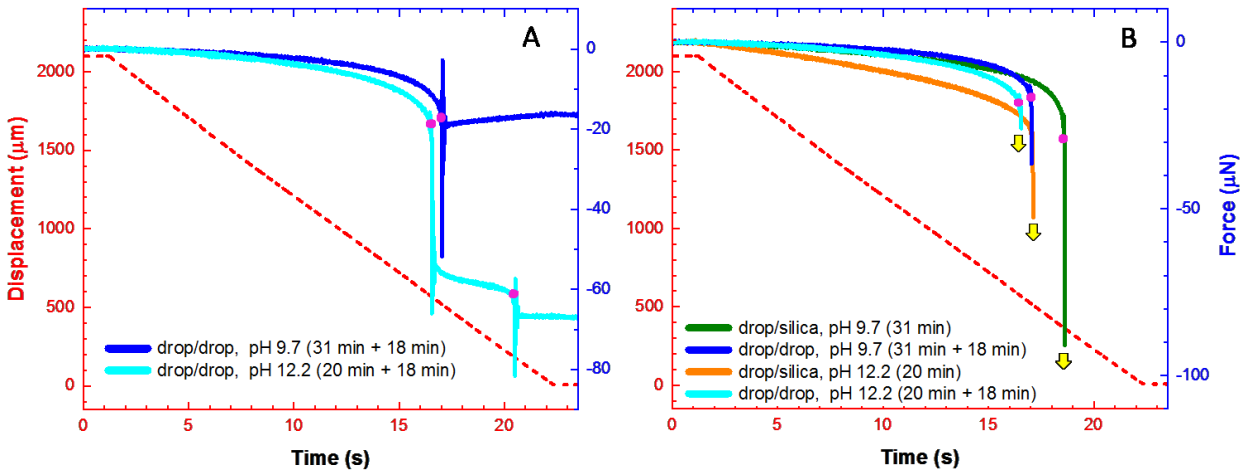


Figure 5.7 (A) Displacement (red) and interaction force (blue, cyan) as a function of time, for an alkaline water drop (blue – pH 9.7, cyan – pH 12.2) approached to an alkaline water drop deposited on 0° silica in *n*-heptane. (B) Comparison of the interaction force between alkaline drop/drop interaction (blue – pH 9.7, cyan – pH 12.2) and alkaline drop and 0° silica (green – pH 9.7, orange – pH 12.2), as a function of time; displacement shown in red. For all curves, drop/drop or drop/solid contact time (pink dot) and jump-in (yellow arrow) is indicated, and in the legend details (in brackets), the silica and bottom water drop exposure time to *n*-heptane, respectively.

For pH 9.7 with 31 minutes of silica exposure to *n*-heptane prior to experiment (blue curve in Figure 5.7), the bottom drop was exposed to *n*-heptane for 18 minutes prior to experiment and the top drop was generated fresh. Drop/drop contact was observed at $t$ = 17.027 s ($D$ = 518 µm, $F$ = -18.4 µN), followed by film rupture at $t$ = 17.028 s ($D$ = 518 µm, $F$ = -18.9 µN) and drop jump-in at $t$ = 17.037 s ($D$ = 517 µm, $F$ = -36.5 µN), for a drop jump-in time of 10 ms. At drop/drop contact, the top water drop elongated by 13.5% (194 µm), with a 3.4% decrease in drop width. Similar to previous drop/drop results, the bottom water drop also elongated, or

"pinched", upwards towards the top drop (precise elongation distance unknown). As discussed previously, due to the bottom water drop "pinching" upwards, film rupture and film lifetime could not be observed from the bottom camera. The side camera images of the alkaline drop are shown in Figure 5.8(a-e), with original drop at $t$ = 0 s and drop/drop contact at $t$ = 17.027 s shown in a and b, respectively. The evolution of the drop after film rupture is shown in Figure 5.8(c,d) for $t$ = 17.029 s and $t$ = 17.035 s, respectively, followed by top drop jump-in shown in Figure 5.8(e) ($t$ = 17.037 s).

For pH 12.2 with 20 minutes of silica exposure to *n*-heptane prior to experiment (cyan curve in Figure 5.7), the bottom drop was also exposed to *n*-heptane for 18 minutes prior to experiment and the top drop was generated fresh. There were two separate jump-ins observed for the same top drop during its descent, with the first being faster than the usual ~10 ms, and only partial (a small portion of the drop detached from the original drop). For the first drop/drop interaction, contact was observed at $t$ = 16.539 s ($D$ = 566 μm, $F$ = -19.9 μN), followed by film rupture at $t$ = 16.540 s ($D$ = 566 μm, $F$ = -20.2 μN) and drop jump-in at $t$ = 16.544 s ($D$ = 566 μm, $F$ = -25.8 μN), for a drop jump-in time of 5 ms. The volume detached from the top drop was ~0.35 μL (drop radius was reduced from 0.85 mm to 0.81 mm). For the second drop/drop interaction, contact was observed at $t$ = 20.483 s ($D$ = 178 μm, $F$ = -60.9 μN), followed by film rupture at $t$ = 20.484 s ($D$ = 178 μm, $F$ = -61.2 μN) and drop jump-in at $t$ = 20.494 s ($D$ = 177 μm, $F$ = -72.5 μN), for a drop jump-in time of 11 ms. As with pH 9.7 drop/drop interaction, for pH 12.2 the top alkaline water drop elongated downwards, while the bottom drop "pinched" upward. During the first jump-in, the top drop elongated by 22.5% (331 μm), with a 5.9% decrease in drop width, while during the second jump-in, the top drop elongated by 6.6% (94 μm), with a 0.9% decrease in drop width. The side camera images of the alkaline drop for the first drop interaction are shown in Figure 5.8(f-i), while the second drop interaction is shown in Figure 5.8(j-n). For the first drop interaction, the original drop at $t$ = 0 s and drop/drop contact at $t$ = 16.539 s are shown in Figure 5.8(f,g), followed by drop pinching at $t$ = 16.543 s in Figure 5.8(h) and detachment at $t$ = 16.544 s in Figure 5.8(i). The evolution of the drop shape at pH 12.2 was faster (5 ms) and involved only the bottom portion of the top drop, in comparison with pH 9.7, where the majority of the drop detached after 10 ms; this difference is easily visible when comparing Figure 5.8(h) and Figure 5.8(d). For the second drop interaction, the drop prior to

interaction and drop/drop contact is shown in Figure 5.8(j) and (k) for $t$ = 17 s and $t$ = 20.483 s, respectively. The evolution of the drop after film rupture is shown in Figure 5.8(l,m) for $t$ = 20.486 s and $t$ = 20.493 s, respectively, followed by top drop jump-in shown in Figure 5.8(n) ($t$ = 20.494 s).

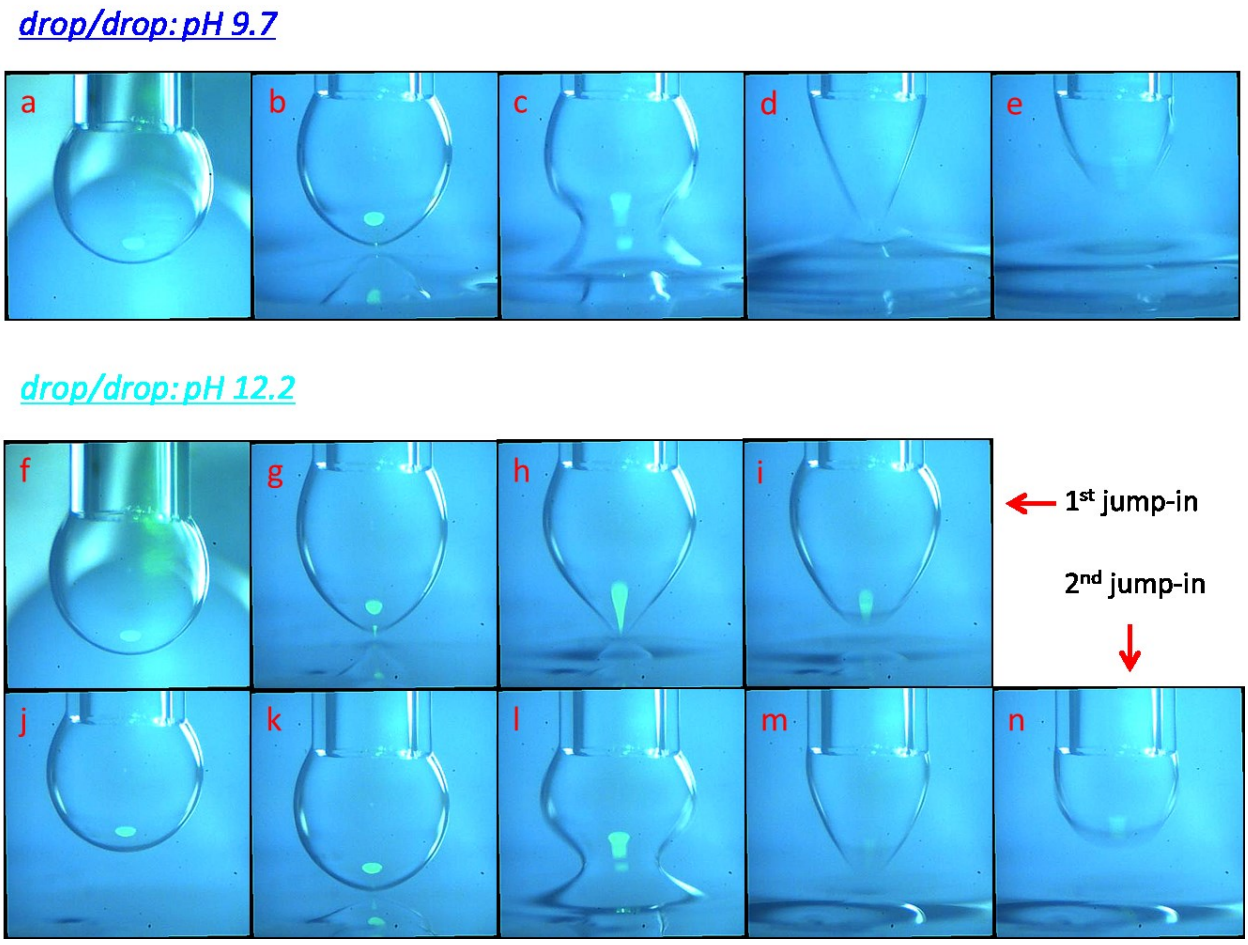


Figure 5.8 Side-camera images of drop/drop interactions in *n*-heptane for pH 9.7 (a-e) and pH 12.2 for first (f-i) and second (j-n) drop jump-in. Image time-stamps are listed alphabetically. pH 9.7 – 0 s, 17.027 s, 17.029 s, 17.035 s, 17.037 s; pH 12.2 – 0 s, 16.539 s, 16.543 s, 16.544 s, 17 s, 20.483 s, 20.486 s, 20.493 s, 20.494 s.

Similar to pure water drop discussed in the previous sub-section, the impact of silica ageing time in *n*-heptane on the strength of the interaction force is not as pronounced for the bottom alkaline water drop ageing in drop/drop experiments as it was for the silica substrate ageing in drop/silica

experiments in Chapter 4. This difference is illustrated in Figure 5.7B, where the drop/drop interactions shown in Figure 5.7A are paired with the equivalent force curves for the drop/silica systems, indicated in orange and green for 20 and 31 minutes *n*-heptane ageing time, respectively (as shown previously in Figure 4.17), with contact and jump-in shown with pink dot and yellow arrow, respectively. As mentioned in the previous section, the extent of spread of the bottom drop on the silica substrate is not known. Slower movement of three-phase contact line was observed for alkaline drop than for pure water drop on the silica surface, and it is possible that the bottom drop height was larger than ~60 μm (assuming partial drop spread). Shifting the drop/drop force curves in Figure 5.7 by $t$ + 0.6 s ($D$ = 1540 μm at start to account for 60 μm less separation, at $V$ = 0.1 mm/s) would result in slower contact time for pH 12.2 drop/drop than drop/silica (17.139 s vs. 17.100 s, respectively), but contact time difference for pH 9.7 drop/drop and drop/silica curve is more significant. For pH 9.7, shifting the force curve by $t$ + 1.6 s may be possible ($D$ = 1440 μm at start, drop spread of 7 mm on silica), but further work is required to understand the larger observed difference in contact time between drop/drop and drop/silica contact for pH 9.7 curves (blue and green in Figure 5.7). Both the magnitude of the force on contact and drop elongation were somewhat stronger for drop/silica interactions than for drop/drop interactions. For 31 minutes silica ageing time, there was 18.3% and 13.5% top drop elongation for drop/silica and drop/drop interactions, respectively. For 20 minutes silica ageing time, there was 28.1% and 22.5% (plus additional 6.6% at second jump-in) top drop elongation for drop/silica and drop/drop interactions, respectively. This difference between drop/silica and drop/drop elongation is partly related to some of the total elongation occurring via the upward pinching of the bottom drop for drop/drop interactions. Interestingly, the rate of the top drop elongation just prior to contact was significantly stronger for drop/drop systems than for drop/silica systems. In the case of pH 9.7 drop/drop system (31 minutes silica ageing), a thin tubule bridge formed between top and bottom drop for 1 ms prior to rupture that covered 105 μm. Assuming a symmetrical contribution (top drop elongation downward and bottom drop pinch upward), the top drop had elongated 52 μm in 1 ms. The same pH 9.7 system for drop/silica interaction saw 52 μm elongation occur over 4 ms prior to drop/silica contact. In the case of pH 12.2 drop/drop system (20 minutes silica ageing), the thin tubule bridge formed 1 ms prior to film rupture covered 126 μm. Similarly, assuming symmetrical contribution, the top drop elongated 63 μm and the equivalent elongation in drop/silica pH 12.2 system occurred over 4 ms

prior to drop/silica contact. For the interaction force, the magnitude was 1.6 times stronger for drop/silica interaction compared to drop/drop interaction: -30.3 μN vs. -18.4 μN for 31 minutes silica ageing, and -31.2 μN vs. -19.9 μN for 21 minutes silica ageing. Another interesting difference is the top drop jump-in time: while it was at the expected rate of a pure water drop or faster for alkaline drop/drop interaction (5 ms for pH 12.2 first jump-in, 10-11 ms for pH 9.7 and second pH 12.2 jump-in), in the case of drop/silica interaction, the jump-in time was markedly slower at the same silica solvent exposure conditions (33 ms and 26 ms for pH 9.7 and 12.2, respectively).

## 5.4 Discussion

From disjoining pressure calculations discussed previously (see Figure 3.3), the interaction between two water drops in *n*-heptane is expected to lead to film thinning ($\Pi < 0$) due to an attractive VdW force. While the interactions discussed in this chapter were indeed attractive and led to film thinning and rupture, the range of the observed attractive force extends far beyond the ~50 nm calculated in section 3.2.1, or the theoretical total range of the VdW force (~100 nm; 500 nm has been observed for zwitterionic surfaces[77]). Specifically, the drop/drop *n*-heptane interactions in this work had long-range attractive force with a range of 5 mm or more, including observed macroscopic effect of drop/drop vertical elongation toward each other prior to contact, followed by film rupture and drop coalescence.

The deformation and coalescence of water droplets has been observed in the presence of an electrical field. That is, the droplets would coalesce once the applied electrical field voltage was higher than a critical voltage in which the Maxwell or electrical stresses overcame the disjoining pressure.[116] Coalescing separated droplets requires that the Maxwell stress first deform droplets against the interfacial tension to promote drop contact, and then it must overcome the disjoining pressure for coalescence to occur.[116] Similar to the setup in Chapter 4, no external electrical field had been applied to the drop/*n*-heptane/drop system discussed here.

Shorter exposure time of the bottom water drop to *n*-heptane prior to drop/drop contact resulted in stronger attractive force and larger top drop elongation on drop/drop contact. Decreasing the bottom water drop *n*-heptane exposure time ("ageing") from 35 to 20 minutes resulted in

increased attractive force (-44.2 μN and -56.7 μN, respectively), increased top drop elongation (+17.2% and +21.5%, respectively), and decreased drop width (-5.6% and -6.9%, respectively), at drop/drop contact. In both cases, the bottom water drop "pinched" upward by at least 200 μm from its original vertical height (as calibrated by a bubble prior to experiment). This result is somewhat surprising, considering that the contact angle of a water drop deposited on a 0° silica disc prior to immersion in *n*-heptane had been shown to stay constant at ~0° even after 3 hours of solvent exposure. It is not clear why ageing the bottom water drop in solvent prior to experiment impacted the results, when for the water drop/silica system, ageing the top water drop in *n*-heptane (for 15 minutes) had negligible impact on the interaction force or drop elongation. Ageing of the top water drop was not addressed for drop/drop experiments (the top drop was always freshly generated), and more work should be done to compare the effect of top and bottom water drop ageing in *n*-heptane on the attractive force magnitude and drop elongation. The interaction (force magnitude, top drop elongation) for drop/drop system was significantly stronger than for drop/silica at 0.5 mm/s approach velocity (shown previously in Figure 4.19): -56.7 μN vs. -27.7 μN, and 21.5% vs. 9.7%, respectively. While the *n*-heptane ageing time was the same (20-21 minutes), the item exposed to *n*-heptane was different: silica substrate in the water/silica system, and the bottom water drop in the water/water system (the water drop was deposited on 0° silica substrate prior to submersion in *n*-heptane, for a silica exposure time of zero). For this reason, a direct comparison is not possible, but demonstrates the effect of increased drop elongation and attractive force on contact by reduced exposure of silica to *n*-heptane.

Similar to drop/silica interaction in *n*-heptane described in Chapter 4, drop/drop interaction in *n*-heptane showed a decrease in attractive force and top drop elongation with increasing silica exposure time to *n*-heptane. The exposure of the bottom drop to *n*-heptane was kept constant at 17-18 minutes (as discussed in the previous paragraph, this type of solvent exposure has an impact on the force magnitude and drop elongation) while the silica substrate exposure time to *n*-heptane prior to deposition of drop on it was varied. For pure water, decreasing silica *n*-heptane exposure from 23 to 17 minutes resulted in increased attractive force (-13.1 μN and 20.3 μN, respectively), increased the top drop elongation (+13.9% and +15.4%, respectively) and decreased the drop width (-3.8% and -4.3%, respectively), at drop/drop contact. For alkaline

drop, decreasing silica *n*-heptane exposure from 31 minutes (pH 9.7) to 20 minutes (pH 12.2) resulted in increased top drop elongation (+13.5% and +22.5%, respectively) and decreased drop width (-3.4% and -5.9%, respectively), at drop/drop contact. Cleaning silica with piranha generates vicinal hydroxyl groups on the silica surface, altering the contact angle of water on such a surface to ~0°. These hydroxyl groups can dissociate and become charged in an alkaline environment (typically pH 10-11).[113]

Comparing interactions between two pure water drops and between two alkaline drops, at low alkalinity (pH 9.7), similar drop elongation is observed as for pure water drops (13.9% vs. 13.5%), while at higher alkalinity (pH 12.2), a stronger top drop elongation was observed for alkaline drop than for pure water (22.5% vs. 15.4%, respectively), despite a shorter silica *n*-heptane exposure time for water than pH 12.2 drop (17 vs. 20 minutes). As discussed in Chapter 4, electrostatics is a possible mechanism for the large range (5 mm+) of attractive force observed here as it has a larger operating range than surface forces, but it is not clear how drop and silica surfaces become oppositely charged such that it would result in the observed long-range attractive force (see section 4.4). For a given electrostatic surface charge $q$ ($q = q_0 \cdot e^{-t/\rho\varepsilon}$), higher resistivity $\rho$ leads to a slower decay of the electrostatic charge $q$. From Table 4.4, the resistivity values of water, alkaline drop, *n*-heptane and silica are $1.82\times10^5$ Ω·m, 1-1.25 Ω·m, $10^{16}$ Ω·m and $10^{16}$ Ω·m, respectively. From this relation, higher resistivity should lead to a slower decay of electrostatic charge, giving rise to the observation of stronger long-range attractive force. However, despite a higher resistivity for water than for an alkaline drop ($1.82\times10^5$ vs. 1-1.25 Ω·m, respectively), at higher pH (12.2), a stronger elongation was observed for the alkaline drop than for pure water (22.5% vs. 15.4% for pH 12.2 and water, respectively). For higher pH (12.2) bottom drop, the dissociation of silica surface hydroxyl groups potentially contributes to the strengthening of observed electrostatic interaction, compared with pure water drop on a silica surface. Expanding the comparison, for the same *n*-heptane silica exposure time prior to experiment, the top drop elongation on contact for alkaline drop/silica interactions was stronger than for two alkaline drops interacting in *n*-heptane (pH 12.2 – 28.1% vs. 22.5%; pH 9.7 – 18.3% vs. 13.5%) as was the attractive force on contact (~30 μN for drop/silica versus ~19 μN for drop/drop). This trend is in line with electrostatics surface charge decay relation, as a bare silica surface has a larger resistivity value than a water drop ($10^{16}$ Ω·m vs. $1.82\times10^5$ Ω·m,

respectively). Given that the exposure to *n*-heptane for both bottom drop and silica surface affect the magnitude of the attractive force in drop/drop systems, and the total system elongation is composed of top and bottom drop contributions, direct comparison between drop/drop and drop/silica results is not straightforward.

There are major implications of an extra long-range attractive force between two water drops (Chapter 5) or water drop and hydrophilic solid (silica, mica – Chapter 4) on the behaviour of W/O emulsions. One could hypothesize that for very clean systems, water drops in high-resistivity solvents such as *n*-heptane would spontaneously attract each other over significant distances, with fast film rupture, coalescence and phase separation. Of course, clean W/O emulsion systems (no surface-active molecules or small particles at the interface) are inherently thermodynamically unstable (see Introduction), and it would be difficult to design an experiment to distinguish inherent phase separation from potential additional extra long-range attractive force-driven contributions. In the case of real-world emulsions such as W/O emulsions found in bitumen production, this mechanism would have limited applicability for improved demulsification as no extra long-range attractive force had been detected in contaminated systems.

## 5.5 Summary

The interaction force between two water drops (pure water, alkaline) in *n*-heptane was measured using the DFA. A long-range (5 mm+) attractive force was detected, with drop elongation observed at drop/drop contact. Both top and bottom drop deformed at close proximity prior to contact, with top drop elongating downwards and bottom drop "pinching" upwards, resulting in contact, film rupture and drop coalescence (top drop detachment from capillary). Larger drop elongation on drop/drop contact was accompanied by (a) a steeper attractive force curve during drop approach (b) larger attractive force at drop/drop contact and (c) decreased top drop width. The effect of silica solvent exposure time, bottom water drop solvent exposure time and drop pH on magnitude of attractive force and drop elongation at drop/drop contact was explored. Similar to water drop/silica system, increased exposure of silica surface to *n*-heptane prior to deposition of the bottom water drop reduced the magnitude of the attractive force at drop/drop contact as well as drop elongation. In addition, increased solvent exposure of the bottom water drop to

*n*-heptane also led to a decreased attractive force magnitude and top drop elongation at drop/drop contact. Contrary to drop/silica system, for drop/drop interactions, the top drop elongation at high pH (12.2) was stronger than the interaction between two pure water drops. The cause of the attractive long-range force is hypothesized to be a combination of electrostatics, dissociation of surface silica hydroxyl groups at high pH, and reduction of substrate hydrophilicity as a function of *n*-heptane exposure time prior to drop/drop contact. As with drop/silica system, no extra long-range attractive force or drop elongation was observed for drop/drop interactions in toluene.

# Chapter 6: Contaminated Organic Systems: Drainage Dynamics of Thin Liquid Films between Water and Silica

## 6.1 Introduction

Properties of thin liquid films between approaching droplets are a critical factor for emulsion stability. The Dynamic Force Apparatus (DFA) - simultaneous measurement of interfacial film thickness, drainage time and interaction forces at precisely controlled approach velocities - was used to study the interactions of a water drop with solid surfaces in organic liquid containing a surface active polyaromatic compound C5PeC11. A water droplet in toluene containing 0.1 g/L C5PeC11 was driven toward a silica surface of varying wettability (contact angles of 0° and 107°) at two different droplet approach velocities (0.1, 1 mm/s) and temperatures (22°C, 40°C). The experimentally determined dynamics of the thin liquid film drainage were modelled successfully using the Stokes-Reynolds-Young-Laplace (SRYL) theoretical model. The velocities chosen (0.1, 1 mm/s) correspond to Reynolds numbers of 0.25 and 2.5, respectively, at room temperature. As discussed previously, this is significantly higher than what is available for studies using AFM. We have chosen to study the interaction between water droplet and silica surface to model W/O emulsions stabilized by model asphaltene compound C5PeC11 as it is difficult to obtain clear interference fringes between two droplets, especially for this system where contrast (difference in refractive indices) is small. The impact of temperature for the interaction of a water drop with solid surfaces in the presence of C5PeC11 in toluene is, for the first time, studied with the DFA in a well-controlled temperature setup.

## 6.2 Results and Discussion

Table 6.1 and Table 6.2 show the experimental parameters of the system, along with the input values used for theoretical modelling. The size of the droplet was maintained by pixel diameter comparison between capillary and droplet from the side camera video feed. The outer diameter of the capillary was verified with a caliper to be 1.30 ± 0.01 mm and the angle that the droplet makes with the capillary is 136 ± 3°. C5PeC11 concentration of 0.1 g/L, or 0.121 mM, was chosen in this work because it is below the CMC (critical micelle concentration)[117] in order to

Table 6.1 Summary of relevant system properties, measured or from literature

| Property | Substance | $T = 22°C$ | $T = 40°C$ |
|---|---|---|---|
| Viscosity $\mu$ (mPa·s) | water | 1.002 | 0.653 |
| | toluene | 0.590 | 0.458 |
| | C5PeC11 (0.1 g/L in toluene) | 0.590 | 0.458 |
| Interfacial Tension $\gamma$ (mN/m) | toluene[91] | 36.5 | 34.7 |
| | C5PeC11 (0.1 g/L in toluene) | 27.5 | 26.5 |
| Refractive Index $n$ | fused silica | 1.458 | |
| | water[93] | 1.334 | |
| | C5PeC11 (0.1 g/L in toluene) | 1.499 | |

Table 6.2 Experimental and theoretical parameters of the droplet-silica system

| Physical Parameter | Experiment | Theory |
|---|---|---|
| Water droplet radius, $R$ | 0.85 ± 0.01 mm | 0.85 mm |
| Initial separation, $h_0$ | 500 ± 10 μm | 490-510 μm |
| Maximum displacement, $\Delta X$ | 600 ± 10 μm | 600 μm |

avoid the formation of micelles and aggregates in solution, but large enough to provide considerable changes in behaviour. While CMC depends strongly on solvent (Zhen *et al.*[117] used xylene), interfacial tension measurements with C5PeC11 at pH 7 in xylene[117] and in toluene[50] yielded similar values, indicating 0.1 g/L C5PeC11 falls below CMC for both toluene and xylene solutions. In addition, rheology contributions are minimized due to low observed apparent dilatational elastic/viscous moduli[50] above 0.05 mM C5PeC11. Interfacial tension measurements were performed for 0.1 g/L C5PeC11 in toluene solution at $T = 22°C$ and $T = 40°C$, as shown in Table 6.1. The adsorption of C5PeC11(molar mass 827.12 g/mol) onto the water droplet surface

was fast (over the course of seconds) and after this time the interfacial tension remained constant. Values for pure toluene, shown in Table 6.1, were measured experimentally and matched those expected from the literature,[91] and are shown for reference to C5PeC11 system.

The experimental displacement and velocity curves of the water droplet approaching a silica substrate are shown in Figure 6.1. Displacement curves are shown in Figure 6.1(a,c) and the corresponding real-time velocity curves are shown in Figure 6.1(b,d). The motorized actuator controlled the entire vertical trajectory of the water droplet, including acceleration/deceleration, but only the droplet approach is shown in Figure 6.1. The displacement signal was measured by a displacement sensor, and the real-time velocity was obtained by smoothing (fifth–order Savitzky–Golay function[95]) and differentiating the displacement curve. The droplet was driven toward the surface after a short hold period at $t$ = 1 s.

The total separation between the bottom of the water droplet and the top of the silica substrate was set at 500 μm. In our experiments, we kept the overlap between the droplet and silica surface at 100 μm, which results in a total displacement of 600 μm, as shown in Figure 6.1(a,c). To ascertain the exact point of contact between the droplet and the silica surface, some air was aspirated into the capillary below the water to generate a bubble of the same height as the water droplet. Each experimental setup is slightly different (capillary length variations, placement of cell on microscope stage, etc.) and the bubble is approached to the surface until contact is just visible on the inverted microscope, with water droplet experiments started at 500 μm above this point. For the case of 1 mm/s in Figure 6.1(b), the droplet was moving at 1 mm/s for 0.32 s, with the remainder of the time spent accelerating from rest (1-1.36 s) and decelerating back to 0 mm/s (1.68-2.15 s), with the hold (stationary) period beginning at 2.15 s. For the case of 0.1 mm/s in Figure 6.1(d), the lower speed meant it took much longer to travel the same 600 μm and the droplet spent most of its time at 0.1 mm/s (1.28-7.07), with about 0.3 s spent accelerating to 0.1 mm/s and back to rest. The holding period began at 7.3 s. After a given stationary holding period (10 s for hydrophilic silica and 50 s for hydrophobic silica) the droplet withdrawal followed the same trajectory but upwards. At 1 mm/s, the droplet was retracted at 12.3 s or 52.3 s (hydrophilic or hydrophobic, respectively) and at 0.1 mm/s, at 17.3 s or 57.3 s (hydrophilic or hydrophobic, respectively). With the same travel time for 600 μm as before (1.15 s for 1 mm/s and 6.4 s for 0.1

mm/s), the droplet was fully retracted at 13.3 s or 53.3 s at 1 mm/s (hydrophilic or hydrophobic, respectively) and 23.7 s or 63.7 s at 0.1 mm/s (hydrophilic or hydrophobic, respectively).

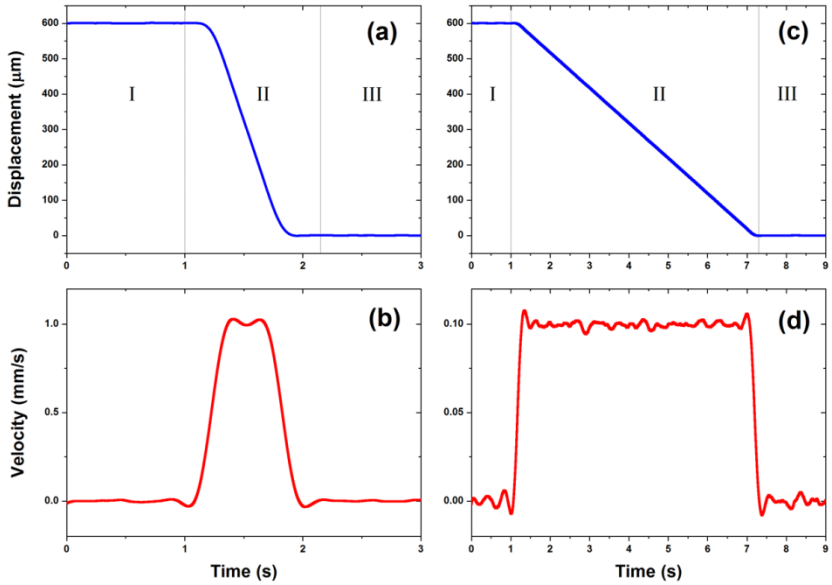


Figure 6.1 Displacement and real-time velocity of the droplet approaching a silica surface, controlled by a motorized actuator. Actual displacement of water droplet and corresponding velocity for a set drive velocity of droplet at 1 mm/s are shown in (a) and (b), respectively, and displacement and velocity for 0.1 mm/s are shown in (c) and (d), respectively. Hold, Drive and Hold periods are indicated by I, II and III, respectively, as shown in (a) and (c).

For the case of a water droplet immersed in an organic continuous phase (0.1 g/L C5PeC11 in toluene), Π is composed of the sum of Van der Waals interaction $\Pi_{vdW}$, hydrophobic force $\Pi_h$ and steric repulsion $\Pi_s$ (electric double layer interaction is notably absent due to negligible concentration of free charge carriers in non-polar media such as toluene[118]). With a pKa[117] of approximately 6, about half of the carboxylic acid groups on C5PeC11 at the toluene/water interface are expected to be deprotonated and charged (the pH of Milli-Q water can be as low as 5.5 due to carbon dioxide solubilization). These charged carboxylic acid groups reside inside the water drop[50] while the pyrene core and aliphatic tails are immersed in toluene. Since electric double layer is absent in toluene due to its low dielectric permittivity, charge-related phenomena are not relevant for thin film drainage in this system, with interactions between the water drop

and silica surfaces governed by Van der Waals and steric forces. Van der Waals contribution is negligible beyond 100 nm separation, with hydrophobic and steric repulsion becoming significant at even smaller separations (though the precise nature and range of hydrophobic interaction is still under debate[119]).

The temperature conditions tested were room temperature ($T$ = 22°C) and 40°C. The upper temperature of 40°C was chosen due to the limitation of bimorph operability (adhesive holding piezoelectric slabs in place inside bimorph is not rated for operation above 40°C), while ideally the temperature of interest for industrial froth treatment operations is significantly higher (80°C). Two wettability conditions were tested for silica, with contact angles (water in air) ~0° and 107°. For simplicity, in further discussions ~0° silica will be referred to as hydrophilic silica and 107° silica will be referred to as hydrophobic silica. Finally, two approach velocities (1 and 0.1 mm/s) were tested to evaluate higher Reynolds number conditions. Spatiotemporal interfacial thin film drainage profiles for 0.1 g/L C5PeC11 toluene solution have been grouped by temperature, with $T$ = 22°C and $T$ = 40°C shown in Figure 6.2 and Figure 6.3, respectively. As the water droplet is driven toward the silica surface, once the hydrodynamic pressure becomes larger than the internal pressure of the water droplet, the curvature of the droplet surface inverts to become locally concave, resulting in dimple formation.[120] Such dimples were observed in all C5PeC11 experiments, similar to previous studies,[95] in which the thickness at the barrier rim becomes thinner than at the center. The film drainage depends on viscosity, while the water drop deformation depends on pressure and surface tension. Temporal film thicknesses at the barrier rim ($r_{rim}$)) and center of the film ($r$ = 0) are shown in Figure 6.4(a-c), with corresponding force curves indicated in Figure 6.4(d-f). The differences of velocity, wettability and temperature are described in the next subsections.

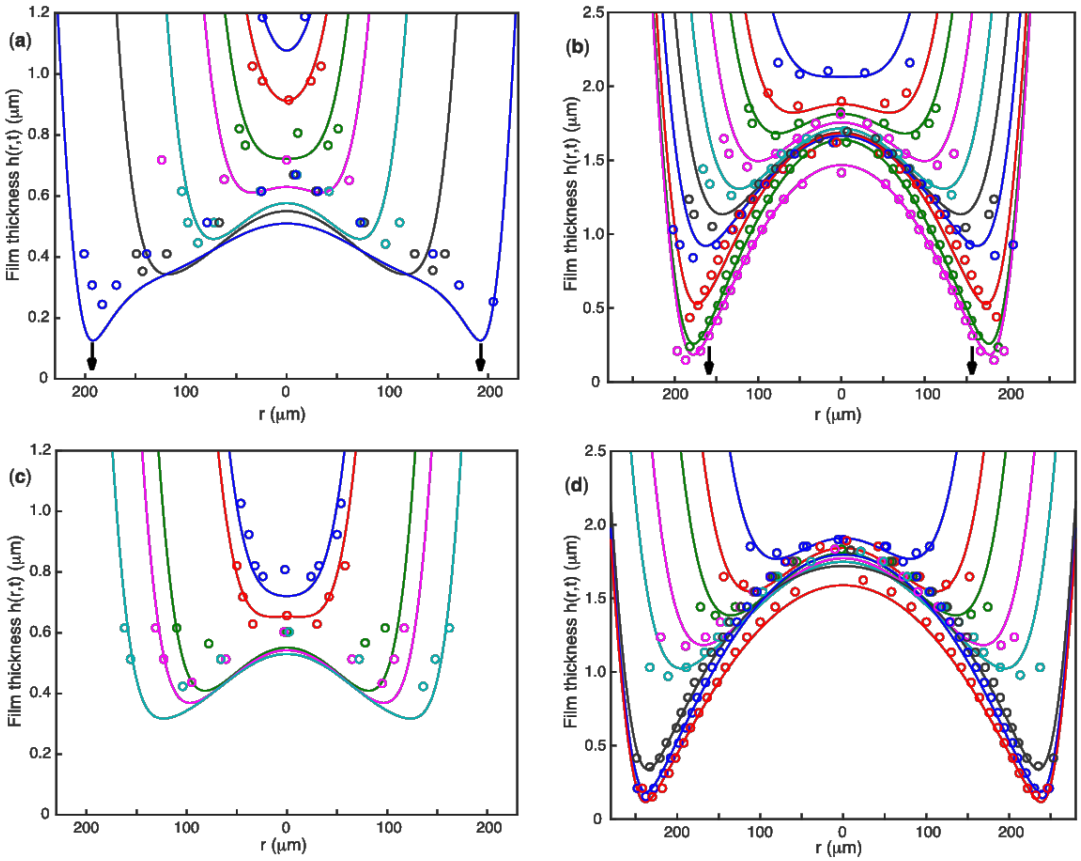


Figure 6.2 Spatiotemporal interfacial thin film profiles for 0.1 g/L C5PeC11 solution at 22°C for: (a) $V = 0.1$ mm/s, 0° silica; (b) $V = 1$ mm/s, 0° silica; (c) $V = 0.1$ mm/s, 107° silica and (d) $V = 1$ mm/s, 107° silica. Open circles represent experimentally measured profiles with the solid lines corresponding to SRYL model prediction, where arrows indicate film rupture (0.240 μm and 0.150 μm for (a,b), respectively). Time (as defined in Figure 6.1) progresses downward in each image as follows: (a) $t$ = 6.338, 6.356, 6.400, 6.468, 6.652, 7.000, 8.564 s; (b) $t$ = 1.776, 1.794, 1.806, 1.826, 1.852, 1.882, 1.924, 2.100, 3.100, 5.330 s; (c) t = 6.400, 6.432, 6.728, 6.840, 7.072, 8.400, 12.800 s and (d) $t$ = 1.752, 1.776, 1.800, 1.840, 1.880, 2.384 3.944, 14.920 s.

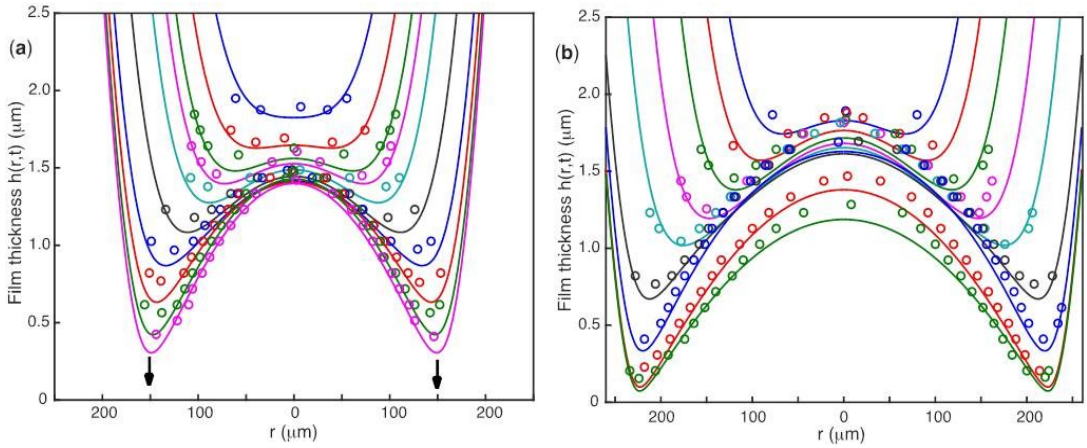


Figure 6.3 Spatiotemporal interfacial thin film drainage profiles for 0.1 g/L C5PeC11 solution at 40°C for: (a) $V$ = 1 mm/s, 0° silica; (b) $V$ = 1 mm/s, 107° silica. Open circles represent experimentally measured profiles with the solid lines corresponding to SRYL model prediction, where arrows indicate film rupture (a: 0.420 μm). Time (as defined in Figure 6.1) progresses downward in each image as follows: (a) $t$ = 1.788, 1.806, 1.816, 1.824, 1.838, 1.866, 1.906, 1.968, 2.130, 2.418 s; (b) $t$ = 1.744, 1.760, 1.784, 1.816, 1.856, 1.952, 2.320, 19.680, 43.456 s.

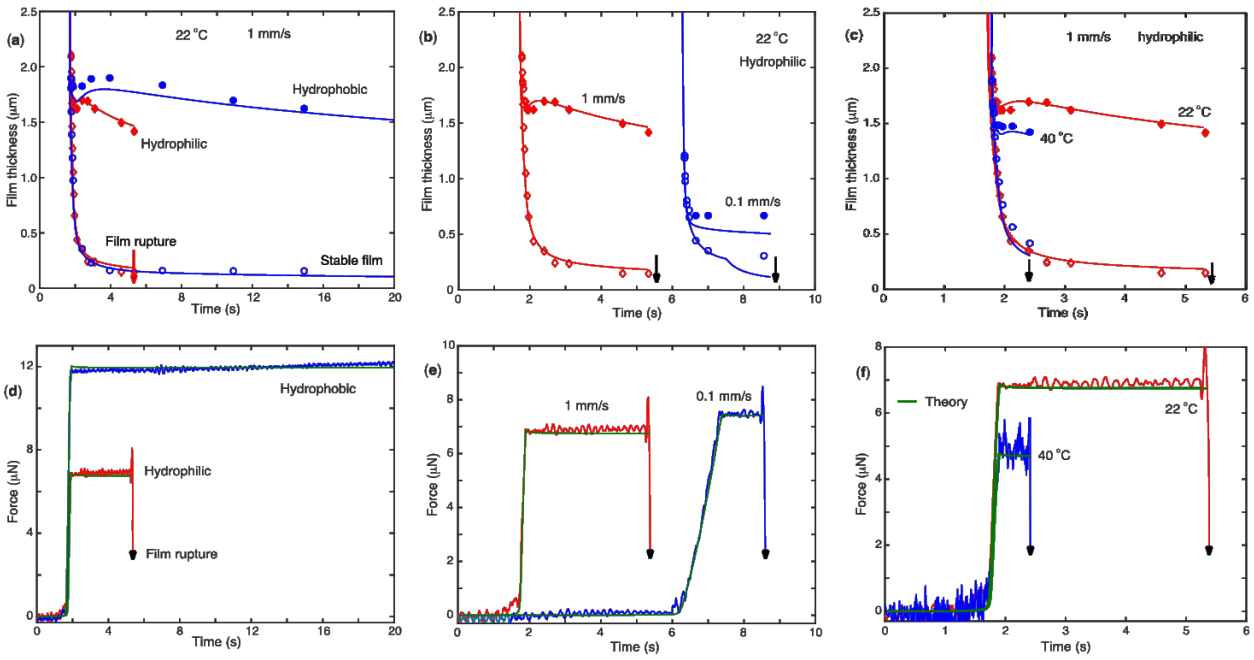


Figure 6.4 Film thickness at the center $h(0,t)$ and at the barrier rim $h(r_{rim},t)$ (a-c): symbols for experimental results and solid lines for corresponding theoretical predictions (filled symbols for $h(0,t)$ and open symbol for $h(r_{rim},t)$); and corresponding force curves (d-f): red/blue for experimental data and green for theoretical prediction as a function of time, with (a,d) showing the effect of wettability at 22°C for $V$ = 1 mm/s, (b,e) showing the effect of approach velocity for hydrophilic silica at 22°C, and (c,f) showing the effect of temperature for hydrophilic silica at $V$ = 1 mm/s.

### *6.2.1 Effect of approach velocity*

In Figure 6.2 and Figure 6.3, the film profiles move downward as a function of time, with the exact times of each profile outlined in the captions of these figures. Experimental measurements and SRYL model predictions are indicated with open symbols and solid lines, respectively. In the case of hydrophilic silica (Figure 6.2a,b and Figure 6.3a), film rupture for the latest film profile is indicated by downward arrows. From Figure 6.2 and Figure 6.3, the theoretical curves agree with the experimental data quite well, with better matching observed for 1 mm/s versus 0.1 mm/s. The reason for this is fewer interference fringes at lower approach velocities (smaller dimple), with higher signal noise in a system with similar refractive indices (low contrast) as compared to the commonly studied bubble/solid interaction. At larger approach velocities, there are more interference fringes, resulting in more accurate experimental data and better agreement with theory. Fewer interference fringes available at lower approach velocities (smaller dimple), as well as higher signal noise in a system with similar refractive indices (low contrast) as compared to the commonly studied bubble/solid interaction, results in a less favorable match between theory and experiment. A larger and more pronounced dimple formed at higher velocities (1 mm/s versus 0.1 mm/s). For example, at $T$ = 22°C (Figure 6.2), the initial dimple formed at 1.7-1.8 μm for 1 mm/s and significantly lower at 0.5-0.6 μm for 0.1 mm/s, depending on silica wettability. Film thickness as a function of velocity is most easily seen from Figure 6.4(b), where the interfacial film height $h$ is plotted as a function of the droplet center ($h(0,t)$; top curves) and droplet rim ($h(r_{rim},t)$; bottom curves) for $V$ = 1 mm/s (red) and 0.1 mm/s (blue) for water droplet interacting with hydrophilic silica at $T$ = 22°C. Experimental data is shown with open symbols, while theoretical modelling is given as solid lines in the corresponding color, with film rupture indicated using downward arrows. Larger dimple formation leads to longer lifetime, where film lifetime (defined as the time between first interference fringe observation and rupture of the film) shown in Figure 6.4(b) is 3.60 s at $V$ = 1 mm/s versus 2.26 s at $V$ = 0.1 mm/s. Corresponding force curves for each case are shown in Figure 6.4(e), where the theoretical results (green lines) show excellent agreement with experimental data (1 mm/s and 0.1 mm/s results shown in red and blue, respectively). In our work, film rupture occurs at separations greater than 100 nm, well beyond the range of surface forces for this system. This was also observed in other systems where solid surfaces are present.[95,96] The reason for film rupture at

large thicknesses beyond the range of surface force is speculated to be caused by surface roughness or the presence of minor contaminants.

For the hydrophobic case, quantitative effects of velocity are more difficult to elucidate because as the film continues to drain, at some point the interference fringes become asymmetrical and can no longer be processed. Figure 6.2(c,d) and Figure 6.3(b) show interfacial thin film drainage results and modeling for 0.1 mm/s at $T$ = 22°C, 1 mm/s at $T$ = 22°C and 1 mm/s at $T$ = 40°C, respectively. The last film profile that reflects interference fringe symmetry was not the last observed interference fringe; the interfacial film continued to drain asymmetrically and film rupture was observed. The exact point in time when film rupture occurred was difficult to identify, as the three-phase contact line did not expand (contact area between the water drop and the silica surface remained constant during the hold period), as observed from the constant contact radius of the drop. Minor local attachment occurred for hydrophobic surfaces, as evidenced by a constant interaction force observed over the duration of the drop hold period. This local attachment was weak in strength, and the water drop readily detached from the silica surface upon withdrawal, with an adhesive force observed because of the receding contact angle.

### *6.2.2 Effect of solid wettability*

In the case of hydrophilic silica, film rupture is readily observed at both approach velocities and temperatures tested. Figure 6.4(a) shows the effect of wettability for $V$ = 1 mm/s at 22°C, where hydrophobic silica is shown in blue, and hydrophilic silica in red. For hydrophilic silica, film rupture occurred at $t$ = 5.37 s, whereas for hydrophobic silica, the film continued to drain for the duration of the hold period. Minor local attachment occurred for hydrophobic surfaces, but was insufficient to cause strong attachment of the drop. Figure 6.4(d) shows the corresponding force curves, with good agreement with the theoretical model, as shown in green. As discussed previously, in some cases it is difficult to evaluate the film evolution and equilibrium thickness for hydrophobic silica due to asymmetrical drainage of the film over time, as illustrated in Figure 6.5. Here, interference fringes and corresponding side camera images for $T$ = 22°C and approach velocity of 1 mm/s are compared for hydrophobic (i-iv) and hydrophilic (v-vi) silica. For hydrophobic silica, Figure 6.5(i) shows the water drop approaching silica surface at $t$ = 2.080 s, followed by a 50 s hold, as shown in Figure 6.5(ii) at $t$ = 25 s (part of the hold period). It is clear

that at $t$ = 25 s, the film had not finished draining but the remaining interference fringes were no longer symmetrical and could not be processed to generate film profiles. During withdrawal, the water droplet remained attached to the silica surface due to rupture of the film, with full droplet elongation before detachment reached at $t$ = 53.2 s (Figure 6.5(iii)), followed by droplet detachment from silica surface at $t$ = 54.0 s (Figure 6.5(iv)). For the hydrophilic case, a typical symmetrical interference fringe is shown in Figure 6.5(v) at the contact time between water droplet and silica surface at $t$ = 1.95 s (Figure 6.5(v)). After film rupture occurred at 5.37 s, the droplet formed a three-phase contact line and remained attached to the silica surface even after withdrawal at 15 s, as shown in Figure 6.5(vi). The dark spot on the right side of Newton fringes in Figure 6.5(v-vi) is a dirt or small defect on the objective lens and does not affect the interfacial thin film drainage.

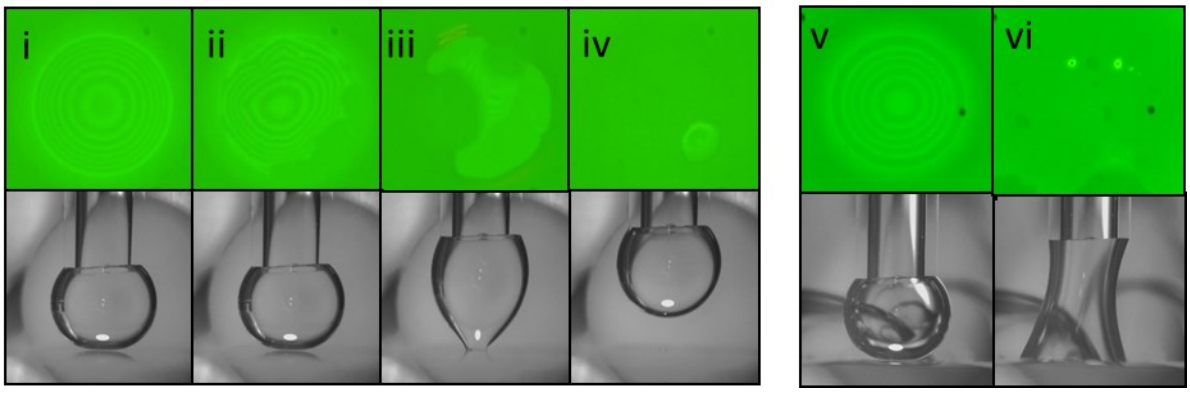


Figure 6.5 Newton fringes (top row) with corresponding side camera image (bottom row) for 22°C and $V$ = 1 mm/s; (i-iv) for hydrophobic and (v-vi) for hydrophilic silica. Time stamps of the images are as follows: (i) in contact at 2.1 s, (ii) holding at 25 s, (iii) detaching at 53 s, (iv) detached at 54 s, (v) contact at 1.9 s and (vi) capillary fully retracted at 15 s.

### *6.2.3 Effect of temperature*

The effect of temperature was investigated for a water droplet interacting with silica in 0.1 g/L C5PeC11-in-toluene system. An interesting observation for this C5PeC11 system is a marked decrease in film lifetime with increasing temperature for the hydrophilic case. For example, at 1 mm/s the film lifetime decreased from 3.60 s at $T$ = 22°C to 0.64 s at $T$ = 40°C. This is shown

clearly in Figure 6.4(c,f), where $T$ = 22°C is shown in red (film rupture at $t$ = 5.37 s) and $T$ = 40°C is shown in blue (film rupture at $t$ = 2.42 s). At $T$ = 22°C, the water droplet remained attached to the silica surface (Figure 6.5(vi)) while at $T$ = 40°C, the water droplet detached from the capillary upon full withdrawal of the capillary. Our results have captured the trend of faster film rupture time with increased temperature from the conditions tested (22°C and 40°C), and we would expect the rupture time to be further enhanced (reduced) at higher temperatures such as 80°C. Reduced viscosity at higher temperatures is one of the contributing factors for faster thin film drainage. A shorter film lifetime at higher temperatures has important implications for industrial applications in oil sands extraction, where the goal of froth treatment is to remove emulsified water droplets from bitumen product stabilized by surface-active specifies, such as asphaltenes. In froth treatment, increasing temperature has the beneficial effect of increased water droplet terminal settling velocities in diluted bitumen as approximated by Stokes' Law (decreased viscosity of diluted bitumen and decreased density difference between water and diluted bitumen). Our results help explain the beneficial effect of temperature in this industrial process from a new perspective: faster interfacial thin film rupture between emulsified water droplets at higher temperatures, leading to coalescence and improved water droplet settling behaviour. We demonstrate a direct link between our C5PeC11 work and observed water-in-oil emulsion behaviour on the industrial scale, establishing that (a) asphaltene model compounds are valid representatives of observed petroleum emulsion behaviour and (b) DFA is well-positioned for the study and modelling of emulsions on the industrial scale, including for other industries such as food and pharmaceuticals.

Finally, for the case of hydrophobic silica, at 0.1 mm/s approach velocity, a similar force of adhesion $F_{adh}$ was measured on detachment at both $T$ = 22°C and $T$ = 40°C, at $F_{adh}$ = 27.0 ± 0.5 μN. For the case of 1 mm/s approaching velocity, $F_{adh}$ = 24.0 ± 2.5 μN at $T$ = 22°C, but a smaller value at $T$ = 40°C of $F_{adh}$ = 10.5 ± 5.5 μN. Interestingly, the expected decrease in adhesion force with temperature is dependent on droplet approach velocity, with no change observed at 0.1 mm/s. This is likely related to larger dimple formation and slower interfacial film drainage at higher velocities, with more prominent interaction between C5PeC11 adsorbed on the droplet interface and silica surface (potential nanoaggregates) than between free C5PeC11 in

toluene and silica surface. More work needs to be done to understand the mechanism for this observation more clearly.

In conclusion, the main findings of our experimental and theoretical observations are:

(A) C5PeC11 is a model asphaltene compound that has been successfully used to model behaviour of petroleum W/O emulsions.

(B) Faster approach velocity of water drop results in larger deformation and longer drainage times for the interfacial thin film.

(C) At higher temperature, film drainage and attachment are faster due to lower viscosity and surface tension. This is in line with observed decrease in stability at higher temperatures for industrial petroleum W/O emulsions.

(D) Attachment of water drop is faster and stronger at hydrophilic surfaces, with slower organic thin film drainage and weak drop attachment observed at hydrophobic surfaces.

## 6.3 Summary

In this chapter, the fundamental behaviour of thin organic liquid films containing model asphaltene compound C5PeC11 between a silica substrate and water droplets was elucidated by using a temperature-controlled cell. In 0.1 g/L C5PeC11/toluene solution, the observed spatiotemporal thin film drainage dynamics and interaction force agreed well with the prediction of SRYL theoretical model. A bigger dimple formation and longer film lifetime were observed at higher droplet approach velocity (1 mm/s versus 0.1 mm/s). The wettability of silica surface was shown to have a significant impact. The film ruptured quickly in the hydrophilic case with strong droplet attachment, while localized, weak attachment was observed in the hydrophobic case. At 1 mm/s approach velocity, an increase in temperature from 22°C to 40°C led to a faster film rupture for fully water-wettable silica. This finding agrees with observations of more rapid oil/water phase separation at higher temperatures in petroleum emulsion systems and provides

justification for using C5PeC11 as a model compound to understand asphaltene behaviour in water-in-oil emulsions.

# Chapter 7: Conclusion and Future Work

## 7.1 Conclusions

Emulsions (dispersion of one liquid in another immiscible liquid; typically water and oil) play an important role in many processes, including foods, pharmaceuticals, agricultural formulations and petroleum processing. While aqueous systems have been studied extensively, droplet interactions and surface forces in non-polar, organic systems have garnered less research attention. In bitumen extraction from oil sands, W/O (water-in-oil) emulsions are encountered in froth treatment, where up to 3 wt% of water in diluted bitumen froth is in the form of kinetically stable W/O emulsions. These emulsions are difficult to remove, and the ions in the emulsified water can lead to downstream corrosion and fouling. Asphaltenes, a solubility class composed of some of the most polar and surface active species found in bitumen, are believed to be in large part responsible for the observed stability of petroleum W/O emulsions. Despite many studies regarding the role of asphaltenes in stabilizing W/O emulsions, gaps remained in understanding the fundamental mechanism behind their interfacial behaviour.

Both surfactants and solids can stabilize emulsions, and the properties and drainage of thin liquid films between approaching emulsified droplets or between droplet and solid surface are a critical factor in determining emulsion stability. That is, an unstable film will lead to rupture and drop/drop coalescence or formation of a three-phase contact line for drop/solid, while no coalescence or attachment will be observed in the case of a stable interfacial thin film. Improved understanding of thin film drainage dynamics and interaction forces for both clean (pure) and contaminated (contain surface-active emulsion stabilizers) organic systems is required to advance fundamentals of emulsion behaviour for various industrial applications, especially for froth treatment in bitumen extraction. In this thesis, the interfacial thin film drainage dynamics and interfacial forces were quantified for various water drop/solid and water drop/water drop organic systems, including “clean systems” (toluene, *n*-heptane) and “contaminated” systems that contain the asphaltene model compound C5PeC11.

The Dynamic Force Apparatus (DFA) was used for measurements, as it can capture information regarding interaction forces, spatiotemporal film thickness, drainage time and macroscopic drop

profile in one experiment, using a temperature-controlled cell. A water droplet was generated using a capillary via a gastight syringe, and moved down vertically toward a solid surface (silica, mica, sapphire) or another water droplet (deposited on silica) in an organic solvent (toluene, *n*-heptane). Precisely controlled droplet approach velocities (0.01 mm/s - 1 mm/s) probed a range of hydrodynamic conditions, with higher Reynolds numbers accessible than in AFM or SFA studies. Thin film profiles obtained from processed interference Newton fringes were complemented with theoretical modeling using the Stokes-Reynolds-Young-Laplace (SRYL) model.

In conclusion, the major contributions of this work are:

1. Observation and characterization of a novel long-range attractive force in "clean" *n*-heptane system for water drop/substrate and water drop/water drop interactions, with up to a 5 mm+ force range that cannot be described with current DLVO theory. Long-range attractive force resulted in progressive drop elongation toward the substrate or bottom water drop, as well as upward "pinching" of the bottom drop in drop/drop systems, with decreasing drop/substrate or drop/drop separation on approach.
2. Generally, larger drop elongation on drop/substrate or drop/drop contact was accompanied by: (a) a steeper attractive force curve during drop approach, (b) larger attractive force on contact, and (c) decreased drop width on contact. The majority of drop elongation (up to 60%) occurred close to silica substrate/bottom drop (within 50 ms of contact).
3. The range of the attractive force is: (a) at least 5 mm at short silica ageing time in *n*-heptane, and (b) disappears after a long (~1.5-2 hours) silica ageing time in *n*-heptane. No clear cause for this long-range hydrophilic attractive force could be identified, with electrostatics and decreasing substrate hydrophilicity with exposure time in *n*-heptane (increasing contact angle of water deposited on solid with longer *n*-heptane immersion) hypothesized as key contributing factors.
4. For drop/solid interactions, the effect of several variables on attractive force and drop elongation was explored: drop and solid ageing in *n*-heptane, *n*-heptane type (pure or water saturated), solid type (0° silica, 0° mica), water drop content (pure, 0.1 M KCl,

alkaline), surface roughness and approach velocity. Strongest drop elongation (33% of original height) was observed for a water drop and 0° silica interacting in water-saturated *n*-heptane at 0.1 mm/s approach velocity and low silica ageing time in *n*-heptane prior to drop/silica contact. Ageing of the water drop in *n*-heptane (up to 15 minutes) did not have a significant impact. Decreased drop elongation and weaker attractive force at drop/solid contact was observed with water drop content modification (0.1 M KCl, pH = 9.7, 12.2), increased solid ageing in *n*-heptane, increased approach velocity, and for mica.

5. For drop/drop interactions, decreasing attractive force and top drop elongation were observed with increased drop exposure to *n*-heptane and increased silica exposure (prior to bottom drop deposition) to *n*-heptane. At pH 12.2, drop elongation for alkaline drops was stronger than for pure drops; this may be related to dissociation of surface silica hydroxyl groups at high pH.
6. No long-range attractive force was observed between 0° sapphire and water in *n*-heptane, hypothesized to be due to the fast reduction in observed level of hydrophilicity of sapphire once submerged in *n*-heptane. It was established that no long-range attractive force was observed between a water drop and 0° silica or water drop/water drop in toluene. For non-hydrophilic substrates (60° sapphire, 107° silica) in *n*-heptane, a larger dimple was observed at higher water drop approach velocities, with good agreement between experiment and SRYL modeling at 1 mm/s and 0.1 mm/s approach velocities.
7. Improved understanding of thin film drainage was achieved in "contaminated" organic system, between a water drop and silica surface in a 0.1 g/L C5PeC11-in-toluene solution. The effect of velocity (0.1, 1 mm/s), surface wettability (0°, 107°) and temperature (22°C, 40°C) on film drainage dynamics was quantified, with results in good agreement with the SRYL theoretical model. Higher approach velocity of water droplet resulted in larger dimple formation and longer film lifetime. Rupture of thin films was observed in all cases, with strong attachment and moving three phase contact line in hydrophilic case. Finally, faster film rupture was observed at higher temperatures, in line with industrially observed improvements in removal of water-in-oil emulsions at higher temperatures during froth treatment in bitumen extraction.

## 7.2 Recommendation for Future Work

For “clean” drop/solid and drop/drop systems:

- Establish the full range of extra long-range attractive force. Current setup (displacement sensor range and visibility of drop inside the cell) had limited experiments to ~5 mm, and at this separation, attractive force had been detected immediately.
- Deconvolute the role of velocity in the observed extra long-range attractive force to determine how the speed of drop approach impacts magnitude of attractive force. This can be done by conducting careful experiments where water droplet is held sufficiently close to the surface to induce droplet elongation but far enough to avoid “jump-in”; thus any droplet elongation would occur independent of external drop displacement. A high-speed camera with more memory may be required to capture the full effect as the duration of such an experiment may be significant.
- Conduct experiments for different water drop functionalities (pH, salt concentration, etc.) over a wide range of substrate (silica, mica) exposure time to *n*-heptane to decouple substrate ageing time from other effects that impact drop elongation and extra long-range attractive force magnitude.
- Explore the effect of increased cation valency, such as $CaCl_2$, on the magnitude of extra long-range attractive force, by varying the salt type and concentration in top and/or bottom drop during drop/solid and drop/drop interactions
- Conduct experiments using different drop sizes to correlate potential impact on the magnitude of long-range force and drop elongation during approaching to investigate the size dependence and hence shed the light on the nature of such extra long-range attractive forces.
- Explore the presence and magnitude of extra long-range attractive force between 0° silica and water drop, as well as between two water drops, by conducting force measurements in other non-polar aliphatic solvents, such as dodecane, including water-saturated dodecane.

For “contaminated” water/silica system with model asphaltene compound C5PeC11 in toluene:

- Conduct experiments over a range of C5PeC11 concentrations to establish the role of C5PeC11 adsorption at the interface and aggregate formation on film stability and thin film drainage dynamics.
- Use mixture of model asphaltene compounds (e.g. C5Pe, C5PeC11, etc.) that mimic different specific asphaltene interfacial behaviours (e.g. C5Pe shows crumpling at oil/water interface) to better capture real asphaltene interfacial behaviour and thin film drainage dynamics
- Use various heptols (mixture of toluene and *n*-heptane at different volume ratios) to observe the effect of solvent type (*n*-heptane is a poor solvent for C5PeC11 and asphaltenes) on thin film drainage dynamics and stability.
- Vary the pH of water drop to understand how pH of the water drop affects film drainage dynamics and film stability (unstable interfacial films are desirable for W/O emulsion destabilization and phase separation). Specifically, high alkalinity is of interest, where deprotonation of C5PeC11 carboxylic acid group occurs and a reduction in interfacial tension at toluene/water interface is observed.[50]
- Procure a bimorph that could accommodate force measurements at higher temperatures, since desired temperature for industrial froth treatment applications in bitumen production is 80°C (the bimorph used in this work was limited to 40°C and below).

# Bibliography


(1) Kilpatrick, P. K. Water-in-Crude Oil Emulsion Stabilization: Review and Unanswered Questions. *Energy and Fuels* **2012**, *26* (7), 4017–4026.

(2) Czarnecki, J.; Moran, K. On the Stabilization Mechanism of Water-in-Oil Emulsions in Petroleum Systems. *Energy and Fuels* **2005**, *19* (5), 2074–2079.

(3) He, L.; Lin, F.; Li, X.; Sui, H.; Xu, Z. Interfacial Sciences in Unconventional Petroleum Production: From Fundamentals to Applications. *Chem. Soc. Rev.* **2015**, *44* (15), 5446–5494.

(4) Tchoukov, P.; Yang, F.; Xu, Z.; Dabros, T.; Czarnecki, J.; Sjoblom, J. Role of Asphaltenes in Stabilizing Thin Liquid Emulsion Films. *Langmuir* **2014**, *30* (11), 3024–3033.

(5) Yang, F.; Tchoukov, P.; Dettman, H.; Teklebrhan, R. B.; Liu, L.; Dabros, T.; Czarnecki, J.; Masliyah, J.; Xu, Z. Asphaltene Subfractions Responsible for Stabilizing Water-in-Crude Oil Emulsions. Part 2: Molecular Representations and Molecular Dynamics Simulations. *Energy and Fuels* **2015**, *29* (8), 4783–4794.

(6) Mozaffari, S.; Tchoukov, P.; Atias, J.; Czarnecki, J.; Nazemifard, N. Effect of Asphaltene Aggregation on Rheological Properties of Diluted Athabasca Bitumen. *Energy and Fuels* **2015**, *29* (9), 5595–5599.

(7) Hörmann, K.; Zimmer, A. Drug Delivery and Drug Targeting with Parenteral Lipid Nanoemulsions - A Review. *J. Control. Release* **2016**, *223*, 85–98.

(8) Mathapa, B. G.; Paunov, V. N. Fabrication of Novel Cyclodextrin-Polyallylamine Hydrochloride Co-Polymeric Microcapsules by Templating Oil-in-Water Emulsions. *Soft Matter* **2013**, *9* (19), 4780–4788.

(9) Sagalowicz, L.; Leser, M. E. Delivery Systems for Liquid Food Products. *Curr. Opin. Colloid Interface Sci.* **2010**, *15* (1–2), 61–72.

(10) McClements, D. J. Edible Nanoemulsions: Fabrication, Properties, and Functional Performance. *Soft Matter* **2011**, *7* (6), 2297–2316.

(11) Mulqueen, P. Recent Advances in Agrochemical Formulation. *Adv. Colloid Interface Sci.* **2003**, *106* (1–3), 83–107.

(12) Chan, D. Y. C.; Klaseboer, E.; Manica, R. Film Drainage and Coalescence between Deformable Drops and Bubbles. *Soft Matter* **2011**, *7* (6), 2235–2264.

(13) Ivanova, N. O.; Xu, Z.; Liu, Q.; Masliyah, J. H. Surface Forces in Unconventional Oil Processing. *Curr. Opin. Colloid Interface Sci.* **2017**, *27*, 63–73.

(14) Wu, X. Investigating the Stability Mechanism of Water-in-Diluted Bitumen Emulsions through Isolation and Characterization of the Stabilizing Materials at the Interface. *Energy*

*and Fuels* **2003**, *17* (1), 179–190.

(15) Wu, X.; van de Ven, T. G. M.; Czarnecki, J. Colloidal Forces between Emulsified Water Droplets in Toluene-Diluted Bitumen. *Colloids Surfaces A-Physicochemical Eng. Asp.* **1999**, *149* (1–3), 577–583.

(16) Pickering, S. U. CXCVI.—Emulsions. *J. Chem. Soc. Trans.* **1907**, *91* (0), 2001–2021.

(17) Masliyah, J. H.; Czarnecki, J.; Xu, Z. Chapter 7: Froth Treatment Fundamentals. In *Handbook on Theory and Practice of Bitumen Recovery from Athabasca Oil Sands*; Kingsley Knowledge Publishing, 2011; pp 349–386.

(18) Hartley, P. G.; Grieser, F.; Mulvaney, P.; Stevens, G. W. Surface Forces and Deformation at the Oil−Water Interface Probed Using AFM Force Measurement. *Langmuir* **1999**, *15* (21), 7282–7289.

(19) Feng, L.; Manica, R.; Grundy, J. S.; Liu, Q. Unraveling Interaction Mechanisms between Molybdenite and a Dodecane Oil Droplet Using Atomic Force Microscopy. *Langmuir* **2019**, *35* (18), 6024–6031.

(20) Gong, L.; Zhang, L.; Xiang, L.; Zhang, J.; Fattahpour, V.; Mamoudi, M.; Roostaei, M.; Fermaniuk, B.; Luo, J.-L.; Zeng, H. Surface Interactions between Water-in-Oil Emulsions with Asphaltenes and Electroless Nickel–Phosphorus Coating. *Langmuir* **2020**, *36* (4), 897–905.

(21) Hu, W.; Cui, X.; Xiang, L.; Gong, L.; Zhang, L.; Gao, M.; Wang, W.; Zhang, J.; Liu, F.; Yan, B.; et al. Tannic Acid Modified MoS2 Nanosheet Membranes with Superior Water Flux and Ion/Dye Rejection. *J. Colloid Interface Sci.* **2020**, *560*, 177–185.

(22) Ducker, W. A.; Xu, Z. H.; Israelachvili, J. N. Measurements of Hydrophobic and DLVO Forces in Bubble-Surface Interactions in Aqueous-Solutions. *Langmuir* **1994**, *10* (9), 3279–3289.

(23) Butt, H. J. A Technique for Measuring the Force between a Colloidal Particle in Water and a Bubble. *J. Colloid Interface Sci.* **1994**, *166* (1), 109–117.

(24) Kuznicki, N. P.; Harbottle, D.; Masliyah, J. H.; Xu, Z. Probing Mechanical Properties of Water–Crude Oil Interfaces and Colloidal Interactions of Petroleum Emulsions Using Atomic Force Microscopy. *Energy and Fuels* **2017**, *31* (4), 3445–3453.

(25) Kuznicki, N. P.; Harbottle, D.; Masliyah, J.; Xu, Z. Dynamic Interactions between a Silica Sphere and Deformable Interfaces in Organic Solvents Studied by Atomic Force Microscopy. *Langmuir* **2016**, *32* (38), 9797–9806.

(26) Liu, J.; Cui, X.; Santander, C.; Tan, X.; Liu, Q.; Zeng, H. Destabilization of Fine Solids Suspended in Oil Media through Wettability Modification and Water-Assisted Agglomeration. *Fuel* **2019**, *254*, 115623.

(27) Tabor, R. F.; Grieser, F.; Dagastine, R. R.; Chan, D. Y. C. Measurement and Analysis of Forces in Bubble and Droplet Systems Using AFM. *J. Colloid Interface Sci.* **2012**, *371*

(1), 1–14.

(28) Dagastine, R. R.; Manica, R.; Carnie, S. L.; Chan, D. Y. C.; Stevens, G. W.; Grieser, F. Dynamic Forces between Two Deformable Oil Droplets in Water. *Science* **2006**, *313* (5784), 210–213.

(29) Shi, C.; Zhang, L.; Xie, L.; Lu, X.; Liu, Q.; He, J.; Mantilla, C. A.; Van den berg, F. G. A.; Zeng, H. Surface Interaction of Water-in-Oil Emulsion Droplets with Interfacially Active Asphaltenes. *Langmuir* **2017**, *33* (5), 1265–1274.

(30) Xie, L.; Lu, Q.; Tan, X.; Liu, Q.; Tang, T.; Zeng, H. Interfacial Behavior and Interaction Mechanism of Pentol/Water Interface Stabilized with Asphaltenes. *J. Colloid Interface Sci.* **2019**, *553*, 341–349.

(31) Vakarelski, I. U.; Li, E. Q.; Thoroddsen, S. T. Soft Colloidal Probes for AFM Force Measurements between Water Droplets in Oil. *Colloids Surfaces A Physicochem. Eng. Asp.* **2014**, *462*, 259–263.

(32) Mettu, S.; Wu, C.; Dagastine, R. R. Dynamic Forces between Emulsified Water Drops Coated with Poly-Glycerol-Poly-Ricinoleate (PGPR) in Canola Oil. *J. Colloid Interface Sci.* **2018**, *517*, 166–175.

(33) Clark, K. A. Bituminuous Sand Processing. CA 289058, 1929.

(34) Clark, K. A. Extracting Oil from Bituminous Sand. CA 448231, 1948.

(35) Masliyah, J. H.; Czarnecki, J.; Xu, Z. Chapter 4: Physical and Chemical Properties of Oil Sands. In *Handbook on Theory and Practice of Bitumen Recovery from Athabasca Oil Sands*; Kingsley Knowledge Publishing, 2011; pp 173–256.

(36) Masliyah, J.; Zhou, Z. J.; Xu, Z.; Czarnecki, J.; Hamza, H. Understanding Water-Based Bitumen Extraction from Athabasca Oil Sands. *Can. J. Chem. Eng.* **2004**, *82* (4), 628–654.

(37) Yang, X. L.; Czarnecki, J. Tracing Sodium Naphthenate in Asphaltenes Precipitated from Athabasca Bitumen. *Energy and Fuels* **2005**, *19* (6), 2455–2459.

(38) Masliyah, J. H.; Czarnecki, J.; Xu, Z. Chapter 8: Colloidal Science in Tailings Management. In *Handbook on Theory and Practice of Bitumen Recovery from Athabasca Oil Sands*; Kingsley Knowledge Publishing, 2011; pp 391–448.

(39) Sztukowski, D. M.; Yarranton, H. W. Rheology of Asphaltene−Toluene/Water Interfaces. *Langmuir* **2005**, *21* (25), 11651–11658.

(40) Kota, A. K.; Kwon, G.; Choi, W.; Mabry, J. M.; Tuteja, A. Hygro-Responsive Membranes for Effective Oil-Water Separation. *Nat. Commun.* **2012**, *3*, 1025.

(41) Zhang, F.; Zhang, W. Bin; Shi, Z.; Wang, D.; Jin, J.; Jiang, L. Nanowire-Haired Inorganic Membranes with Superhydrophilicity and Underwater Ultralow Adhesive Superoleophobicity for High-Efficiency Oil/Water Separation. *Adv. Mater.* **2013**, *25* (30),

4192–4198.

(42) Strausz, O. P.; Mojelsky, T. W.; Lown, E. M. The Molecular-Structure of Asphaltene - an Unfolding Story. *Fuel* **1992**, *71* (12), 1355–1363.

(43) Mullins, O. C. The Modified Yen Model. *Energy and Fuels* **2010**, *24*, 2179–2207.

(44) Gray, M. R.; Tykwinski, R. R.; Stryker, J. M.; Tan, X. Supramolecular Assembly Model for Aggregation of Petroleum Asphaltenes. *Energy and Fuels* **2011**, *25* (7), 3125–3134.

(45) Yarranton, H. W.; Ortiz, D. P.; Barrera, D. M.; Baydak, E. N.; Barre, L.; Frot, D.; Eyssautier, J.; Zeng, H.; Xu, Z.; Dechaine, G.; et al. On the Size Distribution of Self-Associated Asphaltenes. *Energy and Fuels* **2013**, *27* (9), 5083–5106.

(46) Sjöblom, J.; Simon, S.; Xu, Z. Model Molecules Mimicking Asphaltenes. *Adv. Colloid Interface Sci.* **2015**, *218*, 1–16.

(47) Liu, L.; Zhang, R.; Wang, X.; Simon, S.; Sjöblom, J.; Xu, Z.; Jiang, B. Interactions of Polyaromatic Compounds. Part 1: Nanoaggregation Probed by Electrospray Ionization Mass Spectrometry and Molecular Dynamics Simulation. *Energy and Fuels* **2017**, *31* (4), 3465–3474.

(48) Wang, X.; Zhang, R.; Liu, L.; Qiao, P.; Simon, S.; Sjoblom, J.; Xu, Z.; Jiang, B. Interactions of Polyaromatic Compounds. Part 2. Flocculation Probed by Dynamic Light Scattering and Molecular Dynamics Simulation. *Energy and Fuels* **2017**, *31* (9), 9201–9212.

(49) Simon, S.; Wei, D.; Barriet, M.; Sjöblom, J. An ITC and NMR Study of Interaction and Complexation of Asphaltene Model Compounds in Apolar Solvent I: Self-Association Pattern. *Colloids Surfaces A Physicochem. Eng. Asp.* **2016**, *494*, 108–115.

(50) Pradilla, D.; Simon, S.; Sjöblom, J.; Samaniuk, J.; Skrzypiec, M.; Vermant, J. Sorption and Interfacial Rheology Study of Model Asphaltene Compounds. *Langmuir* **2016**, *32* (12), 2900–2911.

(51) Niu, Z.; Yue, T.; He, X.; Manica, R. Changing the Interface Between an Asphaltene Model Compound and Water by Addition of an EO–PO Demulsifier through Adsorption Competition or Adsorption Replacement. *Energy and Fuels* **2019**, *33* (6), 5035–5042.

(52) Andrews, A. B.; McClelland, A.; Korkeila, O.; Demidov, A.; Krummel, A.; Mullins, O. C.; Chen, Z. Molecular Orientation of Asphaltenes and PAH Model Compounds in Langmuir−Blodgett Films Using Sum Frequency Generation Spectroscopy. *Langmuir* **2011**, *27* (10), 6049–6058.

(53) Xu, Y.; Dabros, T.; Hamza, H.; Shefantook, W. Destabilization of Water in Bitumen Emulsion by Washing with Water. *Pet. Sci. Technol.* **1999**, *17* (9–10), 1051–1070.

(54) Stanford, L. A.; Rodgers, R. P.; Marshall, A. G.; Czarnecki, J.; Wu, X. A. Compositional Characterization of Bitumen/Water Emulsion Films by Negative- and Positive-Ion Electrospray Ionization and Field Desorption/Ionization Fourier Transform Ion Cyclotron

Resonance Mass Spectrometry. *Energy and Fuels* **2007**, *21* (2), 963–972.

(55) Yang, F.; Tchoukov, P.; Pensini, E.; Dabros, T.; Czarnecki, J.; Masliyah, J.; Xu, Z. Asphaltene Subfractions Responsible for Stabilizing Water-in-Crude Oil Emulsions. Part 1: Interfacial Behaviors. *Energy and Fuels* **2014**, *28* (11), 6897–6904.

(56) Qiao, P.; Harbottle, D.; Tchoukov, P.; Wang, X.; Xu, Z. Asphaltene Subfractions Responsible for Stabilizing Water-in-Crude Oil Emulsions. Part 3. Effect of Solvent Aromaticity. *Energy and Fuels* **2017**, *31* (9), 9179–9187.

(57) Chacón-Patiño, M. L.; Smith, D. F.; Hendrickson, C. L.; Marshall, A. G.; Rodgers, R. P. Advances in Asphaltene Petroleomics. Part 4. Compositional Trends of Solubility Subfractions Reveal That Polyfunctional Oxygen-Containing Compounds Drive Asphaltene Chemistry. *Energy and Fuels* **2020**, *34* (3), 3013–3030.

(58) Wang, S.; Liu, J.; Zhang, L.; Masliyah, J.; Xu, Z. Interaction Forces between Asphaltene Surfaces in Organic Solvents. *Langmuir* **2010**, *26* (1), 183–190.

(59) Mullins, O. C.; Sabbah, H.; Eyssautier, J.; Pomerantz, A. E.; Barre, L.; Andrews, A. B.; Ruiz-Morales, Y.; Mostowfi, F.; McFarlane, R.; Goual, L.; et al. Advances in Asphaltene Science and the Yen-Mullins Model. *Energy and Fuels* **2012**, *26* (7), 3986–4003.

(60) Natarajan, A.; Xie, J.; Wang, S.; Liu, Q.; Masliyah, J.; Zeng, H.; Xu, Z. Understanding Molecular Interactions of Asphaltenes in Organic Solvents Using a Surface Force Apparatus. *J. Phys. Chem. C* **2011**, *115* (32), 16043–16051.

(61) Natarajan, A.; Kuznicki, N.; Harbottle, D.; Masliyah, J.; Zeng, H.; Xu, Z. Understanding Mechanisms of Asphaltene Adsorption from Organic Solvent on Mica. *Langmuir* **2014**, *30* (31), 9370–9377.

(62) Harbottle, D.; Chen, Q.; Moorthy, K.; Wang, L.; Xu, S.; Liu, Q.; Sjoblom, J.; Xu, Z. Problematic Stabilizing Films in Petroleum Emulsions: Shear Rheological Response of Viscoelastic Asphaltene Films and the Effect on Drop Coalescence. *Langmuir* **2014**, *30* (23), 6730–6738.

(63) Taylor, S. D.; Czarnecki, J.; Masliyah, J. Disjoining Pressure Isotherms of Water-in-Bitumen Emulsion Films. *J. Colloid Interface Sci.* **2002**, *252* (1), 149–160.

(64) Reynolds, O. On the Theory of Lubrication and Its Application to Mr. Beauchamp Tower's Experiments, Including an Experimental Determination of the Viscosity of Olive Oil. *Phil. Trans. R. Soc. Lond.* **1886**, *177*, 157–234.

(65) Chan, D. Y. C.; Horn, R. G. The Drainage of Thin Liquid-Films between Solid-Surfaces. *J. Chem. Phys.* **1985**, *83* (10), 5311–5324.

(66) Sheludko, A. Thin Liquid Films. *Adv. Colloid Interface Sci.* **1967**, *1* (4), 391–464.

(67) Frankel, S. P.; Myseis, K. J. On the "Dimpling" During the Approach of Two Interfaces. *J. Phys. Chem.* **1962**, *66* (1), 190–191.

(68) Manor, O.; Vakarelski, I. U.; Stevens, G. W.; Grieser, F.; Dagastine, R. R.; Chan, D. Y. C. Dynamic Forces between Bubbles and Surfaces and Hydrodynamic Boundary Conditions. *Langmuir* **2008**, *24* (20), 11533–11543.

(69) Manica, R.; Connor, J. N.; Carnie, S. L.; Horn, R. G.; Chan, D. Y. C. Dynamics of Interactions Involving Deformable Drops: Hydrodynamic Dimpling under Attractive and Repulsive Electrical Double Layer Interactions. *Langmuir* **2007**, *23* (2), 626–637.

(70) Klaseboer, E.; Chevaillier, J. P.; Gourdon, C.; Masbernat, O. Film Drainage between Colliding Drops at Constant Approach Velocity: Experiments and Modeling. *J. Colloid Interface Sci.* **2000**, *229* (1), 274–285.

(71) Zhang, X.; Manica, R.; Tchoukov, P.; Liu, Q.; Xu, Z. Effect of Approach Velocity on Thin Liquid Film Drainage between an Air Bubble and a Flat Solid Surface. *J. Phys. Chem. C* **2017**, *121* (10), 5573–5584.

(72) Chan, D. Y. C.; Klaseboer, E.; Manica, R. Theory of Non-Equilibrium Force Measurements Involving Deformable Drops and Bubbles. *Adv. Colloid Interface Sci.* **2011**, *165* (2), 70–90.

(73) Danov, K. D. Effect of Surfactants on Drop Stability and Thin Film Drainage. In *Fluid Mechanics of Surfactant and Polymer Solutions*; Springer: New York, 2004; pp 1–38.

(74) Derjaguin, B.; Landau, L. D. Theory of Stability of Strongly Charged Lyophobic Sols and of the Adhesion of Strongly Charged Particles in Solutions of Electrolytes. *Acta Physicochim. URSS* **1941**, *14*, 633–662.

(75) Verwey, E. J. W.; Overbeek, J. T. G. *Theory of the Stability of Lyophobic Colloids*; Elsevier Publishing Company: Eindhoven, 1948.

(76) Ivanov, I. B.; Dimitrov, D. S. Thin Film Drainage. In *Thin Liquid Films Fundamentals and Applications*; Ivanov, I. B., Ed.; Marcel Dekker: New York, 1988; pp 379–496.

(77) Shi, C.; Yan, B.; Xie, L.; Zhang, L.; Wang, J.; Takahara, A.; Zeng, H. Long-Range Hydrophilic Attraction between Water and Polyelectrolyte Surfaces in Oil. *Angew. Chemie Int. Ed.* **2016**, *55* (48), 15017–15021.

(78) Jin, H.; Wang, W.; Chang, H.; Shen, Y.; Yu, Z.; Tian, Y.; Yu, Y.; Gong, J. Effects of Salt-Controlled Self-Assembly of Triblock Copolymers F68 on Interaction Forces between Oil Drops in Aqueous Solution. *Langmuir* **2017**, *33* (51), 14548–14555.

(79) Jamieson, E. J.; Fewkes, C. J.; Berry, J. D.; Dagastine, R. R. Forces between Oil Drops in Polymer-Surfactant Systems: Linking Direct Force Measurements to Microfluidic Observations. *J. Colloid Interface Sci.* **2019**, *544*, 130–143.

(80) Shi, C.; Zhang, L.; Xie, L.; Lu, X.; Liu, Q.; Mantilla, C. A.; van den Berg, F. G. A.; Zeng, H. Interaction Mechanism of Oil-in-Water Emulsions with Asphaltenes Determined Using Droplet Probe AFM. *Langmuir* **2016**, *32* (10), 2302–2310.

(81) Rocha, J. A.; Baydak, E. N.; Yarranton, H. W.; Sztukowski, D. M.; Ali-Marcano, V.;

Gong, L.; Shi, C.; Zeng, H. Role of Aqueous Phase Chemistry, Interfacial Film Properties, and Surface Coverage in Stabilizing Water-in-Bitumen Emulsions. *Energy and Fuels* **2016**, *30* (7), 5240–5252.

(82) Shi, C.; Cui, X.; Xie, L.; Liu, Q.; Chan, D. Y. C.; Israelachvili, J. N.; Zeng, H. Measuring Forces and Spatiotemporal Evolution of Thin Water Films between an Air Bubble and Solid Surfaces of Different Hydrophobicity. *ACS Nano* **2015**, *9* (1), 95–104.

(83) Ostendorf, F.; Schmitz, C.; Hirth, S.; Kühnle, A.; Kolodziej, J. J.; Reichling, M. How Flat Is an Air-Cleaved Mica Surface? *Nanotechnology* **2008**, *19* (30), 305705.

(84) Holm, B.; Ahuja, R.; Yourdshahyan, Y.; Johansson, B.; Lundqvist, B. I. Elastic and Optical Properties of Alpha- and Kappa-Al2O3. *Phys. Rev. B* **1999**, *59* (20), 12777–12787.

(85) De Graef, M.; McHenry, M. E. *Structure of Materials: An Introduction to Crystallography, Diffraction, and Symmetry*, 2nd ed.; Cambridge University Press: New York, 2012.

(86) Zhang, D.; Wang, Y.; Gan, Y. Characterization of Critically Cleaned Sapphire Single-Crystal Substrates by Atomic Force Microscopy, XPS and Contact Angle Measurements. *Appl. Surf. Sci.* **2013**, *274*, 405–417.

(87) Lifshitz, E. M. The Theory of Molecular Attractive Forces between Solids. *J. Exp. Theor. Phys. USSR* **1955**, *29*, 94–110.

(88) Israelachvili, J. N. *Intermolecular and Surface Forces*, 3rd ed.; Academic Press: Amsterdam, 2011.

(89) Butt, H.-J.; Graf, K.; Kappl, M. *Physics and Chemistry of Interfaces*; Wiley-VCH Verlag GmbH: Weinheim, 2003.

(90) Aralaguppi, M. I.; Jadar, C. V; Aminabhavi, T. M. Density, Refractive Index, Viscosity, and Speed of Sound in Binary Mixtures of Cyclohexanone with Hexane, Heptane, Octane, Nonane, Decane, Dodecane, and 2,2,4-Trimethylpentane. *J. Chem. Eng. Data* **1999**, *44* (3), 435–440.

(91) Saien, J.; Akbari, S. Interfacial Tension of Toluene + Water + Sodium Dodecyl Sulfate from (20 to 50)°C and PH between 4 and 9. *J. Chem. Eng. Data* **2006**, *51* (5), 1832–1835.

(92) Zeppieri, S.; Rodríguez, J.; López de Ramos, A. L. Interfacial Tension of Alkane + Water Systems. *J. Chem. Eng. Data* **2001**, *46* (5), 1086–1088.

(93) Kedenburg, S.; Vieweg, M.; Gissibl, T.; Giessen, H. Linear Refractive Index and Absorption Measurements of Nonlinear Optical Liquids in the Visible and Near-Infrared Spectral Region. *Opt. Mater. Express* **2012**, *2* (11), 1588–1611.

(94) Schiebener, P.; Straub, J.; Levelt Sengers, J. M. H.; Gallagher, J. S. Refractive Index of Water and Steam as Function of Wavelength, Temperature and Density. *J. Phys. Chem. Ref. Data* **1990**, *19* (3), 677–717.

(95) Zhang, X.; Tchoukov, P.; Manica, R.; Wang, L.; Liu, Q.; Xu, Z. Simultaneous Measurement of Dynamic Force and Spatial Thin Film Thickness between Deformable and Solid Surfaces by Integrated Thin Liquid Film Force Apparatus. *Soft Matter* **2016**, *12* (44), 9105–9114.

(96) Zhang, X.; Manica, R.; Tang, Y.; Tchoukov, P.; Liu, Q.; Xu, Z. Probing Boundary Conditions at Hydrophobic Solid–Water Interfaces by Dynamic Film Drainage Measurement. *Langmuir* **2018**, *34* (40), 12025–12035.

(97) Liu, B.; Manica, R.; Zhang, X.; Bussonnière, A.; Xu, Z.; Xie, G.; Liu, Q. Dynamic Interaction between a Millimeter-Sized Bubble and Surface Microbubbles in Water. *Langmuir* **2018**, *34* (39), 11667–11675.

(98) Liu, B.; Manica, R.; Liu, Q.; Klaseboer, E.; Xu, Z.; Xie, G. Coalescence of Bubbles with Mobile Interfaces in Water. *Phys. Rev. Lett.* **2019**, *122* (19), 194501.

(99) Nedyalkov, M.; Alexandrova, L.; Platikanov, D.; Levecke, B.; Tadros, T. Wetting Films on a Hydrophilic Silica Surface Obtained from Aqueous Solutions of Hydrophobically Modified Inulin Polymeric Surfactant. *Colloid Polym. Sci.* **2007**, *285* (15), 1713–1717.

(100) Parker, J. L. A Novel Method for Measuring the Force between 2 Surfaces in a Surface Force Apparatus. *Langmuir* **1992**, *8* (2), 551–556.

(101) Wang, L.; Sharp, D.; Masliyah, J.; Xu, Z. Measurement of Interactions between Solid Particles, Liquid Droplets, and/or Gas Bubbles in a Liquid Using an Integrated Thin Film Drainage Apparatus. *Langmuir* **2013**, *29* (11), 3594–3603.

(102) Simpson, S.; Jain, R. K.; Raghuraman, V.; Somasundaran, P. Thinning and Rupture of Aqueous Surfactant Films on Silica. In *Emulsions, Foams, and Thin Films*; Mittal, K. L., Kumar, P., Eds.; Marcel Dekker: New York, 2000; pp 233–250.

(103) Hsu, M. F.; Dufresne, E. R.; Weitz, D. A. Charge Stabilization in Nonpolar Solvents. *Langmuir* **2005**, *21* (11), 4881–4887.

(104) Briscoe, W. H.; Horn, R. G. Direct Measurement of Surface Forces Due to Charging of Solids Immersed in a Nonpolar Liquid. *Langmuir* **2002**, *18* (10), 3945–3956.

(105) Kanda, Y.; Yamamoto, T.; Higashitani, K. Origin of the Apparent Long-Range Attractive Force between Surfaces in Cyclohexane. *Adv. Powder Technol.* **2002**, *13* (2), 149–156.

(106) Barbagini, F.; Fyen, W.; Van Hoeymissen, J.; Mertens, P.; Fransaer, J. Time-Dependent Attractive Force Between a Silica Particle and a Silica Substrate in Dodecane. *J. Adhes. Sci. Technol.* **2008**, *22* (1), 65–75.

(107) dos Santos, A. P.; Levin, Y. Like-Charge Attraction between Metal Nanoparticles in a 1:1 Electrolyte Solution. *Phys. Rev. Lett.* **2019**, *122* (24), 248005.

(108) Khair, A. S. Electrostatic Forces on Two Almost Touching Nonspherical Charged Conductors. *J. Appl. Phys.* **2013**, *114* (13), 134906.

(109) Walmsley, H. L. The Avoidance Of Electrostatic Hazards In The Petroleum Industry. *J. Electrostat.* **1992**, *27* (1–2), 1–200.

(110) Berg, G.; Lundgaard, L.; Hansen, F. K. Elongation of Water Drops in Oil during Transient Electric Fields. In *IEEE International Conference on Dielectric Liquids*; 2005; pp 189–192.

(111) Eow, J. S.; Ghadiri, M. Motion, Deformation and Break-up of Aqueous Drops in Oils under High Electric Field Strengths. *Chem. Eng. Process. Process Intensif.* **2003**, *42* (4), 259–272.

(112) Polak, J.; Lu, B. C.-Y. Mutual Solubilities of Hydrocarbons and Water at 0 and 25 °C. *Can. J. Chem.* **1973**, *51* (24), 4018–4023.

(113) de Vos, W. M.; Cattoz, B.; Avery, M. P.; Cosgrove, T.; Prescott, S. W. Adsorption and Surfactant-Mediated Desorption of Poly(Vinylpyrrolidone) on Plasma- and Piranha-Cleaned Silica Surfaces. *Langmuir* **2014**, *30* (28), 8425–8431.

(114) Rumble, J. R.; Bruno, T. J. *CRC Handbook of Chemistry and Physics*, 100th ed.; Taylor & Francis, 2019.

(115) Dobrovinskaya, E. R.; Lytvynov, L. A.; Pishchik, V. V. *Sapphire - Material, Manufacturing, Applications*; Springer: New York, 2009.

(116) Srivastava, A.; Karthick, S.; Jayaprakash, K. S.; Sen, A. K. Droplet Demulsification Using Ultralow Voltage-Based Electrocoalescence. *Langmuir* **2018**, *34* (4), 1520–1527.

(117) Niu, Z.; Manica, R.; Li, Z.; He, X.; Sjoblom, J.; Xu, Z. Interfacial Properties Pertinent to W/O and O/W Emulsion Systems Prepared Using Polyaromatic Compounds. *Colloids Surfaces A Physicochem. Eng. Asp.* **2019**, *575*, 283–291.

(118) Butt, H.-J.; Kappl, M. *Surface and Interfacial Forces*, 2nd ed.; Wiley-VCH Verlag GmbH: Weinheim, 2018.

(119) Ducker, W. A.; Mastropietro, D. Forces between Extended Hydrophobic Solids: Is There a Long-Range Hydrophobic Force? *Curr. Opin. Colloid Interface Sci.* **2016**, *22*, 51–58.

(120) Horn, R. G.; Asadullah, M.; Connor, J. N. Thin Film Drainage: Hydrodynamic and Disjoining Pressures Determined from Experimental Measurements of the Shape of a Fluid Drop Approaching a Solid Wall. *Langmuir* **2006**, *22* (6), 2610–2619.